Energy dependent Hanbury Brown - Twiss interferometry and the freeze-out eccentricity of heavy ion collisions at STAR

Dissertation

Presented in Partial Fulfillment of the Requirements for the Degree Doctor of Philosophy in the Graduate School of The Ohio State University

By

Christopher Daniel Anson, A.A., A.S., B.S., M.S.

Graduate Program in Department of Physics

The Ohio State University

2014

Dissertation Committee:

Michael Lisa, Advisor

Thomas Humanic

John Beacom

Yuri Kovchegov

Abstract

Ultra-relativistic heavy ion collisions are believed to produce a state of deconfined quark-gluon plasma that is similar to the universe just after the Big Bang. To investigate the properties of this matter, a Beam Energy Scan was performed at the Relativistic Heavy Ion Collider (RHIC) at Brookhaven National Lab. Information about the phase diagram describing the matter produced in these collisions can be gained by studying the beam energy dependence of various observables. One such analysis is Hanbury Brown Twiss (HBT) interferometry which is used to measure the size and shape of the regions emitting particles which are in turn related to dynamical processes that drive the evolution of the collisions.

In this thesis analyses using two-pion HBT interferometry are presented for Au+Au collisions at $\sqrt{s_{NN}} = 7.7$, 11.5, 19.6, 27, 39, 62.4, and 200 GeV measured in the STAR detector during the Beam Energy Scan program. The dependence of extracted correlation lengths (radii) are studied as a function of beam energy, azimuthal angle relative to the reaction plane, centrality and transverse mass, $\langle m_T \rangle$. The eccentricity of the entire fireball at kinetic freeze-out can be extracted from the azimuthally-differential analysis. This freeze-out shape is believed to be sensitive to changes in the equation of state when measured as a function of beam energy. A new global fit method is studied as an alternate method to directly measure the parameters in the azimuthal analysis. The freeze-out eccentricity is observed to decrease monotonically with beam

energy which is qualitatively consistent with the trends from all model predictions and quantitatively most consistent with a hadronic transport model.

My parents

Acknowledgments

I would like to thank everyone I worked with as part of the STAR Collaboration and here in the OSU heavy ion group. In particular I'd like to thank Zbigniew Chajecki for his help when I was just getting starting with my analysis and my adivsor Mike Lisa for all of his help learning about HBT and the physics of heavy ion collisions.

I also must thank my parents, Barbara Anson and Daniel Anson and my brothers and sister Andrew, Joe and Wendy. All your encouragement over the years is greatly appreciated. I couldn't have made it this far without you.

Vita

April 10, 1976	Born—Muscatine, IA
May 1996	A.A. Muscatine Community College Muscatine, IA
May 1996	A.S. Physics Muscatine Community College Muscatine, IA
May 2000	B.S. Physics & Astronomy The University of Iowa Iowa City, IA
2000-2001	Teaching Assistant Department of Physics and Astronomy The University of Iowa Iowa City, IA
2002-2004	Professional Performance Scorer and Scoring Supervisor Pearson Educational Measurement Iowa City, IA
Fall 2003	Reader and Table Leader ACT, Inc. Iowa City, IA
2004-2006	Graduate Teaching Assistant Departement of Physics Creighton University Omaha, NE
May 2006	M.S. Physics Creighton University Omaha, NE

2006-2009 ..... Graduate Teaching Associate
Department of Physics
The Ohio State University
Columbus, OH

2009-2013 ..... Graduate Research Associate
Department of Physics
The Ohio State University
Columbus, OH

Publications

[1] C. Anson [STAR Collaboration], "Energy dependence of the freeze out eccentricity from the azimuthal dependence of HBT at STAR," J. Phys. G **38**, 124148 (2011) [arXiv:1107.1527 [nucl-ex]].

[2] B. Abelev *et al.* [ALICE Collaboration], "Multiplicity dependence of two-particle azimuthal correlations in pp collisions at the LHC," arXiv:1307.1249 [nucl-ex].

[3] B. Abelev *et al.* [ALICE Collaboration], "Directed flow of charged particles at mid-rapidity relative to the spectator plane in Pb-Pb collisions at $\sqrt{s_{NN}}$=2.76 TeV," arXiv:1306.4145 [nucl-ex].

[4] E. Abbas *et al.* [ALICE Collaboration], "Performance of the ALICE VZERO system," arXiv:1306.3130 [nucl-ex].

[5] B. Abelev *et al.* [ALICE Collaboration], "D meson elliptic flow in non-central Pb-Pb collisions at $/sqrts_{NN}$ = 2.76 TeV," arXiv:1305.2707 [nucl-ex].

[6] E. Abbas *et al.* [ALICE Collaboration], "Mid-rapidity anti-baryon to baryon ratios in pp collisions at $\sqrt{s}$ = 0.9, 2.76 and 7 TeV measured by ALICE," arXiv:1305.1562 [nucl-ex].

[7] E. Abbas *et al.* [ALICE Collaboration], "Charmonium and e^+e^- pair photoproduction at mid-rapidity in ultra-peripheral Pb-Pb collisions at $\sqrt{s_{NN}}$ = 2.76 TeV," arXiv:1305.1467 [nucl-ex].

[8] E. Abbas *et al.* [ALICE Collaboration], "Centrality dependence of the pseudorapidity density distribution for charged particles in Pb-Pb collisions at sqrt(sNN) = 2.76 TeV," arXiv:1304.0347 [nucl-ex].

[8] E. Abbas *et al.* [ALICE Collaboration], "J/ψ Elliptic Flow in Pb-Pb Collisions at $\sqrt{s_{NN}}$=2.76 TeV," arXiv:1303.5880 [nucl-ex].

[9] L. Adamczyk *et al.* [STAR Collaboration], "Measurement of Charge Multiplicity Asymmetry Correlations in High Energy Nucleus-Nucleus Collisions at 200 GeV," arXiv:1303.0901 [nucl-ex].

[10] B. Abelev *et al.* [ALICE Collaboration], "Centrality dependence of π, K, p production in Pb-Pb collisions at $\sqrt{s_{NN}} = 2.76$ TeV," arXiv:1303.0737 [hep-ex].

[11] L. Adamczyk *et al.* [STAR Collaboration], "Jet-Hadron Correlations in $\sqrt{s_{NN}} =$ 200 GeV Au+Au and $p + p$ Collisions," arXiv:1302.6184 [nucl-ex].

[12] L. Adamczyk *et al.* [STAR Collaboration], "Fluctuations of charge separation perpendicular to the event plane and local parity violation in $\sqrt{s_{NN}} = 200$ GeV Au+Au collisions at RHIC," arXiv:1302.3802 [nucl-ex].

[13] L. Adamczyk *et al.* [STAR Collaboration], "Freeze-out Dynamics via Charged Kaon Femtoscopy in sqrt(sNN)=200 GeV Central Au+Au Collisions," arXiv:1302.3168 [nucl-ex].

[14] L. Adamczyk *et al.* [STAR Collaboration], "System Size Dependence of Transverse Momentum Correlations at RHIC," arXiv:1301.6633 [nucl-ex].

[15] B. Abelev *et al.* [ALICE Collaboration], "Centrality determination of Pb-Pb collisions at sqrt(sNN) = 2.76 TeV with ALICE," arXiv:1301.4361 [nucl-ex].

[16] B. Abelev *et al.* [ALICE Collaboration], "Charge correlations using the balance function in Pb-Pb collisions at $\sqrt{s_{NN}} = 2.76$ TeV," Phys. Lett. B **723**, 267 (2013) [arXiv:1301.3756 [nucl-ex]].

[17] B. Abelev *et al.* [ALICE Collaboration], "Measurement of the inclusive differential jet cross section in *pp* collisions at $\sqrt{s} = 2.76$ TeV," Phys. Lett. B **722**, 262 (2013) [arXiv:1301.3475 [nucl-ex]].

[18] L. Adamczyk *et al.* [STAR Collaboration], "Elliptic flow of identified hadrons in Au+Au collisions at $\sqrt{s_{NN}} = 7.7$–62.4 GeV," arXiv:1301.2348 [nucl-ex].

[19] L. Adamczyk *et al.*, "Observation of an energy-dependent difference in elliptic flow between particles and anti-particles in relativistic heavy ion collisions," arXiv:1301.2347 [nucl-ex].

[20] L. Adamczyk *et al.* [STAR Collaboration], "Third Harmonic Flow of Charged Particles in Au+Au Collisions at sqrtsNN = 200 GeV," arXiv:1301.2187 [nucl-ex].

[21] B. Abelev *et al.* [ALICE Collaboration], "Charged kaon femtoscopic correlations in *pp* collisions at $\sqrt{s} = 7$ TeV," arXiv:1212.5958 [hep-ex].

[22] L. Adamczyk *et al.* [STAR Collaboration], "Measurement of J/ψ Azimuthal Anisotropy in Au+Au Collisions at $\sqrt{s_{NN}} = 200$ GeV," arXiv:1212.3304 [nucl-ex].

[23] B. Abelev *et al.* [ALICE Collaboration], "Long-range angular correlations on the near and away side in p-Pb collisions at sqrt(sNN) = 5.02 TeV," arXiv:1212.2001 [nucl-ex].

[24] L. Adamczyk *et al.* [STAR Collaboration], "Studies of di-jets in Au+Au collisions using angular correlations with respect to back-to-back leading hadrons," arXiv:1212.1653 [nucl-ex].

[25] B. Abelev *et al.* [ALICE Collaboration], "Transverse Momentum Distribution and Nuclear Modification Factor of Charged Particles in *p*-Pb Collisions at $\sqrt{s_{NN}} = 5.02$ TeV," arXiv:1210.4520 [nucl-ex].

[26] B. Abelev *et al.* [ALICE Collaboration], "Pseudorapidity density of charged particles *p*-Pb collisions at $\sqrt{s_{NN}} = 5.02$ TeV," Phys. Rev. Lett. **110**, 032301 (2013) [arXiv:1210.3615 [nucl-ex]].

[27] B. Abelev *et al.* [ALICE Collaboration], "Coherent J/ψ photoproduction in ultra-peripheral Pb-Pb collisions at $\sqrt{s_{NN}} = 2.76$ TeV," Phys. Lett. B **718**, 1273 (2013) [arXiv:1209.3715 [nucl-ex]].

[28] B. Abelev *et al.* [ALICE Collaboration], "Measurement of inelastic, single- and double-diffraction cross sections in proton–proton collisions at the LHC with ALICE," Eur. Phys. J. C **73**, 2456 (2013) [arXiv:1208.4968 [hep-ex]].

[29] L. Adamczyk *et al.* [STAR Collaboration], "J/ψ production at high transverse momenta in $p + p$ and Au+Au collisions at $\sqrt{s_{NN}} = 200$ GeV," Phys. Lett. B **722**, 55 (2013) [arXiv:1208.2736 [nucl-ex]].

[30] B. Abelev *et al.* [ALICE Collaboration], "Centrality Dependence of Charged Particle Production at Large Transverse Momentum in Pb–Pb Collisions at $\sqrt{s_{\rm NN}} = 2.76$ TeV," Phys. Lett. B **720**, 52 (2013) [arXiv:1208.2711 [hep-ex]].

[31] B. Abelev *et al.* [ALICE Collaboration], "D_s^+ meson production at central rapidity in proton–proton collisions at $\sqrt{s} = 7$ TeV," Phys. Lett. B **718**, 279 (2012) [arXiv:1208.1948 [hep-ex]].

[32] B. Abelev *et al.* [ALICE Collaboration], "Measurement of electrons from beauty hadron decays in pp collisions at $\sqrt{s} = 7$ TeV," Phys. Lett. B **721**, 13 (2013) [arXiv:1208.1902 [hep-ex]].

[33] L. Adamczyk *et al.* [STAR Collaboration], "Inclusive charged hadron elliptic flow in Au + Au collisions at $\sqrt{s_{NN}} = 7.7$ - 39 GeV," Phys. Rev. C **86**, 054908 (2012) [arXiv:1206.5528 [nucl-ex]].

[34] L. Adamczyk *et al.* [STAR Collaboration], "Single Spin Asymmetry A_N in Polarized Proton-Proton Elastic Scattering at $\sqrt{s} = 200$ GeV," Phys. Lett. B **719**, 62 (2013) [arXiv:1206.1928 [nucl-ex]].

[35] L. Adamczyk *et al.* [STAR Collaboration], "Transverse Single-Spin Asymmetry and Cross-Section for π^0 and η Mesons at Large Feynman-x in Polarized $p + p$ Collisions at $\sqrt{s} = 200$ GeV," Phys. Rev. D **86**, 051101 (2012) [arXiv:1205.6826 [nucl-ex]].

[36] B. Abelev *et al.* [ALICE Collaboration], "Neutral pion and η meson production in proton-proton collisions at $\sqrt{s} = 0.9$ TeV and $\sqrt{s} = 7$ TeV," Phys. Lett. B **717**, 162 (2012) [arXiv:1205.5724 [hep-ex]].

[37] B. Abelev *et al.* [ALICE Collaboration], "Transverse sphericity of primary charged particles in minimum bias proton-proton collisions at $\sqrt{s} = 0.9$, 2.76 and 7 TeV," Eur. Phys. J. C **72**, 2124 (2012) [arXiv:1205.3963 [hep-ex]].

[38] L. Adamczyk *et al.* [STAR Collaboration], "Longitudinal and transverse spin asymmetries for inclusive jet production at mid-rapidity in polarized $p + p$ collisions at $\sqrt{s} = 200$ GeV," Phys. Rev. D **86**, 032006 (2012) [arXiv:1205.2735 [nucl-ex]].

[39] L. Adamczyk *et al.* [STAR Collaboration], "Measurements of D^0 and D^* Production in $p + p$ Collisions at $\sqrt{s} = 200$ GeV," Phys. Rev. D **86**, 072013 (2012) [arXiv:1204.4244 [nucl-ex]].

[40] L. Adamczyk *et al.* [STAR Collaboration], "Di-electron spectrum at mid-rapidity in p+p collisions at $\sqrt{s} = 200$ GeV," Phys. Rev. C **86**, 024906 (2012) [arXiv:1204.1890 [nucl-ex]].

[41] B. Abelev *et al.* [ALICE Collaboration], "Multi-strange baryon production in pp collisions at $(s)^1/2 = 7$ TeV with ALICE," Phys. Lett. B **712**, 309 (2012) [arXiv:1204.0282 [nucl-ex]].

[42] B. Abelev *et al.* [ALICE Collaboration], "Inclusive J/ψ production in pp collisions at $\sqrt{s} = 2.76$ TeV," Phys. Lett. B **718**, 295 (2012) [arXiv:1203.3641 [hep-ex]].

[43] B. Abelev *et al.* [ALICE Collaboration], "J/ψ Production as a Function of Charged Particle Multiplicity in pp Collisions at $\sqrt{s} = 7$ TeV," Phys. Lett. B **712**, 165 (2012) [arXiv:1202.2816 [hep-ex]].

[44] B. Abelev *et al.* [ALICE Collaboration], "J/ψ suppression at forward rapidity in Pb-Pb collisions at $\sqrt{s_{NN}} = 2.76$ TeV," Phys. Rev. Lett. **109**, 072301 (2012) [arXiv:1202.1383 [hep-ex]].

[45] B. Abelev *et al.* [ALICE Collaboration], "Measurement of Event Background Fluctuations for Charged Particle Jet Reconstruction in Pb-Pb collisions at $\sqrt{s_{NN}} = 2.76$ TeV," JHEP **1203**, 053 (2012) [arXiv:1201.2423 [hep-ex]].

[46] L. Adamczyk *et al.* [STAR Collaboration], "Directed Flow of Identified Particles in Au + Au Collisions at $\sqrt{s_N N} = 200$ GeV at RHIC," Phys. Rev. Lett. **108**, 202301 (2012) [arXiv:1112.3930 [nucl-ex]].

[47] L. Adamczyk *et al.* [STAR Collaboration], "Measurement of the $W \to e\nu$ and $Z/\gamma^* \to e^+e^-$ Production Cross Sections at Mid-rapidity in Proton-Proton Collisions at $\sqrt{s} = 500$ GeV," Phys. Rev. D **85**, 092010 (2012) [arXiv:1112.2980 [hep-ex]].

[49] B. Abelev *et al.* [ALICE Collaboration], "Light vector meson production in pp collisions at $\sqrt{s} = 7$ TeV," Phys. Lett. B **710**, 557 (2012) [arXiv:1112.2222 [nucl-ex]].

[50] B. Abelev *et al.* [ALICE Collaboration], "Underlying Event measurements in pp collisions at $\sqrt{s} = 0.9$ and 7 TeV with the ALICE experiment at the LHC," JHEP **1207**, 116 (2012) [arXiv:1112.2082 [hep-ex]].

[51] G. Agakishiev *et al.* [STAR Collaboration], "Energy and system-size dependence of two- and four-particle v_2 measurements in heavy-ion collisions at RHIC and their implications on flow fluctuations and nonflow," Phys. Rev. C **86**, 014904 (2012) [arXiv:1111.5637 [nucl-ex]].

[52] B. Abelev *et al.* [ALICE Collaboration], "Measurement of charm production at central rapidity in proton-proton collisions at $\sqrt{s} = 7$ TeV," JHEP **1201**, 128 (2012) [arXiv:1111.1553 [hep-ex]].

[53] B. Abelev *et al.* [ALICE Collaboration], "J/ψ polarization in pp collisions at $\sqrt{s} = 7$ TeV," Phys. Rev. Lett. **108**, 082001 (2012) [arXiv:1111.1630 [hep-ex]].

[54] G. Agakishiev *et al.* [STAR Collaboration], "System size and energy dependence of near-side di-hadron correlations," Phys. Rev. C **85**, 014903 (2012) [arXiv:1110.5800 [nucl-ex]].

[55] G. Agakishiev *et al.* [STAR Collaboration], "Identified hadron compositions in p+p and Au+Au collisions at high transverse momenta at $\sqrt{s_{_{NN}}} = 200$ GeV," Phys. Rev. Lett. **108**, 072302 (2012) [arXiv:1110.0579 [nucl-ex]].

[56] G. Agakishiev *et al.* [STAR Collaboration], "Directed and elliptic flow of charged particles in Cu+Cu collisions at $\sqrt{\boldsymbol{s_{NN}}} = 22.4$ GeV," Phys. Rev. C **85**, 014901 (2012) [arXiv:1109.5446 [nucl-ex]].

[57] G. Agakishiev *et al.* [STAR Collaboration], "Anomalous centrality evolution of two-particle angular correlations from Au-Au collisions at $\sqrt{s_{\rm NN}} = 62$ and 200 GeV," Phys. Rev. C **86**, 064902 (2012) [arXiv:1109.4380 [nucl-ex]].

[58] G. Agakishiev *et al.* [STAR Collaboration], "ρ^0 Photoproduction in AuAu Collisions at $\sqrt{s_{NN}}$=62.4 GeV with STAR," Phys. Rev. C **85**, 014910 (2012) [arXiv:1107.4630 [nucl-ex]].

[59] G. Agakishiev *et al.* [STAR Collaboration], "Strangeness Enhancement in Cu+Cu and Au+Au Collisions at $\sqrt{s_{NN}} = 200$ GeV," Phys. Rev. Lett. **108**, 072301 (2012) [arXiv:1107.2955 [nucl-ex]].

[60] H. Agakishiev *et al.* [STAR Collaboration], "Evolution of the differential transverse momentum correlation function with centrality in Au+Au collisions at $\sqrt{s_{NN}} =$ 200 GeV," Phys. Lett. B **704**, 467 (2011) [arXiv:1106.4334 [nucl-ex]].

[61] K. Aamodt *et al.* [ALICE Collaboration], "Higher harmonic anisotropic flow measurements of charged particles in Pb-Pb collisions at $\sqrt{s_{NN}}$=2.76 TeV," Phys. Rev. Lett. **107**, 032301 (2011) [arXiv:1105.3865 [nucl-ex]].

[62] K. Aamodt *et al.* [ALICE Collaboration], "Rapidity and transverse momentum dependence of inclusive J/psi production in *pp* collisions at $\sqrt{s} = 7$ TeV," Phys. Lett. B **704**, 442 (2011) [Erratum-ibid. B **718**, 692 (2012)] [arXiv:1105.0380 [hep-ex]].

[63] H. Agakishiev *et al.* [STAR Collaboration], "Observation of the antimatter helium-4 nucleus," Nature **473**, 353 (2011) [Erratum-ibid. **475**, 412 (2011)] [arXiv:1103.3312 [nucl-ex]].

[64] H. Agakishiev *et al.* [STAR Collaboration], "High p_T non-photonic electron production in $p + p$ collisions at $\sqrt{s} = 200$ GeV," Phys. Rev. D **83**, 052006 (2011) [arXiv:1102.2611 [nucl-ex]].

[65] H. Agakishiev *et al.* [STAR Collaboration], "Studies of di-jet survival and surface emission bias in Au+Au collisions via angular correlations with respect to back-to-back leading hadrons," Phys. Rev. C **83**, 061901 (2011) [arXiv:1102.2669 [nucl-ex]].

[66] K. Aamodt *et al.* [ALICE Collaboration], "Production of pions, kaons and protons in *pp* collisions at $\sqrt{s} = 900$ GeV with ALICE at the LHC," Eur. Phys. J. C **71**, 1655 (2011) [arXiv:1101.4110 [hep-ex]].

[67] K. Aamodt *et al.* [ALICE Collaboration], "Femtoscopy of *pp* collisions at $\sqrt{s} =$ 0.9 and 7 TeV at the LHC with two-pion Bose-Einstein correlations," Phys. Rev. D **84**, 112004 (2011) [arXiv:1101.3665 [hep-ex]].

[68] K. Aamodt *et al.* [ALICE Collaboration], "Two-pion Bose-Einstein correlations in central Pb-Pb collisions at $sqrt(s_N N) = 2.76$ TeV," Phys. Lett. B **696**, 328 (2011) [arXiv:1012.4035 [nucl-ex]].

[69] K. Aamodt *et al.* [ALICE Collaboration], "Strange particle production in proton-proton collisions at sqrt(s) = 0.9 TeV with ALICE at the LHC," Eur. Phys. J. C **71**, 1594 (2011) [arXiv:1012.3257 [hep-ex]].

[70] K. Aamodt *et al.* [ALICE Collaboration], "Centrality dependence of the charged-particle multiplicity density at mid-rapidity in Pb-Pb collisions at $\sqrt{s_{NN}} = 2.76$ TeV," Phys. Rev. Lett. **106**, 032301 (2011) [arXiv:1012.1657 [nucl-ex]].

[71] K. Aamodt *et al.* [ALICE Collaboration], "Suppression of Charged Particle Production at Large Transverse Momentum in Central Pb–Pb Collisions at $\sqrt{s_{NN}} =$ 2.76 TeV," Phys. Lett. B **696**, 30 (2011) [arXiv:1012.1004 [nucl-ex]].

[72] K. Aamodt *et al.* [ALICE Collaboration], "Elliptic flow of charged particles in Pb-Pb collisions at 2.76 TeV," Phys. Rev. Lett. **105**, 252302 (2010) [arXiv:1011.3914 [nucl-ex]].

[73] K. Aamodt *et al.* [ALICE Collaboration], "Charged-particle multiplicity density at mid-rapidity in central Pb-Pb collisions at $\sqrt{s_{NN}} = 2.76$ TeV," Phys. Rev. Lett. **105**, 252301 (2010) [arXiv:1011.3916 [nucl-ex]].

[74] H. Agakishiev *et al.* [STAR Collaboration], "Measurements of Dihadron Correlations Relative to the Event Plane in Au+Au Collisions at $\sqrt{s_{NN}} = 200$ GeV," arXiv:1010.0690 [nucl-ex].

[75] M. M. Aggarwal *et al.* [STAR Collaboration], "Strange and Multi-strange Particle Production in Au+Au Collisions at $\sqrt{s_{NN}} = 62.4$ GeV," Phys. Rev. C **83**, 024901 (2011) [arXiv:1010.0142 [nucl-ex]].

[76] M. M. Aggarwal *et al.* [STAR Collaboration], "Measurement of the parity-violating longitudinal single-spin asymmetry for $W^{\pm}$ boson production in polarized proton-proton collisions at $\sqrt{s} = 500 - GeV$," Phys. Rev. Lett. **106**, 062002 (2011) [arXiv:1009.0326 [hep-ex]].

[77] M. M. Aggarwal *et al.* [STAR Collaboration], "Scaling properties at freeze-out in relativistic heavy ion collisions," Phys. Rev. C **83**, 034910 (2011) [arXiv:1008.3133 [nucl-ex]].

[78] M. M. Aggarwal *et al.* [STAR Collaboration], "Measurement of the Bottom contribution to non-photonic electron production in $p+p$ collisions at $\sqrt{s}$=200 GeV," Phys. Rev. Lett. **105**, 202301 (2010) [arXiv:1007.1200 [nucl-ex]].

[79] K. Aamodt *et al.* [ALICE Collaboration], "Two-pion Bose-Einstein correlations in pp collisions at $\sqrt{s} = 900$ GeV," Phys. Rev. D **82**, 052001 (2010) [arXiv:1007.0516 [hep-ex]].

[80] K. Aamodt *et al.* [ALICE Collaboration], "Transverse momentum spectra of charged particles in proton-proton collisions at $\sqrt{s} = 900$ GeV with ALICE at the LHC," Phys. Lett. B **693**, 53 (2010) [arXiv:1007.0719 [hep-ex]].

[81] A. :: K. Aamodt *et al.* [ALICE Collaboration], "Midrapidity antiproton-to-proton ratio in pp collisions at $\sqrt{s} = 0.9$ and 7 TeV measured by the ALICE experiment," Phys. Rev. Lett. **105**, 072002 (2010) [arXiv:1006.5432 [hep-ex]].

[82] M. M. Aggarwal *et al.* [STAR Collaboration], "K^{*0} production in Cu+Cu and Au+Au collisions at $\sqrt{s_N N}$ = 62.4 GeV and 200 GeV," Phys. Rev. C **84**, 034909 (2011) [arXiv:1006.1961 [nucl-ex]].

[83] K. Aamodt *et al.* [ALICE Collaboration], "Charged-particle multiplicity measurement in proton-proton collisions at $\sqrt{s} = 0.9$ and 2.36 TeV with ALICE at LHC," Eur. Phys. J. C **68**, 89 (2010) [arXiv:1004.3034 [hep-ex]].

[84] K. Aamodt *et al.* [ALICE Collaboration], "Charged-particle multiplicity measurement in proton-proton collisions at $\sqrt{s} = 7$ TeV with ALICE at LHC," Eur. Phys. J. C **68**, 345 (2010) [arXiv:1004.3514 [hep-ex]].

[85] K. Aamodt *et al.* [ALICE Collaboration], "Alignment of the ALICE Inner Tracking System with cosmic-ray tracks," JINST **5**, P03003 (2010) [arXiv:1001.0502 [physics.ins-det]].

[86] K. Aamodt *et al.* [ALICE Collaboration], "First proton-proton collisions at the LHC as observed with the ALICE detector: Measurement of the charged particle pseudorapidity density at s**(1/2) = 900-GeV," Eur. Phys. J. C **65**, 111 (2010) [arXiv:0911.5430 [hep-ex]].

[87] K. Aamodt *et al.* [ALICE Collaboration], "The ALICE experiment at the CERN LHC," JINST **3**, S08002 (2008).

Fields of Study

Major Field: Physics

Studies in High Energy Nuclear Particle Physics: Mike Lisa

Table of Contents

List of Tables

List of Figures

Figure **Page**

Chapter 1: Introduction

The universe immediately after the Big Bang was composed of matter under extraordinary conditions of extreme temperatures and pressures. About a microsecond after the Big Bang all matter was in a state of deconfined quarks and gluons. As the universe expanded and cooled, the quarks and gluons coalesced into neutrons and protons. Many of the neutrons and protons became bound into the nuclei that form the ordinary matter we observe all around us. Today, the initial quarks and gluons remain tightly bound, deep within ordinary matter. To study the material in the early universe requires compressing material to sufficiently high energy density to break the material back into quarks and gluons. This may be possible by colliding heavy nuclei at high energy. Compressing together many protons and neutrons may create a small, short-lived pocket of deconfined quarks and gluons. Of course, historically speaking all this is a rather recent discovery.

It was only in the late 1800s that scientists determined that matter was composed of atoms. In the early 1900s it was found that the these atoms each contained a small, dense nucleus composed of smaller, tightly bound neutrons and protons. The nuclei were surrounded by diffuse clouds of relatively loosely bound electrons. In the

latter half of the 1900s it was found that these neutrons and protons were themselves composed of smaller particles, quarks and gluons, that interacted according to a new force, the strong nuclear force.

In particle collisions, either in accelerators or cosmic ray studies, new particles were identified and their properties studied. Particle collisions were produced at higher and higher energies as technology allowed more powerful colliders to be designed. As the energy of the collisions were increased smaller and smaller length scales were probed. Instead of probing the structure of atoms at keV energies, MeV colliders probed the structure of the nucleus. New, heavier unstable particles were discovered as more energy is required to produce more massive particles. At GeV energies the structure of the matter at scales smaller than the size of the protons and neutrons could be investigated. It was at these high energies that quarks were discovered and the theory of quantum chromodynamics (QCD) was created to explain the observed properties of the quarks.

Several decades ago Cabibbo and Parisi [1], Shuryak [2] and others suggested collisions of heavy nuclei may compress the nuclear matter so it exceeds normal nuclear density (0.17 GeV fm^{-3}) possibly to the extent that individual nucleons overlap and the quarks are no longer bound inside individual nucleons. They are free to interact en mass, forming a bulk state of deconfined quarks and gluons. This is a concept referred to as asymptotic freedom, as there is a transition from bound quarks to freely interacting quarks. If the transition was experimentally observable it would provide an opportunity to verify and refine the QCD theory. This simple argument provided motivation to develop the field of high energy nuclear physics and build machines to collide nuclei over wide ranges of both nuclear size and collision energy.

In previous experiments at the Bevalac at Lawrance Berkeley National Lab (LBNL), the Alternating Gradient Synchrotron (AGS) at Brookhaven National Lab (BNL), and the Super Proton Synchrotron (SPS) at the European Center for Nuclear Research (CERN) techniques for studying nuclear collisions were developed. The nuclear collisions studied were at center of mass energies, $\sqrt{s_{NN}}$, up to 17.3 A·GeV. With the creation of the Relativistic Heavy Ion Collider (RHIC) at BNL, Au+Au collisions at energies as high as 200 GeV may be studied and the accelerator is designed to perform at lower energies (≈5-200 GeV) and for different collision systems (p+p, d+Au, Cu+Cu, U+U, etc.). The Large Hadron Collider (LHC) at CERN now allows Pb+Pb collisions as high as 7 TeV.

The results from RHIC experiments (STAR, PHENIX, PHOBOS, and BRAHMS) indicate that the material produced in collisions at its highest energies studied (62.4, 130, 200 GeV) is a state of deconfined quarks and gluons predicted by QCD [3–6]. At some energy (or energies) there must be a transition from normal nuclear matter to this deconfined state that should leave some signature in the various observables that can be measured. Due to the flexibility of the RHIC accelerator, a Beam Energy Scan was proposed to map out the nature of the phase diagram for nuclear matter [7]. The goal is to look at many observables simultanously across a range of lower energies and see if there are changes that might provide an understanding of the phase transition that appears to occur at higher energy. Abrupt changes or non-monotonic behavior might indicate a change in the type of phase transition; the slope of the equation of state might develop a flat region indicative of a mixed phase at certain energies. Other observed behavior attributed to a deconfined state at higher energies may no longer be observed below some energy or may become less and less prominent.

This thesis explores one of the main observables - the shape of the collisions during the short period of time when all the interactions cease and the produced particles freeze-out and free stream to the detectors. This period is referred to as kinetic freeze-out. The shape is expressed as a freeze-out eccentricity obtained in an azimuthally-differential Hanbury Brown Twiss (HBT) analysis and plotted as a function of beam energy. As described later, if non-monotonic behavior were observed it might indicate a different equation of state at some energy that could suggest the type of phase transition has changed [8]. Standard azimuthally-integrated HBT analysis also is performed as it provides information related to the source sizes emitting pions, evolution of the system volume and system lifetime, and information about the temperature of the system at different collision energies. Chapter 2 provides an overview of some relevant information about the fundamental particles in the standard model, the evolution of the collisions and physical processes that drive the evolution. In Chapter 3 the expected QCD phase diagram is reviewed and the broad Beam Energy Scan program is described. The current analysis is placed within the context of this larger effort. Chapter 4 then gives a description of the RHIC complex and the STAR detector focusing on subsystems relavent to this analysis. The concepts underlying the Hanbury Brown - Twiss (HBT) Interferometry are presented in Chapter 5 while Chapter 6 elaborates on how the HBT radii and freeze-out eccentricity can be experimentally extracted. In Chapter 7 details of the data sets and event, track and pair selections used in the analysis are outlined. The results are presented in Chapter 8 along with discussion. Finally, in Chapter 9, conclusions are drawn about what has been learned.

Chapter 2: The structure of matter and nuclear collision evolution

The study of ultra-relativistic nuclear collisions allows investigation of the fundamental structure of matter and the processes that occur when the exotic matter produced in the collisions evolves back into ordinary, stable matter. This chapter provides a review of the structure of matter, the evolution of nuclear collisions, and some of the processes that occur in the collisions that are especially relavent to the current work. The last section gives a general discussion of the thermodynamic description of nuclear material.

2.1 The structure of matter

As was mentioned earlier, over the last 150 years or so, it was gradually discovered that all matter was composed of a finite set of atoms which themselves are composed of even smaller particles. Atoms contain a nucleus of tightly bound neutrons and protons surrounded by a diffuse cloud of electrons. The electrically charged particles experience electromagnetic interactions mediated by massless, chargeless photons. The neutrons and protons are composed of smaller quarks which interact with each other through the strong force in addition to the electromagnetic force. Figure 2.1 arranges the fundamental particles from which all other composite particles are made

along with some of their basic properties. While electrically charged particles may have either of two charges, positive or negative, there are three color charges that govern strong force interactions. This makes the theory describing the strong force much more complex than electromagnetic theory. The particle that mediates the strong interaction is the massless gluon. The photon in the electromagnetic interaction does not possess electric charge and therefore does not interact electromagnetically with other photons. In contrast to this, the gluon does contain color charge and so interacts, not only with the quarks, but with other gluons through the strong force. This further complicates the theory describing strong interactions making calculations with the theory extremely difficult.

There are a few other fundamental particles. In addition to the electron there is another type of lepton, the nearly massless neutrino which interacts only through the weak force which is mediated by massive W^+, W^-, and Z bosons. The weak force is responsible for the radioactive decay of unstable nuclei. There are three generations of particles with many similar properties but different masses. Also, for each of the quarks and leptons in Figure 2.1 there is a corresponding anti-particle.

Hadrons are composite states built from various combinations of quarks and anti-quarks. Hadrons come in two types. Mesons are composed of two constituent particles, a quark-anti-quark pair, while baryons are composed of three constituent particles, also some combination of quarks and anti-quarks. Discovery of heavier and heavier hadrons came historically as higher and higher energy accelarators were built. It takes more energetic collisions to create heavier particles but even so the lightest particles are produced in larger numbers (higher multiplicities) as the collision energy is increased. In relativistic heavy ion collisions, most of the observed particles,

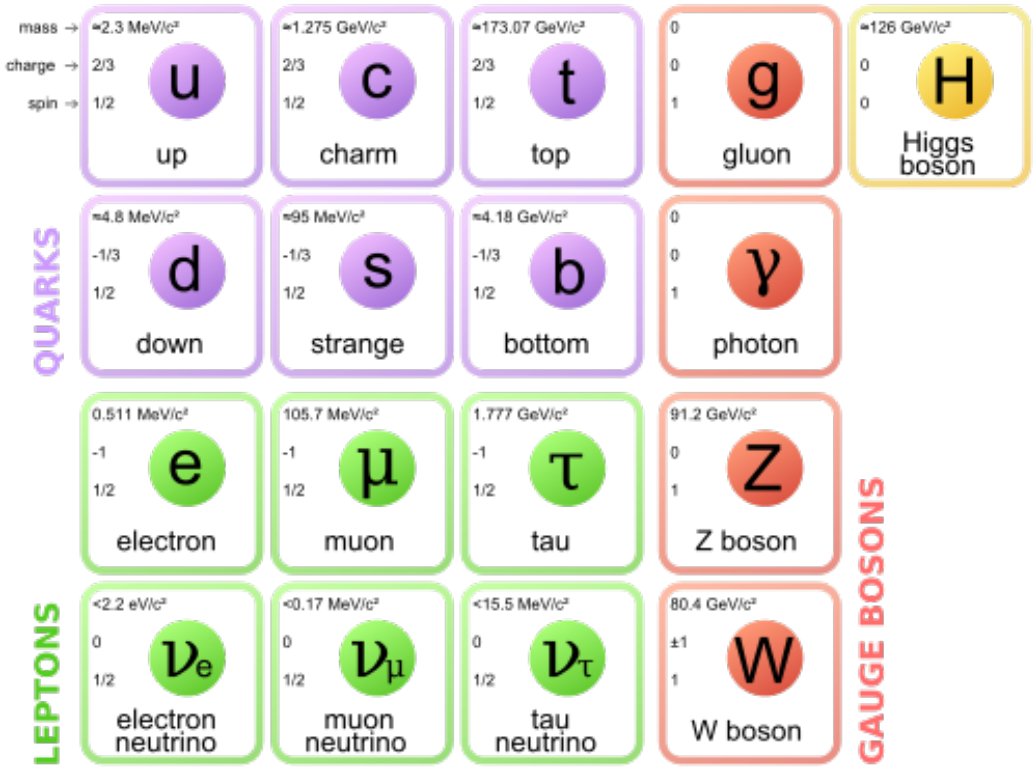

Figure 2.1: Chart summarizing the fundamental particles [9]. The first three columns show the three generations of quarks and leptons. The Higgs boson is a new addition to the chart as it was only recently discovered.

about 90%, are pions, the lightest meson. Charged pions are the particles used in this analysis. Of course, the only stable composite particle is the lightest baryon, the proton. Heavier baryons are unstable and decay to lighter particles. Neutrons are stable over a long period of time in various stable nuclei due to being bound inside the potential well of the nuclei. However, even neutrons are unstable when free or when in radioactive nuclei. All mesons are unstable as well.

In particle collisions the interactions may occur between fundamental particles, quarks and gluons for instance, but the observed particles are the mesons and baryons, as well as leptons and photons, that are formed and which stream out into the detectors. The observed particles, and their relative numbers and patterns of momentum and spatial distribution, are used to infer information about the fundamental interactions and properties of the medium produced in the collisions.

The material that is most difficult to study is that composed of unbound quarks and gluons because they have been so tightly bound inside nucleons since a microsecond after the big bang. To study interactions of quarks and gluons and experimentally explore Quantum Chromo-Dynamics (QCD), the theory describing strong force interactions, requires colliding particles at extremely high, ultrarelativistic energies in particle accelerators. While proton+proton collisions can be used to study simple interactions between the quarks and gluons, nucleus+nucleus collisions smear together many protons and neutrons at the same time. At sufficiently high energy densities the nucleons should overlap. Instead of a gas of interacting hadrons (particles with quarks still bound inside) the interactions are between quarks which form a bulk liquid medium. In the high energy density many additional quarks and anti-quarks are formed by pair production. This medium of deconfined quarks and gluons is often

referred to as the strongly coupled Quark Gluon Plasma (sQGP). The material is hot and dense. It evolves, expanding, cooling, and eventually freezing out into composite particles which may be measured in the detectors. Certain aspects of how the collisions evolve are intimately related to the research in this thesis so we will review these basic, relavent, aspects of the evolution of the collisions in further detail.

2.2 Evolution of a heavy ion collision

When two heavy nuclei collide the system is believed to evolve through several states that may be depicted using a space-time diagram shown in Figure 2.2. The two nuclei approach each other along the lines defining the lower cone and collide at the vertex. After the collision, the pieces of nuclei, spectators, that do not participate in the collision (for instance in non-central collisions), continue down the beam pipe (near the lines defining the upper cone in the diagram). These so called fragmentation regions are at very forward and backward "beam" rapidities, y_{beam} where rapidity is defined as

$$y = \frac{1}{2} \ln \left(\frac{E + p_z}{E - p_z} \right). \tag{2.1}$$

The maximum momentum in the longitudinal direction, p_z, that a particle can have is determined by the beam energy. At higher energy, therefore, the beam rapidity, y_{beam} increases. A second beam in the opposite direction has negative beam rapidity and so as the energy of two colliding beams increases, the rapidity window, Δy, increases and the regions near beam rapidity become more separated from the mid-rapidity region.

At sufficiently high collision energies it is believed that a bulk medium is formed. It cools and emits particles primarily into the mid-rapidity region (the central part

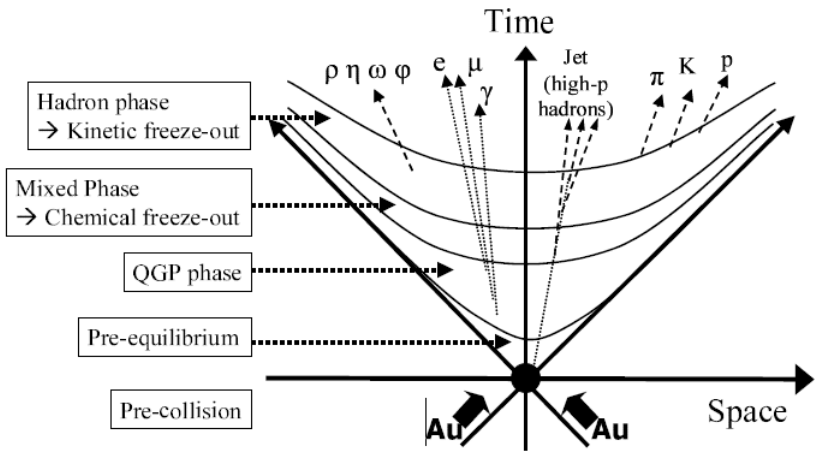

Figure 2.2: Space-time diagram demonstrating the evolution of a heavy ion collision. Figure is from Reference [10].

of the upper space-time cone). The medium that is produced evolves through several stages also shown in the diagram. Just after the collision, the system takes some time to reach thermodynamic equilibrium. This process is believed to take ≈1 fm/c. During a subsequent period, lasting very roughly ≈10 fm/c, the system undergoes hydrodynamic expansion as a result of pressure gradients in the compressed fluid. As the system expands, it cools. If the medium is deconfined then at some temperature the partons will form back into hadrons. If the phase transition is first order then the system passes through a mixed phase. Once the system is composed of re-formed hadrons, the particles may still undergo interactions that change ratios of the particle species. At a sufficiently low temperature, $T_{\rm ch}$, chemical freeze out occurs and the particle yields are frozen. Still, final-state interactions between the hadrons (Coulomb interactions for instance) may change the particles' momentum distributions. At some temperature, when the system has expanded and cooled enough, to a temperature,

$T_{\rm kin} \approx 120$ MeV/c, kinetic freeze out occurs. The freeze-out process takes ≈2-3 fm/c. The particles free stream away from the collision vertex, out into the detectors. These are the main stages in the evolution believed to occur at sufficiently high collision energies achieved at RHIC and the LHC. The picture may change as the collision energy is lowered. Observing such changes can be explored in a Beam Energy Scan which has been carried out recently at RHIC. This program is reviewed in detail in Chapter 3.

2.3 Relavent nuclear processes

Even though the particles measured and used in this analysis, low momentum pions, reflect the state of the system at freeze-out, the state of the system during this late stage depends upon the entire prior evolution of the system and the type of material of which it was composed as it evolved. Because the material is compressed to such a hot, dense state, pressure gradients are created which drive the system to expand in both the transverse and longitudinal directions. These are decoupled at high energies, so the discussion in this section should apply to collisions obtained at the AGS, SPS, RHIC, and the LHC [11]. In the transverse plane, central collisions will experience radial flow, expansion in the outward direction. In collisions at non-zero impact parameter, however, the initial shape of the collision region is approximately an ellipse. Although initial state fluctuations in positions of participant nucleons may cause deviation from this shape [12], the primary second order anisotropy remains approximately elliptical. In this case, the initial spatial anisotropy causes stronger pressure gradients to develop along the short axis of the ellipse (the reaction plane

containing the impact parameter and beam direction) which in turn causes preferential expansion in the reaction plane compared to the out-of-plane direction. The shape of the region becomes more round as the system expands and cools. In non-central collisions, the variation of pressure gradients boosts the momentum of the particles preferentially in the reaction plane direction. Therefore, more particles are emitted in the reaction plane causing an azimuthal anisotropy, in momentum space, that is a function of transverse momentum, p_T. This anisotropy is generally represented by the Fourier decomposition

$$E\frac{d^3N}{d^3p} = \frac{1}{2\pi p_T}\frac{d^3N}{dp_T dy}(1 + \sum 2v_n(p_T)\cos[n(\phi - \Psi_r)]) \tag{2.2}$$

in which the Fourier coefficients, v_n, reflect the amplitude of the variation relative to the n^{th} order event plane. An event plane is an estimate, with imperfect resolution, of the true reaction plane determined either by the azimuthal distribution of observed particles or by the spectator particles that proceed near the beam pipe at large rapidity. The details of the event plane calculations are left for Chapter 6. If the direction of the impact parameter can be reliably estimated, v_1 can be measured which reflects the strength of the so called directed flow. If only the reaction plane is estimated (with the direction unspecified) this allows determination of the 2^{nd} order coefficient, v_2, which corresponds to elliptic flow. These first two coefficients are most related to the hydrodynamic description of the collision evolution because it is the initial first and second order anisotropy of the collision geometry that should generate related first and second order anisotropy of the pressure gradients. Higher order coefficients like v_3 (triangular flow) can also be extracted. The higher order coefficients likely arise due to initial state fluctuations of the particpant nucleons that cause deviations from precise initial elliptical geometry [12]. The beam energy

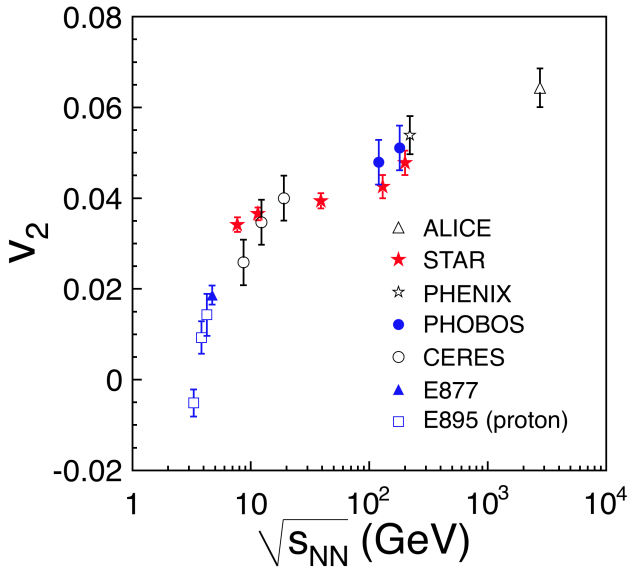

Figure 2.3: The elliptic flow coefficient, v_2, integrated over low p_T shows a monotonic increase with beam energy [13].

dependence of the momentum space anisotropy, v_2, integrated over p_T is shown in Figure 2.3. It appears to increase smoothly at higher energies although a plateau may possibly develop in the 10-100 GeV region.

While the pressure gradients should drive the system toward a more round shape, a couple of other factors are important to consider. First, if the lifetime of the system increases at higher energies then, even if the pressure gradients were the same at all energies, the system would experience the pressure gradients for a longer time before freeze-out. The longer the preferential in-plane expansion occurs the more round the shape becomes. A stronger difference between in-plane and out-of-plane pressure gradients, a longer lifetime, or both, should result in a monotonic decrease in the

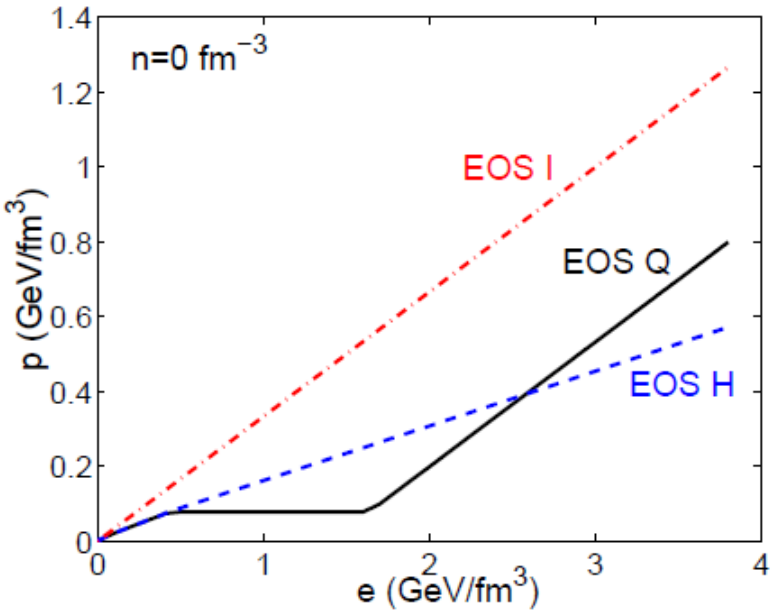

Figure 2.4: Equations of state for a hadronic gas (EOS-H), an ideal gas of massless quarks (EOS-I), and for a system with a first order phase transition between the two (EOS-Q) [14].

shape as a function of beam energy. Second, the time spent in different phases of matter could affect the beam energy dependence of the freeze-out shape.

Phase transitions may leave an imprint on the freeze-out shape. Three different equations of state are shown in Figure 2.4. One is for a hadron gas, EOS-H, another for an ideal gas of massless quarks, EOS-I, and a third which incorporates a phase transition between the two, EOS-Q. The pressure gradients are stronger in the deconfined case the $c_s^2 = dp/d\epsilon = 1/3$ compared to the hadronic case $c_s^2 = 1/6$ [14]. Figure 2.5 shows two two-dimensional hydrodynamical model predictions showing the time evolution of the participant zone shape when two different equations of state

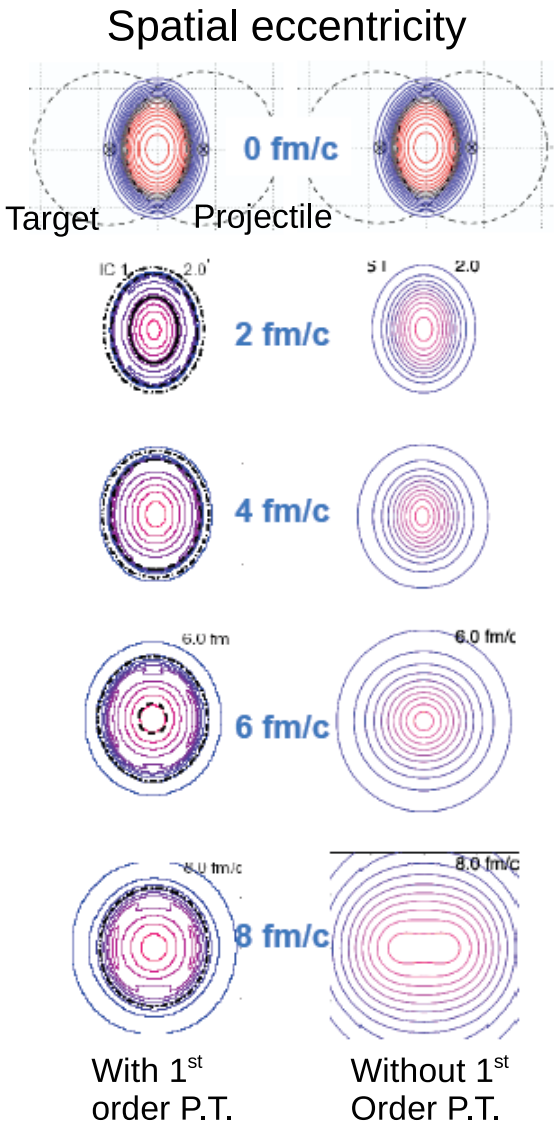

Figure 2.5: Two-dimensional hydrodynamical evolution of the freeze-out shape for two different equations of state [14].

are specified. In one case the matter experiences a first-order phase transition from a deconfined ideal gas of quarks and gluons back to a hadron gas state. When the phase transition is included the model predicts a more out-of-plane extended, elliptical shape [14]. This may be due to the time spent in the mixed phase during which the pressure gradients vanish (the flat segment in Figure 2.4). During this mixed phase the change in shape would not be accelerating.

Clearly there is a direct connection between the initial pressure gradients and the final shape. The size of the momentum space azimuthal anisotropy, v_2, is determined by the difference in pressure gradients in-plane and out-of-plane and system lifetime. The relative strength of these pressure gradients determines how much the system changes from an out-of-plane extended ellipse to a more round shape at freeze-out. The final elliptical shape of the collision can be quantified by its freeze-out eccentricity, ε_F. The method of extracting this from the data and the mathematical definition are described in Chapter 6 but qualitatively ε_F is positive for an out-of-plane extended elliptical shape, zero for a round shape, and negative if the shape evolves to an in-plane extended ellipse. If the nature of the phase transition changes from a rapid crossover to first order transition, which requires passage through a mixed phase, ε_F may exhibit non-monotonic dependence on collision energy. Prior to the Beam Energy Scan at RHIC a few prior measurements of ε_F were performed by E895 at 2.7, 3.32, and 3.84 GeV [15], CERES at 17.3 GeV [16], and STAR at 200 GeV [17]. These are summarized in Figure 2.6.

There is a suggestion of non-monotonic behavior with a minimum near 17.3 GeV. However, these measurements were carried out using different detectors with different acceptance regions and variations in the analysis details. While a minimum is

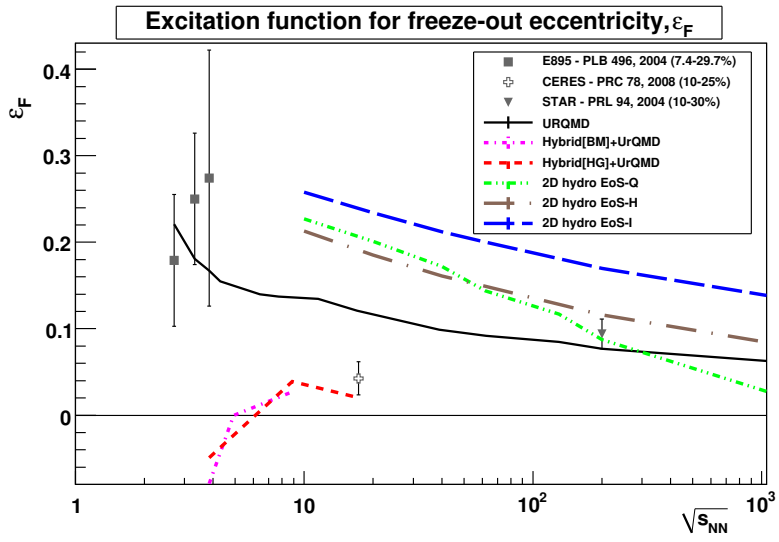

Figure 2.6: Existing measurments of the freeze-out eccentricity, ε_F, [15–17] and model estimates [8, 14] prior to the Beam Energy Scan program.

suggested, the statistics and number of measurements were too few to rule out that this could simply be due to random fluctuations. However, to explain this possible non-monotonic behavior two scenarios were speculated to be possible in [8] which are discussed here. In the first scenario the material begins to enter a mixed phase near 17.3 GeV. As the energy is increased it simply increases the concentration of deconfined material in the mixed phase without increasing the temperature, indicative of a latent heat during the phase transition, and the time spent in the mixed phase may increase. During that time the lack of pressure gradients mean the expansion is not accelarating and the eccentricity plateaus with $\sqrt{s_{NN}}$. At some higher energy, perhaps around 200 GeV, the material is completely deconfined and the pressure gradients reappear. Beyond that point the eccentricity would again drop with collision

energy. In the second scenario the behavior is instead related to changes in the lifetime of the system. Somewhere around 17.3 GeV deconfinement begins resulting in an increase in the lifetime of system as it coasts through the mixed phase. A more round shape is obtained. As the collision energy is increased, however, the lifetime of the system decreases and shape evolves less toward a round shape. This may be consistent with a faster evolution in which the passage through the mixed phase is shorter due to more rapid expansion prior to the mixed phase.

The available model predictions prior to the Beam Energy Scan are also interesting. The hydrodynamic models with equations of state shown in Figure 2.4 tend over predict the available data. Also, no models predict a rise in the eccentricity with collision energy. However, the magnitude of the freeze-out eccentricity predicted using different equations of state are clearly different. Measuring the freeze-out eccentricity can place new constraints on the models. The models shown in Figure 2.4 and more recent models will be discussed in more detail in Chapter 9.

In any case, extracting the beam energy dependence of the freeze-out eccentricity is the main subject of this thesis. Performing the analysis with the same detector, analysis techniques, and acceptance cuts will allow unambiguous determination of the freeze-out shape and determine whether or not there is really any non-monotonic behavior. Details of the techniques used to extract the freeze-out shape of the system are described later in Chapters 5 and 6. This study is part of a larger Beam Energy Scan program designed to map out features of the QCD phase diagram. The next chapter provides an overview of this Beam Energy Scan program, placing the current research within this larger context.

2.4 Thermodynamic description of nuclear matter

The previous section outlined a scenario in which the material produced in the collision of two heavy nuclei undergoes hydrodynamic evolution. In such a scenario the system may be described by thermodynamic quantities such as temperature, T, pressure, P, energy density, ϵ, particle number density, η, entropy density, s, and chemical potentials, μ of different types. This section is not intended as a comprehensive review of thermodynamics but simply as a brief overview to promote some discussion of important concepts that will be mentioned later, especially regarding the phase diagram in the next chapter.

The matter produced in a heavy ion collision may exist in different states at different times during its evolution depending on the collision energy. Since particles may flow out of the system, thermodynamically the system should be described by a Grand Canonical Partition Function. In this case, a chemical potential, μ, determines what types of particles may be emitted. Conserved quantities play an important role. As an example, baryon number is conserved in the collision. The incoming nuclei already have a net baryon number. The material produced at mid-rapidity may contain a large fraction of particles from pair production of quarks and anti-quarks as well which contribute no additional net baryon number. At lower collision energies the net baryon density at mid-rapidity increases, as does the baryon chemical potential, μ_B. A larger value of μ_B ensures that more net baryons will be produced in collision and also ensures that the net baryon number is conserved during any phase transitions that may occur in the collisions.

The form of the partition function depends on the state of matter formed in the collisions and which assumptions or approximations may be imposed for simplicity

(can particles be treated as massless, for example). If a quark-gluon plasma is formed the partition function will include contributions from gluons (bosons) and quarks (fermions) with some number of quarks specified (often u, d, and s are included). If the system is a hadron gas instead, the partition function must account for mesons (bosons) and baryons (fermions). An example Grand Canonical Partition function, Eq. 4.124 in Reference [18], is

$$\ln Z(T,\mu,V) = \frac{gV}{2\pi^2 T}\int_0^\infty \frac{dkk^4}{3E}\left[\frac{1}{e^{(E-\mu)/T}\mp 1} + \frac{1}{e^{(E+\mu)/T}\mp 1}\right] \tag{2.3}$$

where k is the particle momentum, $E = \sqrt{m^2+k^2}$ is the particle energy, and g is the degeneracy factor for the particle. In this equation the positive sign is for fermions and the negative sign is for bosons. Also, the term with $(E-\mu)$ accounts for particles while the term with $(E+\mu)$ accounts for antiparticles because they will have equal and opposite chemical potentials. Several terms of this form may be added to account for more complex systems with multiple types of particles and anti-particles.

The partition function is determined once the relavent Bose-Einstein or Fermi-Dirac distributions are included for all the particles and anti-particles in the system, any simplifying approximations are applied, and the degeneracies of the particles are computed. Ref. [18] provides a thorough derivation for several different scenarios as examples.

Once the partition function is constructed, the free energy is simply

$$F = -T\ln Z. \tag{2.4}$$

Free energy is the available energy that may be taken out of the system to do some useful work on the surrounding environment. The free energy allows calculation of

thermodynamic quantities using standard relationships

$$\eta = \frac{T}{V}\frac{d\ln Z}{d\mu}, \tag{2.5}$$

$$\epsilon = \frac{T^2}{V}\frac{d\ln Z}{dT} + \mu\eta, \tag{2.6}$$

$$P = -\left(\frac{dF}{dV}\right)_T = -\left(\frac{d(-T\ln Z)}{dV}\right)_T, \tag{2.7}$$

and

$$s = \frac{1}{V}\frac{dT\ln Z}{dT}. \tag{2.8}$$

A phase transition requires that certain criteria be met in order to occur. The pressure, temperature and chemical potential must remain equal in the transition [18]. As mentioned earlier, the baryon chemical potential is conserved during the collision, regardless of whether the material is in a deconfined quark-gluon plasma state or a hadron gas state. When the phase transition occurs the criteria above are met and are constrained by any conservation laws. The next chapter outlines the $T-\mu_B$ phase diagram that describes nuclear matter and how it can be explored by looking at a variety of observables at different energies.

Chapter 3: The Beam Energy Scan

The first phase of a Beam Energy Scan (BES) recently performed at RHIC was designed to map out expected features of the QCD phase diagram depicted in Figure 3.2. This is accomplished by varying the energy of the collisions. In Au+Au collisions, the incoming nuclei have a net baryon number, B=394, which is conserved in the collision. As the collision energy is lowered, the rapidity window narrows as demonstrated in Figure 3.1. Specifically, as the beam energy is reduced from $\sqrt{s_{NN}} = 200$ GeV down to 7.7 GeV the rapidity window ($\Delta y = 2y_{\text{beam}}$) decreases from 10.8 units of rapidity down to 4.18 units of rapidity. The rapidity density of net baryon number, dN_B/dy, must increase as the beam energy is reduced. More initial baryon number in the mid-rapidity region, where measurements are made ($y \approx< 1$ for STAR), means a larger number of net baryons will be produced in the final state. Such a higher potential for baryon formation is associated with a larger baryon chemical potential, μ_B. Measuring collisions at lower and lower energy during a Beam Energy Scan is equivalent to measuring material produced at larger and larger baryon chemical potential.

The next few sections describe the landscape of the QCD phase diagram, the questions the Beam Energy Scan is designed to address, and some observables that can be used to probe those questions. The current work is then placed in the context of this bigger picture.

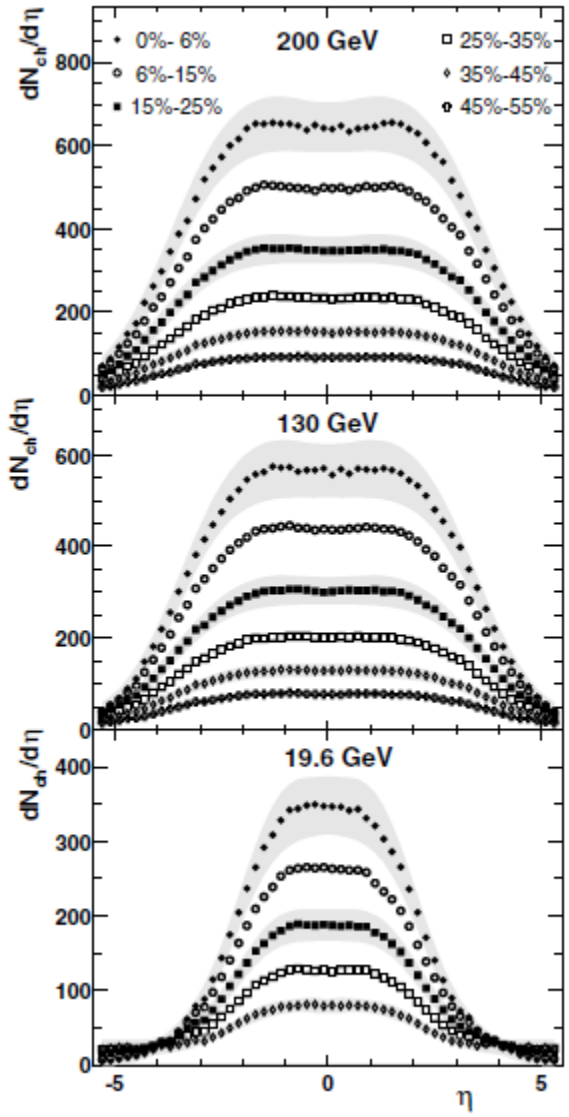

Figure 3.1: The pseudo-rapidity distribution for charged particles, $dN_{ch}/d\eta$ ($\approx dN_{ch}/dy$) narrows as the beam energy is reduced. Rapidity, y, and pseudo-rapidity, η, are nearly equal for the relativistic particles measured at RHIC. These results, from the PHOBOS collaboration, show the distributions for measured charged particles (including charged baryons) but the shape should hold for neutral baryons and mesons as well. This figure is taken from [19].

3.1 The QCD phase diagram

Figure 3.2 shows the main features that are expected to describe the various states of hot QCD matter. At low temperatures, T, and baryon chemical potential, μ_b, the material consists of a hadronic gas. The quarks are bound inside individual nucleons in the case of ordinary nuclei or baryons and mesons in more exotic situations (for instance the later stages of a heavy ion collision). At large enough baryon chemical potential a transition is expected to some other state of matter, perhaps a deconfined color super-conductor [20]. This type of material is hypothesized to exist in astrophysical contexts such as neutron star cores [20, 21] although recent observations of the highest mass neutron stars tend to disfavor such a scenario [22]. At high temperature a phase transtion is also expected from a hadronic gas to a strongly interacting fluid of quarks and gluons. This high temperature, low chemical potential region is expected to be most similar to the material in the early universe. This material with high T, low μ_b is the region produced and studied in heavy ion collisions.

Soon after a collision occurs some high temperature QGP material is created which evolves. The matter expands and cools along a trajectory through the phase diagram. Such paths are depicted on the phase diagram for different collision energies measured in the Beam Energy Scan. As mentioned above, decreasing the beam energy increases the baryon chemical potential of the produced material but also decreases the (initial) maximum temperature achieved. As the system evolves, the trajectories pass through different regions of the phase diagram.

The phase diagram contains several other important details. At low μ_b the transition from a deconfined fluid back to a hadronic gas state appears to be a rapid, smooth crossover transition [23–26]. At higher μ_b, however, the transition is expected

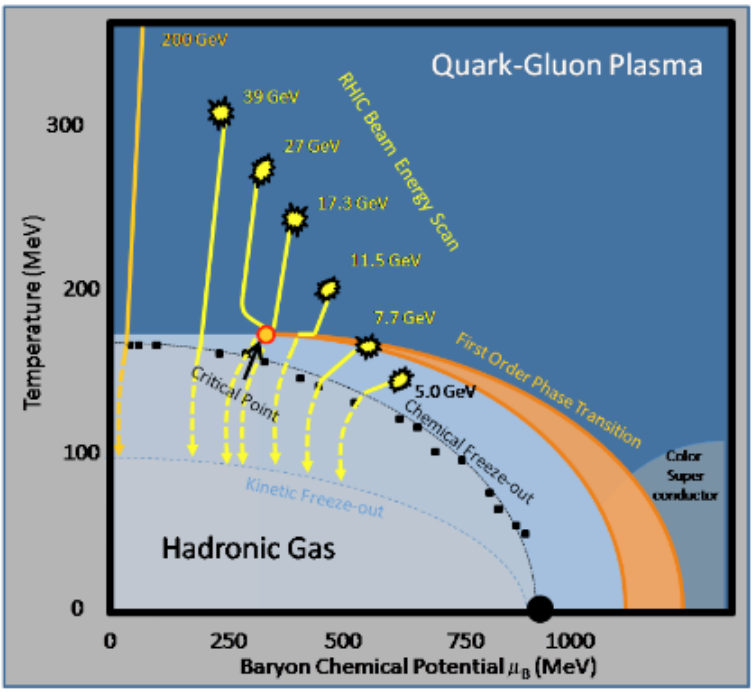

Figure 3.2: QCD phase diagram [7].

to change to a first order phase transition which would have an associated latent heat [27–35]. The system may spend part of its evolution in a mixed phase. A critical point is predicted to exist [36] that would lie at the boundary between the smooth crossover and the first order phase transition regions. There are theoretical predictions of the location of the critical point [37–41] but they are imprecise due to the difficulty of the calculations. Experimental identification of the critical point is needed in order to guide the theories [7]. It is important to note that the values on the diagram (e.g. T and μ_b of the critical point, maximum temperatures at each energy) are simply rough estimates for the purpose of illustration. The various features on the diagram are expected or predicted but the precise details are uncertain and must be determined experimentally.

Also shown on the diagram are lines defining both chemical and kinetic freeze out which occur after the system has returned to a confined, hadronic gas state. These features are also on the space-time diagram in Figure 2.2. In Chapter 2 the temporal evolution of a heavy ion collision was described in detail. That evolution is what occurs along the trajectories in the phase diagram. The initial highest temperature point for each energy is reached at the moment on the space-time diagram when the medium thermalizes, a requirement for a phase diagram to be a meaningful representation of the material [7]. The system expands and cools, passing back from a deconfined state to a hadronic gas and finally undergoing chemical and then kinetic freeze out.

The main features of the QCD phase diagram have just been described. The stages of evolution of the collisions were described in Chapter 2 and reviewed briefly in the previous paragraph. It was discussed above how lowering the beam energy allows

the collision to evolve through different regions of the phase diagram. Numerous observables may be used to study heavy ion collisions. Reference [7] includes an extensive summary of observables proposed to be studied in the Beam Energy Scan and what information each may provide. In the next section, a sample of these observables is reviewed to provide an outline of how different complementary analyses (including the current work) may lead to a better understanding of the QCD phase diagram.

3.2 Methods to probe the QCD phase diagram

Different observables probe different stages in the evolution of a heavy ion collision and are sensitive to different features in the QCD phase diagram. Some observables may be sensitive to the critical point if the system evolves along a trajectory that passes near the critical point in Figure 3.2. A different set of observables show behavior at high energies that is consistent with the formation of a deconfined state. It is interesting to perform the same measurements at lower energies to see if the behavior changes or disappears. A third set of observables may be sensitive to the type of phase transition through which the system evolves. In the rest of this chapter, representative examples of these observables are described. Earlier measurements that hinted at possibly interesting behavior, and therefore helped motivate the Beam Energy Scan, are discussed. In some cases, more recent results already available from the Beam Energy Scan are commented on, as well.

3.2.1 Searching for a critical point

The observables used to search for evidence of a critical point are primarily fluctuations of various quantities. Reference [7] lists flucuations of the following quantities

as being of interest: $\langle p_T \rangle$, K/π, p/π, K/p, v_2. Near the critical point lattice QCD suggests the susceptibilities for electric charge, Q, baryon number, B, and strangeness, S, diverge [42]. These are conserved quantities set at the beginning of the collision and should be preserved through subsequent evolution [43]. The large variations in susceptabilities may be reflected in different particle ratios for identified hadrons which would also show large fluctuations if the evolution trajectory passes near the critical point. Additionally, fluctuations in mean p_T and multiplicity may appear if the chemical freeze-out temperature is near to temperature at the critical point [44]. If one of the beam energies scanned were to pass close to the critical point the increased fluctuations would appear as non-monotonic behavior in that quantity as a function of beam energy.

Some of these quantities have been observed before at the lower SPS and and at higher RHIC energies. The Beam Energy Scan remeasures some of these lower energies with higher statistics and fills in a wide gap in $\sqrt{s_{NN}}$ at higher energies with results from the same detector and the same (and more uniform) acceptance regions and with better and more complete particle identification. An example of this type of observable is the K/p fluctuation represented by the quantity [45]

$$\sigma_{\rm dyn} = sign(\sigma^2_{\rm data} - \sigma^2_{\rm mixed})\sqrt{|\sigma^2_{\rm data} - \sigma^2_{\rm mixed}|} \tag{3.1}$$

where $\sigma_{\rm data}$ and $\sigma_{\rm mixed}$ are the ratios of standard deviation to the mean of a given particle ratio distribution (K/p, for instance) for the data and for mixed events. Subtracting the mixed event distribution helps remove fluctuations with unphysical cause, from imperfect particle identification on an event-by-event basis, for instance [45]. The definition of σ_{dyn}, makes it easy to see how fluctuations in a particle ratio will affect the width a simple distribution. A closely related quantity $\nu_{dyn,i/j}$ is defined

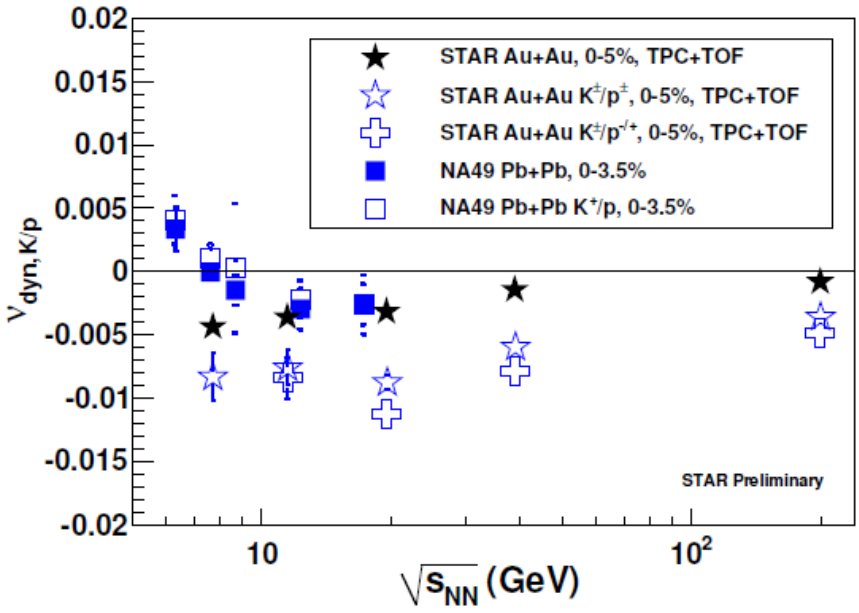

Figure 3.3: Results from NA49 [47] and STAR [46] suggested $\nu_{dyn,K/p}$ (and $\sigma_{dyn,K/p}$) had a sign change around 8 GeV and a minimum at slightly higher energy. More recent Beam Energy Scan results from STAR do not suggest such non-monotonic behavior [46].

rather in terms of physical correlations of particles (letting i=K and j=p here)

$$\nu_{\mathrm{dyn,K/p}} = \frac{\langle N_K(N_K-1)\rangle}{\langle N_K\rangle^2} + \frac{\langle N_p(N_p-1)\rangle}{\langle N_p\rangle^2} - 2\frac{\langle N_K N_p\rangle}{\langle N_K\rangle\langle N_p\rangle}. \tag{3.2}$$

The last term will become more significant if there are correlations between K and p particles that are generated in the collisions. The relationship between these two quantities is $\nu_{dyn} \approx \sigma^2_{dyn}$ [46]. The definition of ν_{dyn} makes it is easier to see how fluctuations arise from changes in the correlation of the production of particles of different types. The beam energy dependence of ν_{dyn} is shown in Figure 3.3.

Event-by-event fluctuations in the susceptibilities may produce large fluctuations in the number of baryons and the number of particles with strange quark content.

Near the critical point larger fluctuations might increase or decrease $\sigma_{\rm data}$ in Equ. 3.1 and, therefore, $\sigma_{\rm dyn}$. These flucuations may be observed in $\sigma_{\rm dyn}$ and $\nu_{\rm dyn}$ for ratios of kaons to protons, proxies for the strangeness and baryon number ratio, respectively. This is simply because kaons have non-zero strangeness (S=-1) and no baryon number (B=0), whereas the protons (S=0, B=1) are the exact opposite. In Figure 3.3, the NA49 results and STAR results at higher energy suggested a sign change around 8 GeV and a minimum at slightly higher energy. The change from positive to negative values at low energies in Figure 3.3 may be related to a modification in the correlation of strange and baryonic particles. This would increase the last term in Eq. 3.2 causing the values to turn negative. If the collision evolves near the critical point a large increase in strange particles may cause the K value in K/p to fluctuate. The non-monotonic behavior suggested by the NA49 results made this an interesting fluctuation observable to study in more detail.

Recent Beam Energy Scan results from STAR (the low energy STAR data in Figure 3.3) suggest that this sign change for $\nu_{dyn,K/p}$ does not occur (similar to results for other particle ratios). Ref. [48] suggests this difference in results is due to differences in the phase space probed by the two experiments. However, the discussion demonstrates how fluctuation measurements may potentially reflect the presence of a critical point near the evolution trajectory at some beam energy. This is why fluctuations studies are an important part of the Beam Energy Scan program.

3.2.2 Low energy turn off of QGP signatures

At high energy two of the most compelling cases for creation of a deconfined state are the scaling of v_2 for different identified particle species with the number of constituent quarks and the suppression of high momentum particles in central collisions relative to peripheral collisions, R_{cp}. The elliptic flow coefficient, v_2, was described in the previous chapter. If the azimuthal anisotropy of the pressure gradients is acting on particles in a deconfined, thermalized state then all the quarks would experience a similar preferential boost to higher momentum in the reaction plane direction. Hadrons formed from these quarks would reflect this by exhibiting a larger azimuthal momentum space anisotropy, v_2. After re-forming into hadrons, baryons would tend to have a larger v_2 compared to mesons by a factor of 3/2, simply due to the different number of constituent quarks, N_{cq}. In the baryon case they are formed from three quarks, each of which experienced a similar momentum boost. On the other hand, the mesons only contain two particles that experienced a similar boost. Such behavior is observed at intermediate p_T, Figure 3.4, where v_2 is plotted against the reduced transverse mass, $m_T - m_0$. After scaling identified particle v_2 (and $m_T - m_0$ in this case) by the N_{cq} value appropriate for each particle species, the results follow a common curve, as seen in Figure 3.5. It was pointed out in Reference [49] that the quantity v_2/N_{cq} would represent the common v_2 for the individual quarks in the deconfined state. While this is not conclusive proof of deconfinement, it is necessary if deconfinement does occur and is corroborated by other observations consistent with deconfinement. If the results for lower energy collisions no longer show this N_{cq} scaling, it would suggest that at lower energy the material is not entering into a deconfined state. The QGP signature would be said to have turned off.

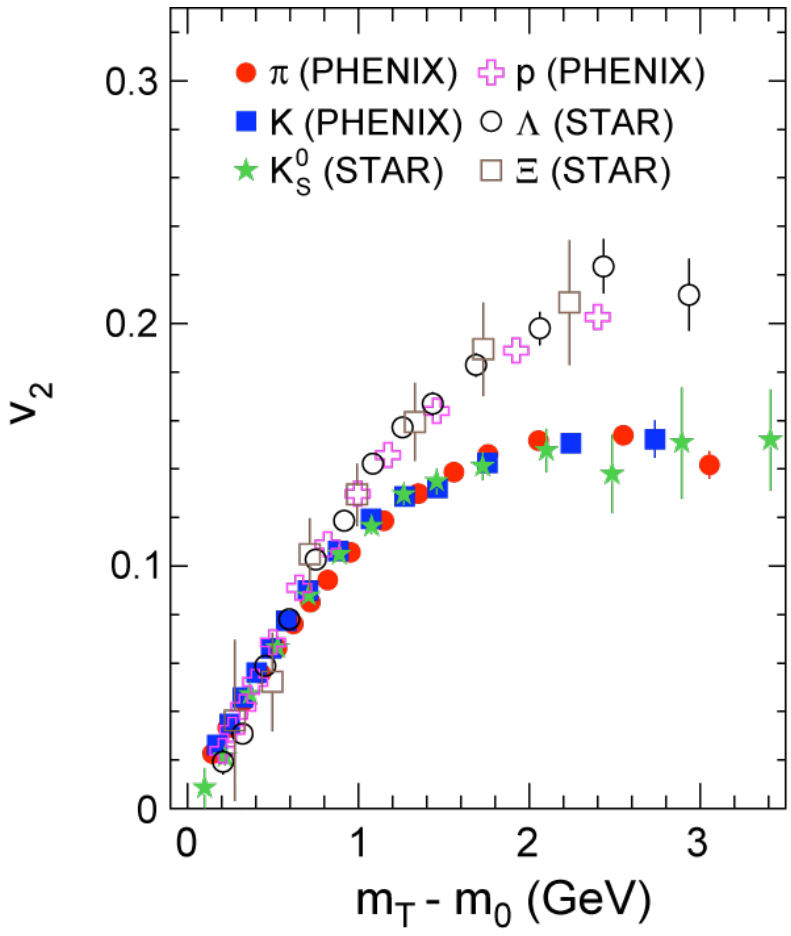

Figure 3.4: Elliptic flow, v_2, for identified particles follows two trends depending on the number of constituent quarks, N_{cq}, in the particle [7].

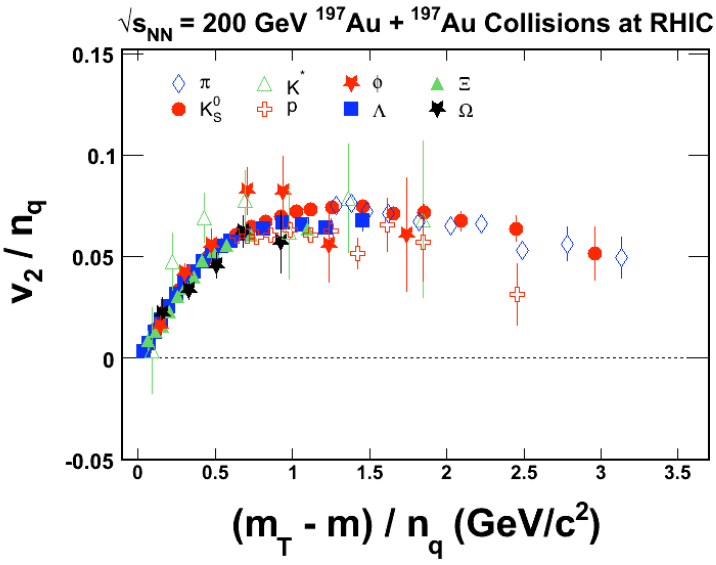

Figure 3.5: The quantity v_2/N_{cq} shows that after scaling by the number of constituent quarks, N_{cq}, all particles follow the same trend [7].

Recent results from the Beam Energy Scan do in fact show some breaking of N_{cq} scaling. As Figure 3.5 demonstrates, at $\sqrt{s_{NN}} = 200$ GeV, the v_2/N_{cq} for particles follows the same trend as for anti-particles. At lower energy, however, v_2, and therefore v_2/N_{cq}, for particles and anti-particles no longer agree [50]. Figure 3.7 shows that the p_T independent difference in anti-particle and particle v_2 increases as the energy is lowered, especially for baryons, which may possibly be due to increased importance of hadronic, rather than partonic, interactions [50].

Another important signature for QGP formation is the suppression of high p_T particles. High p_T particles are primarily produced early in the collisions due to hard scattering of quarks that produce jets of particles. The belief is that in a strongly interacting deconfined medium, high p_T partons lose energy which is transferred to

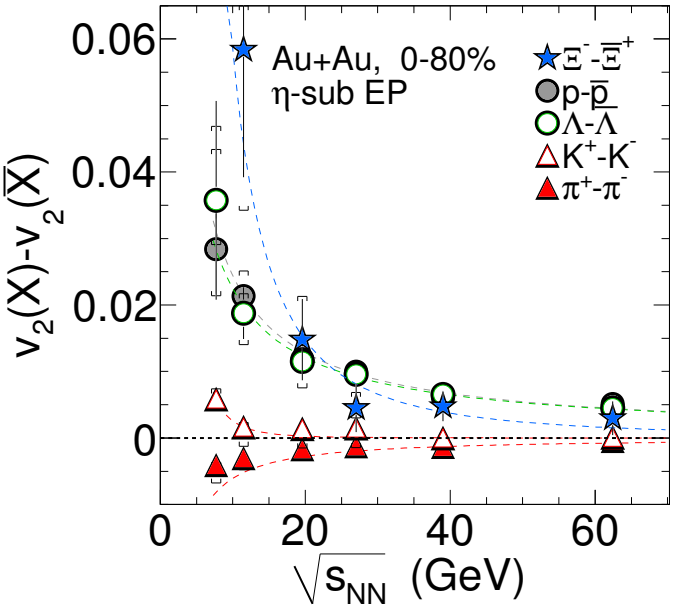

Figure 3.6: Energy dependence of the p_T independent difference in v_2 for particles and antiparticles [50]. In other words, the difference in v_2 for particles and antiparticles is plotted as a function of p_T which is then fit with a constant, horizontal line to extract the difference independent of p_T. The results also use $v_2(p_T)$ values in the centrality range 0-80%.

the bulk medium. The observable R_{cp} provides a useful way to view the effect of the medium on high p_T particles. In central collisions a larger volume of medium is produced so on average high p_T particles will pass through more of the medium compared to peripheral collisions. The yields of particles in central and peripheral collisions can be measured and normalized by the number of binary collisions in each case. The ratio of these yields, R_{cp}, must be one if no medium effect occurs. If the particles do interect and lose energy in the medium there should be less high p_T particles and more intermediate and low p_T particles would appear. Such behavior is observed in 200 GeV collisions as Figure 3.7 demonstrates. In the figure, at $p_T \approx 2$ to 6 GeV/c, the splitting in R_{cp} occurs with the values for baryons being larger that for mesons. Recombination models can successfully reproduce this behavior by assuming the hadrons reform out of partons in a deconfined state [7, 49]. Therefore, like v_2/N_{cq} scaling this is another observable that suggests a phase transition has occurred at high energy. If this phenomena were to turn off at some lower energy it would suggest that the material may not enter into a deconfined state below some energy.

Measurements of R_{cp} from the Beam Energy Scan are now available and are shown in Figure 3.8. As the energy is lowered the suppression of particles decreases and the trend approaches one at higher p_T for 39 GeV. At still, lower energies the values of R_{cp} continue rising above one. The splitting of R_{cp} for baryons and mesons seen in Figure 3.7 also has been observed to disappear at lower energy [3, 51]. The Cronin effect, the rise of R_{cp} above one at intermediate p_T in d+Au collisions, is attributed to cold nuclear matter effects since a deconfined state is not expected [3]. Similar behavior is seen in the lowest energy Au+Au results and may be consistent with

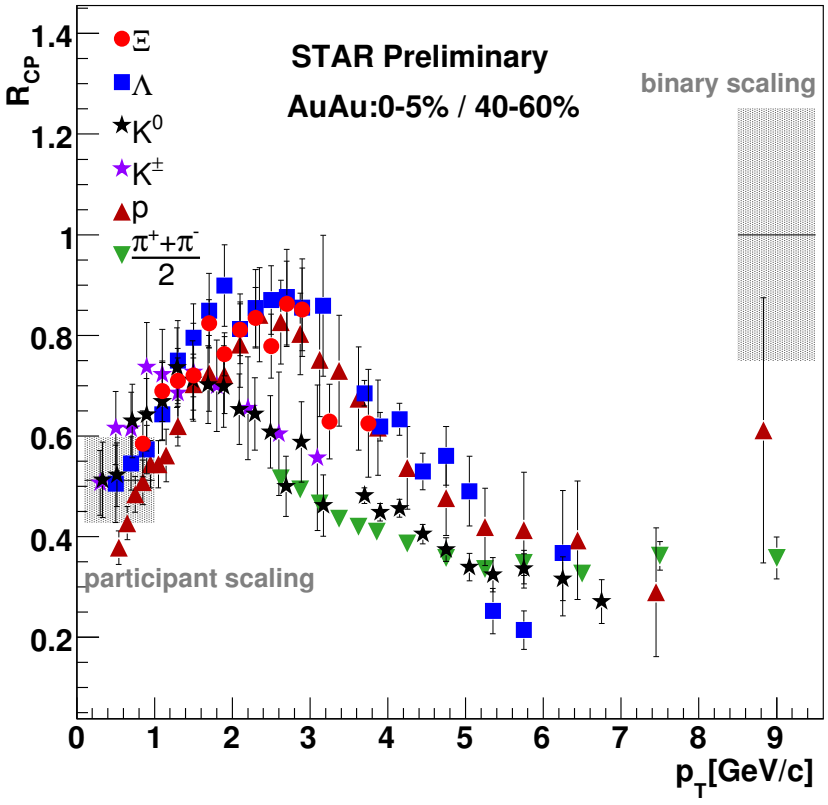

Figure 3.7: R_{cp} observed in 200 GeV Au+Au collisions [49].

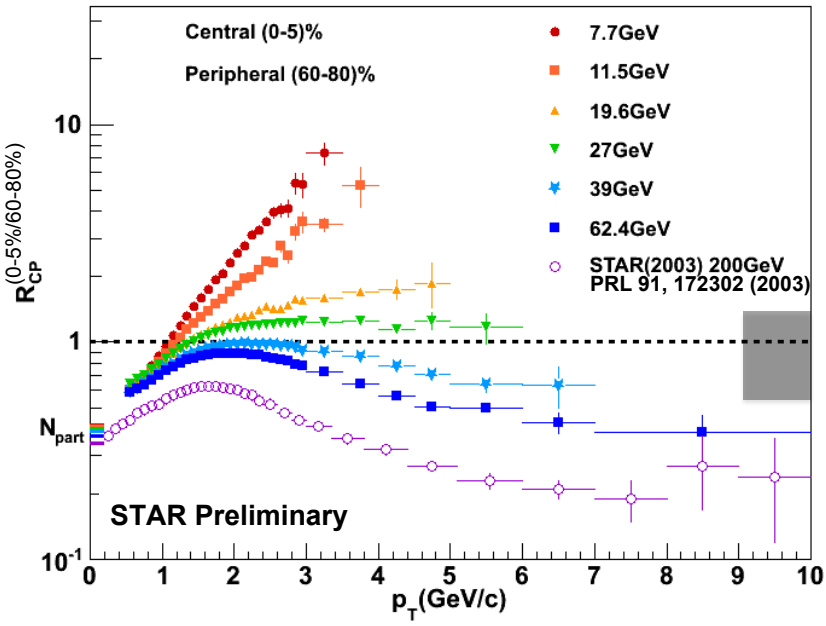

Figure 3.8: Beam Energy Scan measurements of R_{cp} from 7.7 to 200 GeV [51].

the disappearance of the effects attributed to a deconfined medium in higher energy collisions.

3.2.3 Evidence of a modified equation of state

If the energies scanned do not pass close enough to the critical point the variables described in Section 3.2.1 may be ineffective in identifying its location on the phase diagram. Even so, its location may be constrained using a different set of observables sensitive to the equation of state of the material throughout the collision evolution. A change in the type of phase transition may leave an imprint on the beam energy dependence of these quantities. Observing evidence of a change from a smooth crossover at one energy to a first-order phase transition at a lower energy

would constrain the location of on the critical point and provide guidance for more narrowly focused future studies [7].

As explained in Chapter 2, the current study measures the freeze-out eccentricity of the collision region, one example of an observable that may be sensitive to a change in the type of phase transition. At the same time there are some measurements from SPS, in this class of observable, that show interesting behavior that may be consistent with a change in the type of phase transition at lower energies. A few of these results are reviewed here.

At SPS, the K^+/π^+ ratio showed interesting non-monotonic behavior suggesting strangeness enhancement as seen in Figure 3.9 [52, 53]. The horn shape may be consistent with entrance into a mixed phase at the peak and complete deconfinement at the beginning of the plateau region. Assuming this, a closely related quantity measured only at SPS, $(\langle K\rangle + \langle\Lambda\rangle/\langle\pi\rangle$ shows a similar horn shape that was predicted by the SMES model [52]. The K^-/π^- ratio does not exhibit a peak. This is consistent with a scenario where strange quarks are generated by pair production in a deconfined state. The $\bar{s}$ quarks primarily form into K^+ mesons while s quarks are shared between K^- and Λ particles.

An alternative explanation in terms of associated production in hadronic interactions does not require formation of a deconfined state [54]. The argument is as follows. As the collision energy increases more strange particles are produced. In this scenario, particles with strange quark content are produced through hadronic interactions which may create kaons and hyperons (baryons with strange quarks). At low energy, this should primarily generate K^+ and Λ particles since they are the

lightest strange meson and strange baryon respectively. At low energy, baryon chemical potential is high which makes the creation of hyperons and K^+ more significant because producing a more significant fraction of hyperons helps conserve baryon number. At still higher energies, however, the baryon chemical potential becomes small and hadronic interactions that pair produce kaons become more favorable. In pair production K^+ and K^- are produced in equal amounts. Since the enhanced production of K^+ mesons to conserve baryon number decreases, the ratio K^+/π^+ decreases to a constant value. This may be due to the common mechanism, pair production, for both pions and kaons at these higher energies. A requirement of the statistical model that can explain the behavior of the K^+/π^+ ratio in this way is that the temperature does not exceed the critical temperature, $T_c \approx 170$ MeV, believed to be required for transition to a deconfined state [54].

At the same energies the slope of the p_T distributions were fit to extract the temperature. Figure 3.10 shows that a plateau in the temperature obtained by fits to kaon spectra emerges at SPS energies [52, 53]. This may be an indication that the medium is entering into a mixed phase indicative of a latent heat. Putting more and more energy into the system does not change the temperature but simply converts more and more of the system into a deconfined state. Above some energy the system would be completely deconfined and the temperature should rise again. As seen in Figure 3.10, the Beam Energy Scan confirmed this plateau in the lower energy region and filled in the region at higher energy. The new results suggest the plateau extends to at least 39 GeV before rising again.

In Reference [55] the speed of sound (pressure gradient) is extracted from measure pion rapidity distributions, dN_π/dy, and plotted as a function of beam energy. See

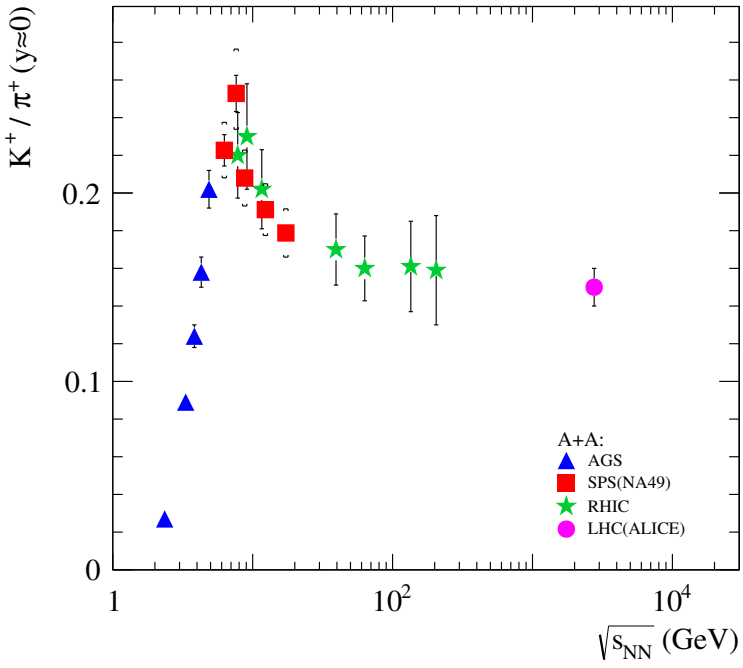

Figure 3.9: The K^+/p^+ ratio shows non-monotonic behavior as a function of beam energy. This figure is from [52]

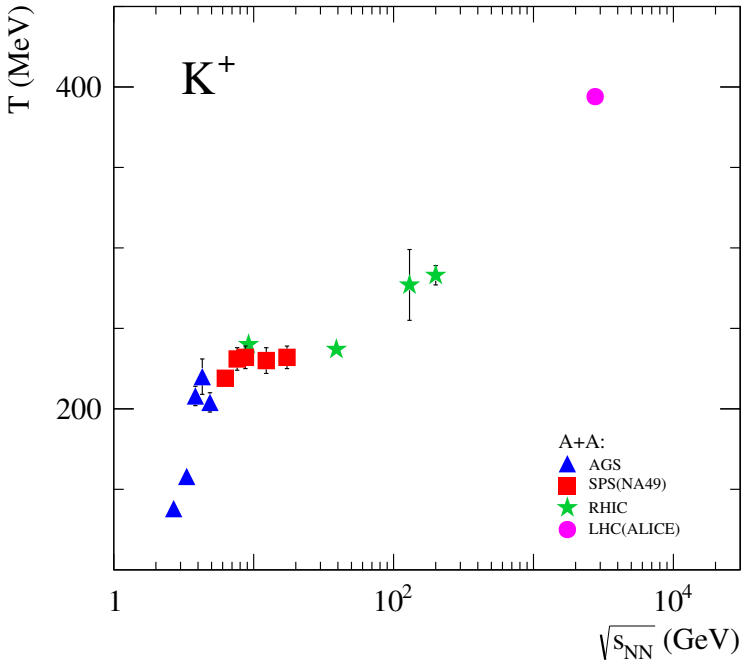

Figure 3.10: The kinetic freeze-out temperature extracted from kaon spectra appear to show a plateau at SPS energies. This figure is from [52]

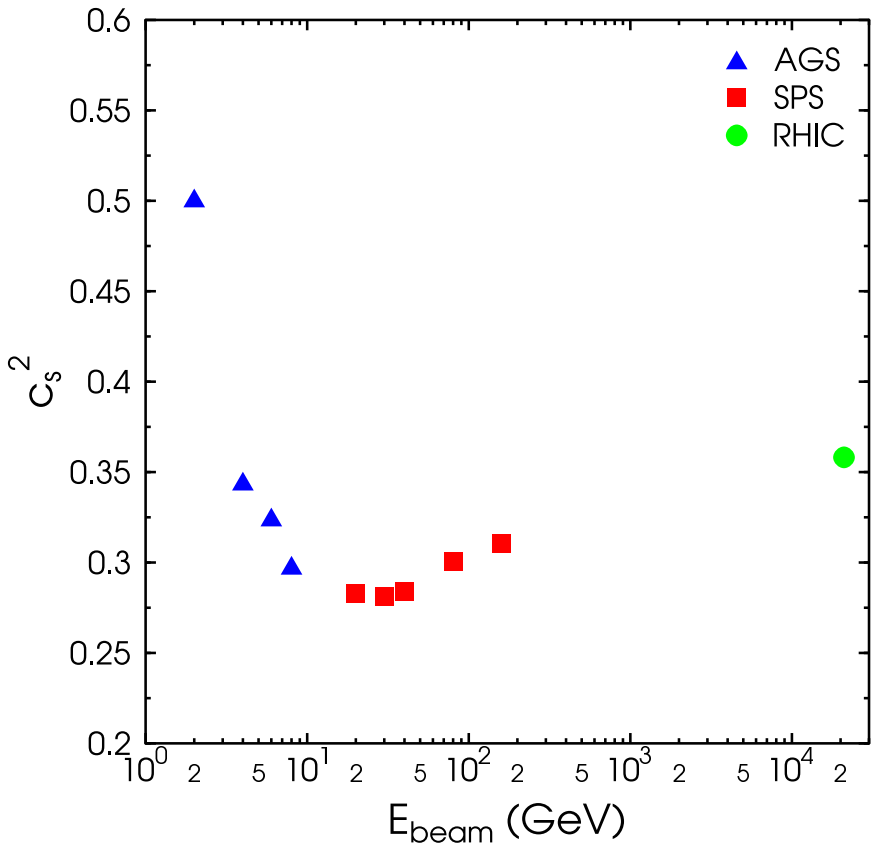

Figure 3.11: Beam energy dependence of the speed of sound (pressure gradients) extracted from experimentally measured pion rapidity distributions [55].

Figure 3.11. As discussed in Chapter 2, a mixed phase corresponds to a disappearance (or at least a minimum) of the pressure gradients. There is a clear minimum in Figure 3.11 at $E_{beam} \approx 30A$ GeV ($\sqrt{s_{NN}} = 5$ GeV) suggesting entrance into a mixed phase begins at this energy [55].

The flow coefficients v_1 and v_2 may also be sensitive to the type of phase transition since the pressure gradients that cause the azimuthal anisotropy disappear during the mixed phase in the case of a first order transition. In the case of $v_2(p_T)$, Figure 3.12 shows that the strength in different p_T ranges exibits a plateau at higher energies. This

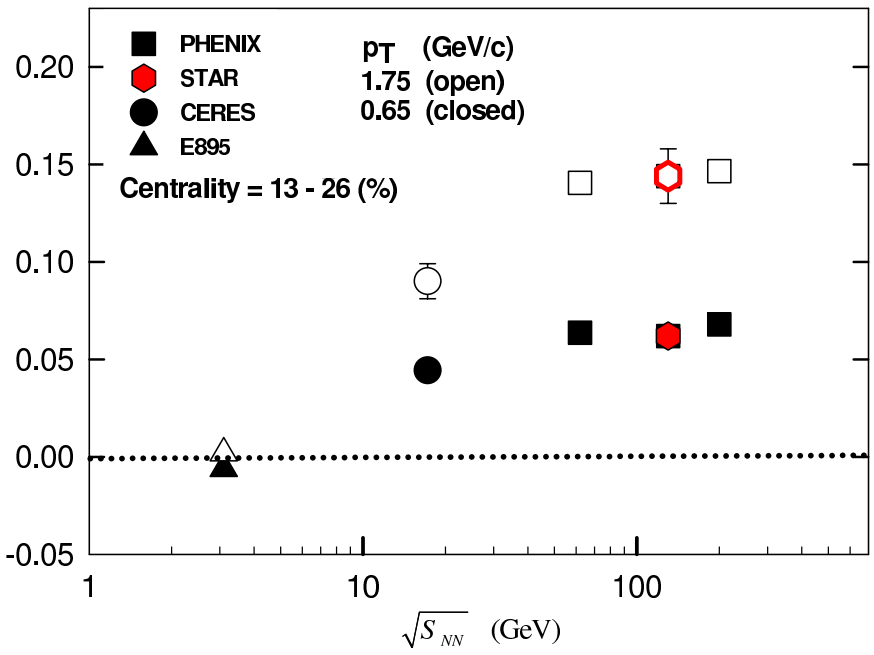

Figure 3.12: Elliptic flow, v_2, from PHENIX appears to have a plateau as a function of energy that begins somewhere in the SPS energy range. This is true for different p_T ranges [56].

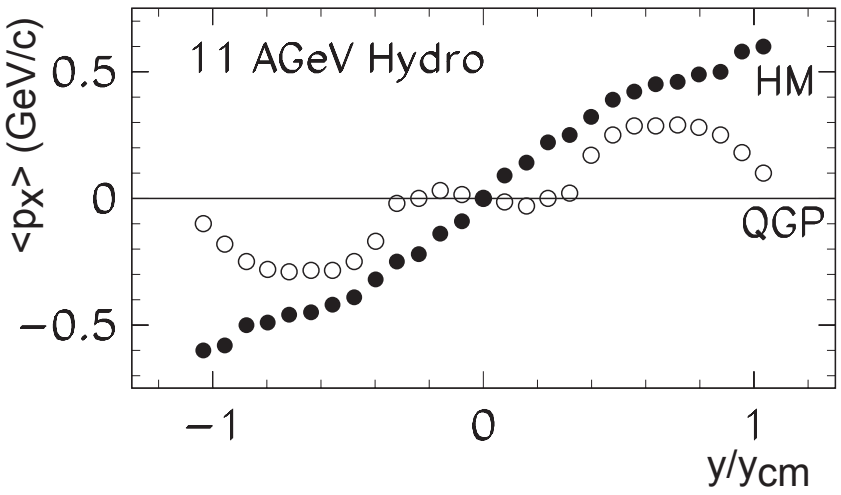

Figure 3.13: The rapidity dependence of v_1 is predicted to have certain features that are related to modifications in the equation of state [7, 57, 58].

might suggest entrance into a mixed phase [7]. Similar to the latent heat discussion in regards to the temperature from kaon spectra, one could imagine that while adding more and more energy to the system the system simply gets more and more partially converted to a deconfined state. Due to the absence of pressure gradients the system is not undergoing accelerated expansion during this stage of evolution leading to the plateau in $v_2(p_T)$. This is the same region where there was speculation (see Section 2.3) that entrance into a mixed phase might allow the freeze-out eccentricity to plateau or rise with energy [8]. If the HBT results were to be confirmed, and these other observations further clarified, a very interesting picture would be emerging.

In the case of v_1, several theoretical predictions suggest a possible "wiggle" structure may appear in the $v_1(y)$, or the rapidity dependence may simply vanish at some

low energy [57–61]. This is shown in Figure 3.13. The relative slopes of $v_1(y)$ for pions and protons at different energies can provide further information. Current Beam Energy Scan results suggest that 10-40% central proton v_1 does change sign above 10 GeV to agree with pion v_1 slope at higher energies, as seen in the upper panel of Figure 3.14 [62]. The estimated slope of v_1, dv_1/dy', was also extracted for only protons that were transported to the mid-rapidity region from the fragmentation regions [62]. In this case, a significant minimum appears which can be seen in the lower panel of Figure 3.14. This may be consistent with a softening of the equation of state, although further work may be needed for verification of this conclusion [62].

3.3 The contribution of this analysis

The observables discussed in the previous section taken together are intended to help map out the QCD phase diagram. They provide complementary information. The sample of observables reviewed not only provides an idea of earlier results that motivated the Beam Energy Scan at RHIC, but also gives a sense of the general approach of the program to answer important questions about the QCD phase diagram, and demonstrates how some of the new results from the Beam Energy Scan are already beginning to improve our understanding of QCD matter.

This thesis fits into the bigger effort to map out the QCD phase diagram by searching for signs that the equation of state at low energy is different from the equation of state at high energy. As described earlier, if the equation of state at low energy develops a flat region indicating a change from a smooth cross-over phase transition to a first order transition, the freeze-out shape could potentially show non-monotonic behavior. Such an observation would also automatically constrain the

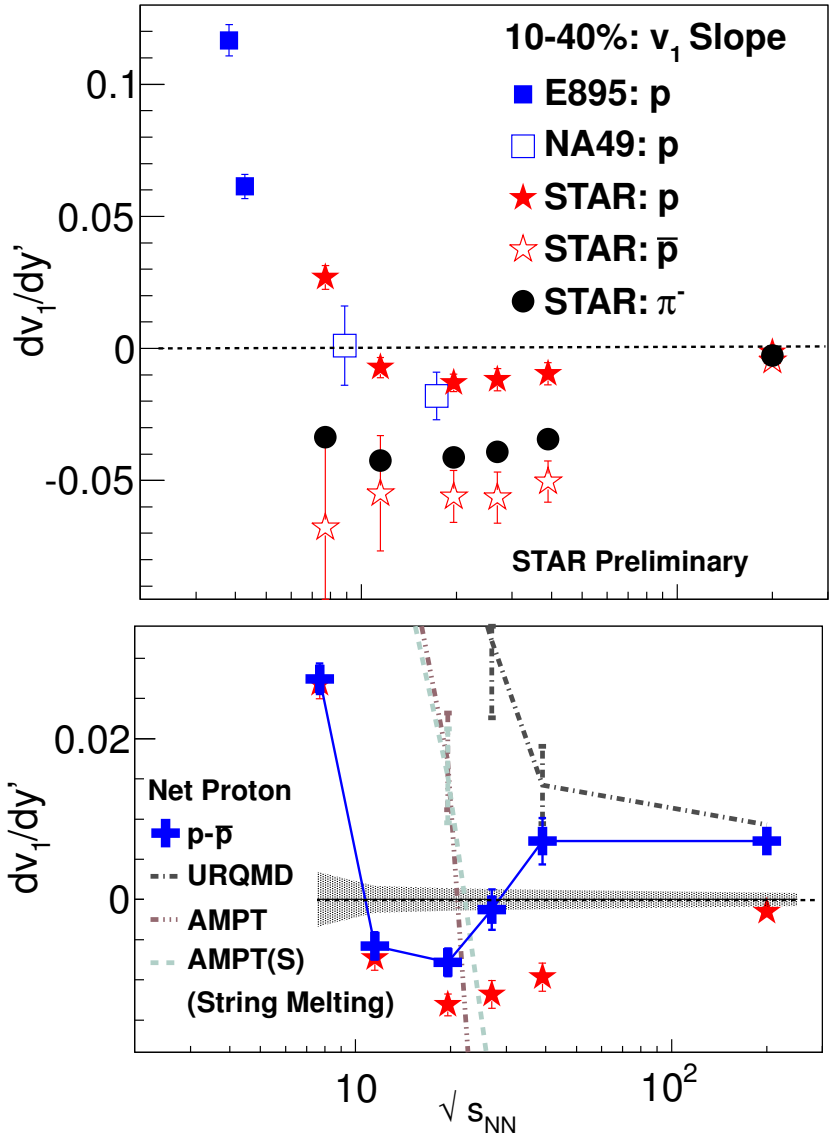

Figure 3.14: The slope of v_1, dv_1/dy', shows non-monotonic behavior [62].

range in beam energy where the QCD critical point could be located. Taken with all the other observables, it is hoped that the new information learned from the Beam Energy Scan as a whole will provide a more clear picture of the properties of QCD matter. In any case, the wealth of new data are already providing new, interesting observations that will provide improved constraints for the models that are used to describe heavy ion collisions.

In the remainder of this thesis the detector, experimental techniques, and theory underlying the extraction of the freeze-out eccentricity are described and the results presented and discussed.

Chapter 4: A detector overview

4.1 The Relativistic Heavy Ion Collider (RHIC)

Data used in this analysis were collected at the Relativistic Heavy Ion Collider (RHIC) at Brookhaven National Lab. The facility, pictured in Figure 4.1, consists of a series of particle accelerators that accelerate heavy ions or protons in stages up to 9.8 GeV before injection into the two RHIC rings. RHIC then accelerates the particles to the desired collision energy. For Au+Au collisions the maximum center of mass energy is $\sqrt{s_{NN}} = 200$ GeV. For p+p collisions even higher energies up to $\sqrt{s_{NN}} = 500$ GeV can be produced and the protons can be polarized allowing the study of physics related to the proton spin.

For the Beam Energy Scan program the collider provided Au+Au collisions at 7.7, 11.5, 19.6, 27, 39, 62.4 and 200 GeV. The collisions at 7.7 GeV actually required the collider to decelerate the Au ions since this is below injection energy. In the near future the Beam Energy Scan program may be extended by colliding beams with fixed targets located near the detectors. The collisions take place at six interaction regions around the RHIC ring where the beams cross. The collisions are measured by two large detectors: Solenoidal Tracker At RHIC (STAR) and the Pioneering High

Figure 4.1: The RHIC accelerator complex at Brookhaven National Laboratory.

Energy Nuclear Interaction eXperiment (PHENIX). The events used in this analysis were measured using the STAR detector.

4.2 The STAR detector

STAR, shown in Figure 4.2, is a wide acceptance detector designed to efficiently measure low momentum hadrons [63]. The Time Projection Chamber (TPC) primarily measures charged hadrons. The calorimeters detect primarily electrons, positrons and photons (many of which are due to the decay of neutral pions). A Time-of-flight (TOF) detector helps extend particle identification to higher momenta. Other detectors including the Beam-Beam Counters (BBCs), Zero Degree Calorimeters (ZDCs),

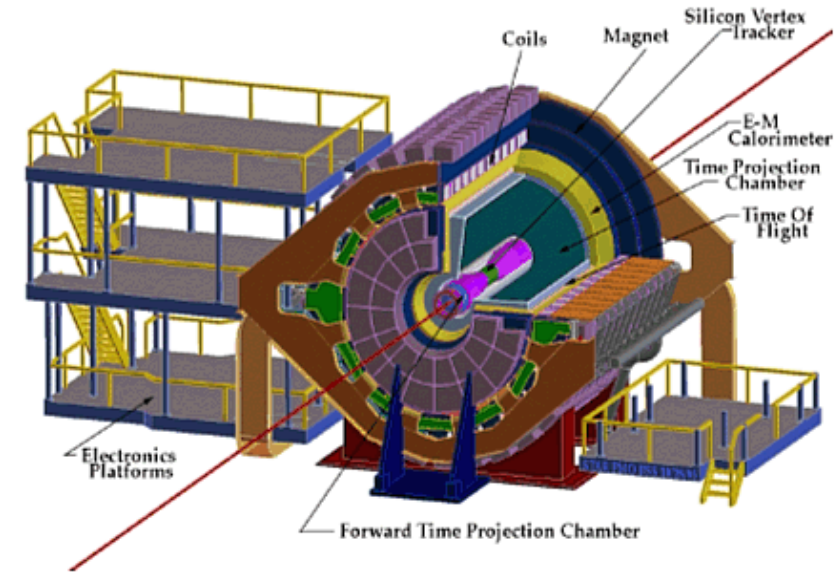

Figure 4.2: The STAR detector and its subsystems.

and Vertex Position Detectors (VPDs) help to trigger on events that occur near the center of the detector.

The main detector for this analysis is the Time Projection Chamber [64, 65] which is a large cylinder (inner radius 0.5 m, outer radius 2 m) with a cathode plane at the center and anode planes at each end to create a uniform electric field. It can measure charged particles with pseudo-rapidity in the range $-1 < \eta < 1$ with 2π azimuthal acceptance. The TPC is filled with P-10 gas (90% Argon, 10% methane) and operates inside a magnetic field (0.5 T for all the energies used in this analysis). Both the magnetic field and the electric field lie parallel to the beam direction. As charged particles fly away from each collision vertex the magnetic field bends the trajectories allowing the charge to be identified. Figure 4.3 shows the charged particle tracks in an event reconstructed by the TPC.

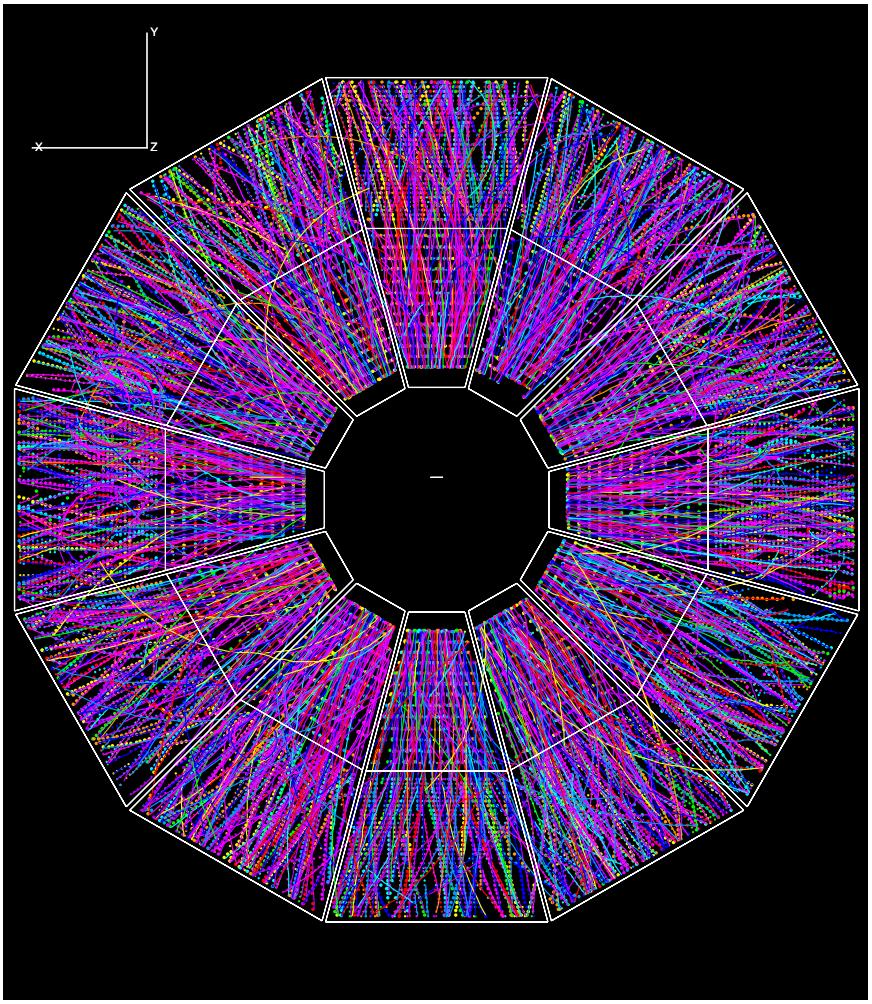

Figure 4.3: Charged tracks reconstructed for an event by the STAR TPC.

The charged particles also interact with the P-10 gas, losing a little energy by ionizing the gas molecules. The energy loss, dE/dx, along a particles path depends on the type of particle and allows for particle identification. The electrons from each track drift in the electric field at 5.5 μm/ns to each end of the TPC. Near the endcaps a set of wires at high potential (the anode plane) creates a strong electric field. When the drift electrons enter this field they are accelerated to high enough energy to ionize additional gas particles which in turn ionize even more particles. The resulting avalanche of electrons is collected by the wires. The positive ions that remain cause an image charge on the final pad plane. This is the electrical signal that is measured. The x and y locations of each point on the track are determined by the x and y locations of the pads that record signals. The z location is determined by combining the time a signal is recieved with the constant drift velocity of the electrons. This allows full three dimensional reconstruction of the tracks.

The size of the electrical signal detected at the endcap is proportional to the number of original electrons liberated by the track which depends on the momentum of the particle and the mass of the particle. From a plot of dE/dx versus momentum such as Figure 4.4 it is possible to separate the low momentum pions from the electrons, kaons and protons. Additional information about the specific particle identification criteria used in this work can be found in Section 7.2.

Detector inefficiencies and measurement uncertainties lead to imperfect reconstruction of individual tracks and pairs of tracks which can have an adverse affect on the HBT measurements. How these inefficiencies arise are described here but the description of how to remove or account for such effects are discussed later in Chapter 7. First, it will be useful to describe how tracks are reconstructed. As described

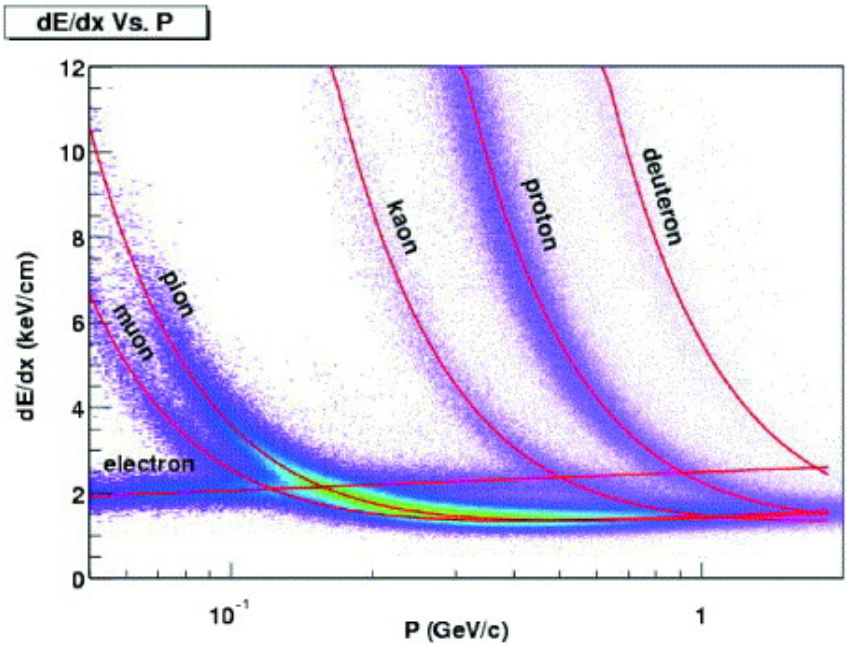

Figure 4.4: Energy loss, dE/dx, as a function of momentum allows particle identification. Figure taken from [64].

above, particles created in the collision ionize gas particles in the TPC volume. The electrons that are liberated in this process drift to the endcaps and eventually a signal is detected on individual pads. The TPC is designed so the signal from a single track is split among roughly three pads which allows estimation of the track position at a scale that is finer than the pad sizes (consider a weighted average of the signal in three adjacent pads or a Gaussian fit to the signal distribution on three pads versus just the pad location with the most signal). The time after the beginning of the event that the signals are detected at the endcap combined with the constant drift velocity (5.5 μm/s) allows identification of the position along beam direction (z-axis) where the particle passed. After being recorded, these hit locations are then fit with a parameterization for a track helix to identify tracks. The tracks are extrapolated back to the beam line. Many of the tracks will extrapolate back to a common location along the beam line within some range of uncertainty. The place were the most tracks converge within some radius (a few centimeters) is identified and the mean x, y, and z coordinates of the distances of closest approach (DCA) of those tracks is identified as the primary vertex position. The tracks used in this calculation are referred to as primary tracks and are the tracks used later in the analysis. The primary tracks are refit requiring the additional point at the primary vertex be included. Other tracks may come from decays of primary particles or may be noise from other interactions between particles and the detector or from pile-up events (extra events that occur in the detector at a similar time which may cause tracks unrelated to the event that was actually triggered).

There is experimental uncertainty in different steps of these calculations. For each hit measured on a TPC pad row there is some uncertainty in the exact position. As

the signals reach the pads on the endcaps they are binned in finite time intervals during which causes some uncertainty in the z-position of each hit as well. When the track helix is fit, which allows determination of the momentum of the track, there is a corresponding uncertainty in the momentum of the track which means there is imperfect momentum resolution. For the HBT analysis which relies on the relative momentum of track pairs this will slightly broaden the relative momentum distributions. For STAR, the effect on HBT results has been studied and estimated to be quite small, 1% to 2.5% for central and peripheral collisions, respectively [66].

An important inefficiency that can have a strong influence on HBT measurements is the ability of the detector to resolve two tracks that are close together. Because of the finite size of the pads that detect signals two tracks that are close together will cause drift electrons that arrive at a similar point on the endcaps. The signal from the two tracks may overlap and at some small separation hits from two tracks can not be resolved. If many hits along two tracks can not be resolved two tracks may be reconstructed as a single track. These tracks are referred to as merged tracks. Alternatively, if a single track produces hits on many pad rows, uncertainties on the location of the hits may allow the track finding algorithm to be tricked such that it reconstructs two tracks when really there is only one. These tracks are referred to as split tracks. These two effects are important to account for because, as described later in Chapter 7, merged tracks will reduce the signal extracted in an HBT analysis while split tracks will add false pairs to the HBT analysis. Methods of dealing with these effects were developed in the past [66, 67], are applied in this analysis, and are discussed later after the HBT analysis has been described.

Chapter 5: HBT interferometry

Hanbury Brown Twiss interferometry is a technique designed to extract spatial and temporal information in particle collisions. The original application was by Hanbury Brown and Twiss to measure the diameters of stars [68]. The technique was developed independently and applied in particle physics by Goldhaber, *et al.*, to study angular distributions of pion pairs in $p\bar{p}$ anhilations [69]. Quantum statistics appeared to cause an enhancement in pairs with small relative momentum [69]. Over time the method has evolved into a precision tool for measuring the space-time properties of the regions of homegeneity at freeze-out in heavy ion collisions [70]. In particular, the size and shape of the homogeneity regions emitting particle pairs can be obtained and information related to the lifetime, and duration of particle emission can be inferred. Dynamics present in the collision and final state interactions can modify the extracted source shapes. If the analysis is performed differentially in bins relative to the reaction plane a connection can be established between the shape of the homegeneity region and the shape of the entire fireball at kinetic freeze-out [8]. This chapter elaborates on some of the theory underlying the analysis performed in this thesis. The experimental details of the analysis are left for Chapter 6.

5.1 Theory of HBT

HBT exploits a quantum statistical effect which determines the distribution of the relative momentum of correlated particles generated during the collision of two heavy nuclei. Figure 5.1 shows how HBT exploits a connection between the measured particle momenta and the femtoscopic source sizes . The correlation function is defined by the Koonin-Pratt equation [71, 72]

$$C(\vec{q},\vec{k}) = \int d^4 r S(\vec{q}, r, \vec{k}) |\psi_2(\vec{r},\vec{q})|^2 \tag{5.1}$$

where $S(\vec{r})$ is the distribution of separation distance between pairs of particles, $\vec{r} = \vec{r}_i - \vec{r}_j$. The squared, two particle wave-function $|\psi_2(\vec{r},\vec{q})|^2$, is the probability density for observing a particle pair emitted with a given separation distance in the source and a given relative momentum $\vec{q} = \vec{p}_i - \vec{p}_j$. The correlation function and source function are functions of the total pair momentum, $\vec{k}$. For bosons (fermions), interference of the single particle wavefunctions lead to the two particle wave-function

$$\psi_2(\vec{r},\vec{q}) \approx \psi(\vec{r}_1,\vec{p}_1)\psi(\vec{r}_2,\vec{p}_2) \pm \psi(\vec{r}_1,\vec{p}_2)\psi(\vec{r}_2,\vec{p}_1) \tag{5.2}$$

where the sign is determined by the type of quantum statistics (Bose-Einstein or Fermi-Dirac) that is appropriate for the particles being studied. The current analysis is performed on identical pions (bosons) so the + sign is appropriate.

The correlation function may be viewed in terms of probabilities. The probability of observing a single particle with momentum p_i is

$$P(p_i) = \int d^4 x S(x_i, p_i) \tag{5.3}$$

and the probability of observing a pair of particles with momenta p_i and p_j is

$$P(p_i, p_j) = \int d^4 x_i d^4 x_j S(x_i, p_i) S(x_j, p_j) |\psi_2(\vec{r},\vec{q})|^2. \tag{5.4}$$

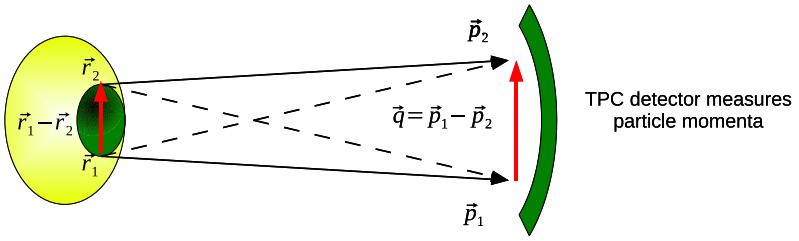

Figure 5.1: HBT diagram connecting particle momenta to source shape.

Here the functions $S(x_i, p_i)$ are the single particle probability densities for emission of a single particle with momentum, p_i, from emission point, x_i, in the source. The derivation in the next section connects these single particle probability densities to the distribution of separation distance for particle pairs, $S(\vec{q}, \vec{r}, \vec{k})$, in Eq. 5.1 using some reasonable approximations. In the two particle case, Eq. 5.4, the product of two single particle probability distributions are weighted by the two-particle wave-function which modifies the probability appropriately for quantum statistics. In both cases, because the particles are observable, they are real and must be on-shell which requires $E_p^2 = p^2 + m^2$ and therefore $p^0 = E_p$ constrains the four-momenta. In terms of these probabilities the correlation function can be expressed as

$$C(\vec{q}) = \frac{P(\vec{p}_1, \vec{p}_2)}{P(\vec{p}_1)P(\vec{p}_2)}. \tag{5.5}$$

If particles are emitted independently from one another then $P(p_i, p_j) = P(p_i)P(p_j)$ and the correlation function would be unity. This would be the case if quantum statistics were not important. It would also be true if the pairs were formed with

particles from different, mixed events which will be exploited later in the construction of the denominator in the experimental correlation function. If emission of the particles in the pair obeys Bose-Einstein statistics then there will be an enhancement at low relative momentum, $\vec{q}$, in the probability of observing particles with p_i and p_j and therefore an enhancement in $C(\vec{q})$ for small values of $\vec{q}$. If the particles being studied obey Fermi-Dirac statistics the correlation function will instead exhibit a deficiency in pairs at low $\vec{q}$. In addition to quantum statistics, final state interactions and collective dynamics can modify the particle momenta (and relative momenta) which modifies $P(p_i, p_j)$ and therefore the correlation function signal. These will be discussed later. While this discussion has explained qualitatively how a correlation analysis can be used to extract femtoscopic length scales from the observed final state particle momenta, an example derivation (there are many variations in the literature) can provide a more in depth understanding of the source/wavefunction description of the correlation function and will allow to discuss some approximations that enter the derivation.

5.2 Deriving the correlation function

The probability of observing a single particle with momentum p_i emitted from a point x_i was given by Equ. 5.3. The probability of observing two particles with momenta p_i and p_j emitted from the points x_i and x_j in the source was given by Equ. 5.4. These already connect the source distributions to the probabilities. However, to get to the final form of the correlation function requires some approximations in order to convert the distributions of sources that emit single particles, $S(x_i, p_i)$, to the pair separation distibribution, $S(r)$, in Eq. 5.1. The first step in the derivation

is to express the two particle wave function. For the moment, contributions from the Coulomb interaction and strong interactions are excluded from the two particle wave function. Because the particles measured are free streaming through the detector, they can be represented as plane waves

$$\psi(x_i, x_i', p_i) \approx e^{i(x_i'-x_i)p_i} \tag{5.6}$$

where the primed variable is the location where the particle is observed and the unprimed variables are the values at the source when the particle is emitted. Substituting in Eq. 5.2 the two particle wave function becomes

$$\psi(x_i, x_j, p_i, p_j) = \frac{1}{\sqrt{2}}(e^{i(x_i-x_i')p_i}e^{i(x_j-x_j')p_j} \pm e^{i(x_i-x_j')p_j}e^{i(x_j-x_i')p_i}). \tag{5.7}$$

Squaring this, the primed variables cancel leaving

$$|\psi(x_i, x_j, p_i, p_j)|^2 = 1 \pm \cos((x_i - x_j)(p_i - p_j)). \tag{5.8}$$

Substituting into Eq. 5.4, and identifying $\vec{q} = \vec{p}_i - \vec{p}_j$ and $\vec{r} = \vec{x}_i - \vec{x}_j$, yields

$$P(p_i, p_j) = \int d^4x_i S(x_i, p_i) \int d^4x_j S(x_j, p_j) \pm \int d^4x_i d^4x_j S(x_i, p_i) S(x_j, p_j) \cos(qr) \tag{5.9}$$

The first two terms are just the single particle probabilities, Eq. 5.3, and the second term arises from the quantum interference. Substituting Eqs. 5.3 and 5.9 into Eq. 5.5, the correlation function becomes

$$C(\vec{q}, \vec{k}) = 1 \pm \frac{\int d^4x_i d^4x_j S(x_i, p_i) S(x_j, p_j) \cos(qr)}{\int d^4x_i S(x_i, p_i) \int d^4x_j S(x_j, p_j)}. \tag{5.10}$$

The goal is to express the correlation function in terms of only the relative momentum, $\vec{q}$, which can be measured, and the source distributions only in terms of the separation of the particles in the source, $\vec{r}$, which is the information to be extracted

from the correlation function. The source distributions are themselves functions of both single particle momenta and position of the single particle emission source so an approximation is needed, the smoothness approximation. Using the relative and average pair momenta, $\vec{q}$ and $\vec{k}$, the source functions can be written as [73]

$$S(x_i, p_i)S(x_j, p_j) = S(x_i, k + \frac{q}{2})S(x_j, k - \frac{q}{2}) \approx S(x_i, k)S(x_j, k). \tag{5.11}$$

The approximation is valid for small $\vec{q}$ and assumes that the source functions have a smooth dependence on the particle momenta [73, 74]. These seem reasonable. For instance, the signal in the two-pion correlation function appears at small $\vec{q}$ and pairs with small average pair momenta are excluded from the analysis. Typically, a smooth Gaussian shape is assumed in order to extract the main length scales that describe the two particle emission sources. The approximation is valid in both the numerator and denominator of Eq. 5.9. Using the approximation yields

$$C(\vec{q}, \vec{k}) = 1 \pm \frac{\int d^4x_i d^4x_j S(x_i, k)S(x_j, k)\cos(qr)}{\int d^4x_i S(x_i, k) \int d^4x_j S(x_j, k)}. \tag{5.12}$$

The last step is to convert from specific positions of sources, x_i and x_j, to a relative separation, $r = x_i - x_j$. Similar to the momentum conversion, the quantity $X = (x_i + x_j)/2$ can be defined so $x_i = X + r/2$ and $x_j = X - r/2$. Assuming X is the space-time position of the center of the source emitting the pair, r/2 may be interpreted as a measure of the width of the source centered at X. In this pair center-of-momentum coordinate system, Reference [73] defines what the authors refer to as the normalized relative distance distribution

$$d(r, k) = \int d^4X \frac{S(X + \frac{r}{2}, k)}{\int d^4r S(r, k)} \frac{S(X - \frac{r}{2}, k)}{\int d^4r S(X - \frac{r}{2}, k)}. \tag{5.13}$$

Under the assumption of the smoothness approximation and conversion to pair center-of-momentum coordinates, Eq. 5.13 relates the single particle emission functions

$S(x_i, p_i)$ to the two-particle relative separation distribution. In other words, $d(r,k)$, is essentially $S(r)$ in Eq. 5.1. Substituting into Eq. 5.12 yields

$$C(\vec{q},\vec{k}) = 1 \pm \int d^4r \cos(qr) d(r,k). \tag{5.14}$$

where the integration has been converted from $d^4x_i d^4x_j$ to $d^4r d^4X$. They further simplify this by an assuming on-shell pair momenta $qk = q^0k^0 - \vec{q}\cdot\vec{k} = 0$ is approximately true. Then using the pair velocity, $\vec{\beta} = \vec{k}/k^0$, yields $q^0 = \vec{\beta}\cdot\vec{q}$. Noting that $qr = \vec{q}\cdot\vec{r} - \vec{q}\cdot\vec{\beta}t$ allows the integal to be written as

$$C(\vec{q},\vec{k}) = 1 \pm \int \cos(\vec{q}\cdot\vec{r}) \int dt d(\vec{r} + \vec{\beta}t, t; k). \tag{5.15}$$

By defining the relative source distribution [73]

$$S(\vec{r},\vec{k}) = \int dt d(\vec{r} + \vec{\beta}t, t; \vec{k}) \tag{5.16}$$

it is apparent that the quantity the correlation function measures is the shape of the source separation distribution averaged over time. Finally, the correlation function can be written as

$$C(\vec{q},\vec{k}) = 1 \pm \int d^3r S(\vec{r},\vec{k}) \cos(\vec{q}\cdot\vec{r}) \tag{5.17}$$

Comparing to Eq. 5.1, in this derivation the integral has been reduced from four dimensions to three dimensions. Information related to how the emission source evolves with time is lost due to the integration over time in Eq. 5.16. While no information about how the emission source function evolves during an individual collision can be obtained in this formalism, dynamics at work in the collision can leave patterns in the dependence of the correlation function on the average transverse pair momentum, $\vec{k_T}$. The size and shape of the two-particle relative separation function can be extracted from correlation functions constructed for different values of $\vec{k_T}$ and

the dependencies on $\vec{k_T}$ can be related to physical quantities such as the lifetime of the collision evolution or the duration of particle emission. So information about how the fireball produced in the collision evolves can be inferred from HBT analyses. The derivation reviewed here does demonstrate that a connection can be established between the measured particle momenta and the relative separation of particles in the source.

5.3 Final state interactions

The derivation in the last section assumed final state interactions were not present and only quantum statistics played a role in the correlation between particles. In different circumstances effects due to strong force interactions, Coulomb force interactions, or a mean field due to the rest of the participant zone might also contribute significantly to the two-particle correlation function. For femtoscopy with charged pions, the strong force is negligible. The reason is the typical separation for pions in the source is several femtometers (as will be measured later) while the typical range for strong interactions between pions is 0.2 fm [75]. Studies accounting for the strong force demonstrate that the effect is very small in pion interferometry. In fact, for like-sign pion analysis it is negligible [66].

Mean field effects due to net charge in the collision fireball could potentially be significant. For the high energies studied in this analysis such an effect has also been found to be negligible [76, 77]. At high energy the much of net charge is conserved in the fragmentation region. Constrast this with the situation at very low energies where more of the net charge remains in the fireball at mid-rapidity and the colliding nuclei evaporate into smaller, often multiply charged, nuclei, therefore allowing a relatively

large mean field effect on the outgoing particles. Anyway, it was pointed out in [67] that such an effect would apply similarly to both particles in each pair so the relative momentum for each pair would be rather unchanged.

The Coulomb interaction between pions in each pair turns out to be significant in charged pion correlations. In the derivation in the previous section, the two particle wave function was constructed out of plane waves representing the observed particles but subject to Bose-Einstein statistics. The source distribution, $S(\vec{r})$, describes distribution of the relative separation of particles in each pair when they are emitted. Even considering a Coulomb interaction, when observed far from the source, the particles are still described approximately by plane waves but the source distribution itself appears distorted by the Coulomb interaction. More specifically, the wave function is really a Coulomb wave that approximates a plane wave asymptotically [78]. For like-sign particles forming a pair, the repulsive Coulomb force will tend to increase both the observed separation distance, $\vec{r}$, and the relative momentum, $\vec{q}$. From Eq. 5.17, it is clear that if the relative separation distribution changes the correlation function will change too. From the increase in the relative momentum, $\vec{q}$, it means that for identical bosons, the enhancement at very low $\vec{q}$ will be reduced by the Coulomb interaction.

In theory, one can introduce a correction to the source distribution by multiplying by a correction factor, $K_{\mathrm{Coul}}(q_{\mathrm{inv}})$. Then the correlation function, Eq. 5.17, can be written as [78]

$$C(\vec{q},\vec{k}) = K_{\mathrm{Coul}}(q_{\mathrm{inv}})(1 \pm \int d^3r S(\vec{r},\vec{k}) \cos(\vec{q}\cdot\vec{r})) \tag{5.18}$$

The value of $K_{\rm Coul}(q_{\rm inv})$ in each $\vec{q}$ bin of the correlation function can be calculated for each $\vec{q}$ bin due to the relation from [79]

$$K_{\rm Coul}(\vec{q}) \equiv \int d^3r S(r)|\psi_{\rm Coul}(q,r)|^2. \tag{5.19}$$

This quantity is computed numerically using mixed event pairs. A mixed event distribution in $\vec{q}$-space is created with the entry for each pair weighted by $q_{\rm inv}$. Later this Coulomb weighted mixed event distribution can be divided by the unweighted mixed event distribution and the result is the change in the correlation function appropriate for each bin in $\vec{q}$-space. There are no Bose-Einstein effects in this quantity due to using mixed events, and acceptance and efficiency effects cancel as the same pairs enter both distributions. This Coulomb effect in each $\vec{q}$ bin is simply included as a constant in a later step when the correlation function is fit to extract the HBT radii that describe the source region. This experimental technique for accounting for the Coulomb effect, called the Bowler-Sinyukov method, is described further in the next Chapter.

5.4 Space-momentum correlations

The discussion in the last two sections has assumed a static source. In other words the collective flow of particles discussed earlier has not yet been taken into account. In a static source the size and shape of the region emitting particles may correspond to the entire fireball at kinetic freeze-out. The presence of collective behavior, however, will result in particles emitted from one region to have a preferential direction compared to particles emitted from a different region. The source sizes probed by

the correlation function correspond to a region that is smaller than the fireball produced in the collision. Figure 5.2 illustrates this behavior. The contours correspond to emission regions, often called regions of homogeneity. Radial flow boosts particles near the top of the participant zone preferentially out of plane. Particles emitted in the reaction plane are emitted preferentially in the reaction plane direction. In other words, collective flow introduces a correlation between the position where a particle is emitted and its momentum, a space-momentum correlation. Particle pairs that are more effected by the collective flow, those boosted to higher k_T, experience stronger space-momentum correlation and therefore correspond to smaller emission regions. The extracted HBT radii show a systematic decrease at higher k_T as will be observed later in the results in Figure 8.13. The effect of space-momentum correlations is included in Eqs. 5.17 and 5.19 by including the $\vec{k}$ dependence in $C(\vec{q},\vec{k})$ and $S(\vec{r},\vec{k})$.

All the discussion of the correlation function in the previous sections is still applicable. The presence of space-momentum correlations just means that the extracted source sizes measure, not the entire participant zone, but rather only a smaller region of the total volume. In the next few sections, a connection will be made between variations in the shape of these smaller regions of homogeneity and the shape of the entire participant zone at freeze-out. Such a connection is essential to the azimuthally-differential analysis.

5.5 Gaussian parameterization

To extract the shape and size of the emission function requires some assumption about the shape. Usually it is assumed that the source function is a three-dimensional Gaussian which permits extraction of the widths of the distribution. The widths

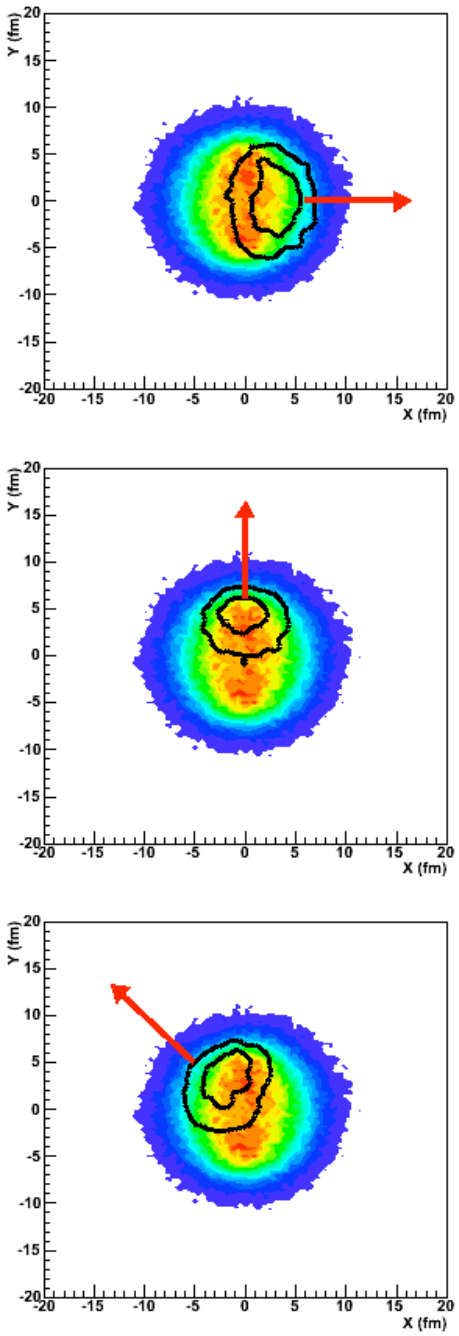

Figure 5.2: Correspondence between regions of homogeneity and entire participant zone in non-central collisions. The presence of anisotropic pressure gradients introduces space-momentum correlations. This figure is reproduced from Reference [80].

are the HBT radii. While the shape is known to have some non-Gaussianess this assumption allows estimation of the main length scales of the source. To get a sense of what these radii describe, consider the first few terms in the Taylor expansion of $\cos(\vec{q}\cdot\vec{r})$ in Eq. 5.17

$$C(\vec{q},\vec{k}) \approx 1 \pm \int d^3r S(\vec{r},\vec{k})\{1-\alpha(r_i r_j)+...\} \tag{5.20}$$

Notice that integration of $r_i r_j$ over the probability density $S(\vec{r})$ define a variance

$$\sigma_{ij}^2 = \langle r_i r_j \rangle = \int d^3r S(\vec{r},\vec{k}) r_i r_j. \tag{5.21}$$

The separation distance obtained in this formulation may be interpreted as the root-mean-square widths of the region of homogeneity, $S(\vec{r})$. Assuming $S(\vec{r})$ is a Gaussian, as in [73], allows writing the expression

$$S(\vec{r}) \approx S(X)S(\vec{r}) \approx S(X)e^{-q_i q_j \langle r_i r_j \rangle}. \tag{5.22}$$

Then the correlation function will also have a Gaussian form as in

$$C(\vec{q},\vec{k}) = 1 \pm e^{-\vec{q}^{\dagger}\bar{R}^2\vec{q}} = 1 \pm e^{-R_{ij}^2 q_i q_j} \tag{5.23}$$

By measuring the relative momentum distribution and fitting with a Gaussian of this form, using R_{ij}^2 as the fit parameters allows to extract the root-mean-square size of the regions of homogeneity. Once again, these radii describe smaller regions of homogeneity, not the entire participant zone. To make a connection between the regions of homogeneity and the shape of the entire participant zone, it will be convenient at this point to choose a specific coordinate system in which to express the momenta and radii.

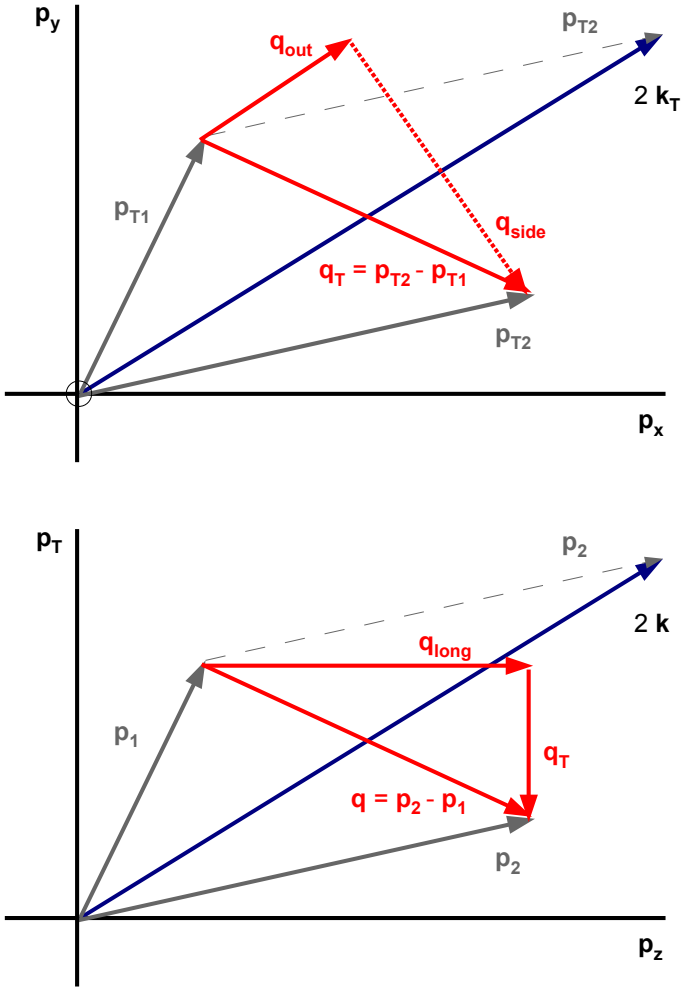

Figure 5.3: The Bertsch-Pratt, out-side-long (o-s-l) coordinate system. The upper part of the figure demonstrates how the transverse components of the momentum difference, $q_{\rm out}$ and $q_{\rm side}$ are defined relative to the average pair transverse momentum, k_T. The lower part of the figure demonstrates how the longitudinal component, $q_{\rm long}$, is defined parallel to the beam direction.

5.6 Bertsch-Pratt coordinate system

The relative pair momentum, $\vec{q}$, is often projected into the Bertsch-Pratt [81–83] coordinate system pictured in Figure 5.3. The three axes are labeled out, side, and long (or o, s, and l) and are oriented such that q_{out} lies along the direction of the average transverse pair momentum, $\vec{k_T}$, while q_{long} lies along the "longitudinal" beam direction, and q_{side} is perpendicular to the other directions and is therefore also in the transverse plane. Further information related to these coordinates can be found in Section 6.2 which is relavent to the experimental details of the analysis. The relative momentum is expressed in the longitudinal co-moving system (LCMS) in which the longitudinal component of the pair velocity vanishes. To extract the bulk shape of the particle emitting regions, a Gaussian parameterization is typically used:

$$C(\vec{q}) = 1 + (e^{-q_o^2 R_o^2 - q_s^2 R_s^2 - q_l^2 R_l^2 - 2q_o q_s R_{os}^2 - 2q_o q_l R_{ol}^2 - 2q_s q_l R_{sl}^2}) \tag{5.24}$$

Fitting the measured correlation function with Eq. 5.24 permits extraction of the HBT radii. The diagonal radii, R_o^2, R_s^2, and R_l^2 are the widths of the emission regions. The cross terms become non-zero if a correlation appears between different relative momentum components which appears as a tilt in the $\vec{q}$-space distribution. In Figure 5.4, these cross terms are predicted to exhibit oscillations relative to the first order event plane - tilting first one way and then the other. In the next chapter similar, experimental projections relative to the second order event plane are measured. In that case the first order oscillations of R_{sl}^2 and R_{ol}^2 average to zero but the R_{os}^2 cross terms still exhibits a clear second order oscillation. More elaboration on this can be found in Section 6.2. The diagonal terms, R_{out}^2, R_{side}^2, and R_{long}^2 are also

predicted to show second order oscillations relative to the event plane. Measurement of these oscillations will allow extraction of the shape of the entire participant zone.

In the azimuthally differential analysis several correlation functions are constructed for different angular bins. These can each be fit with a Gaussian parameterization related to Eq. 5.24 to extract the HBT radii parameters as described in more detail in Section 6.2. Alternatively, a global fit method, described in Section 6.7 can simultaneously fit the distributions for all angular bins to directly extract the participant zone shape. These experimental details are explored in the next chapter. The theoretical connection between the shape of the emission regions and the entire participant zone is explored in the next section.

5.7 Extracting the shape of the participant zone

As mentioned before space-momentum correlations reduce the correspondence between the shape of the emission regions and the entire particpant zone. In non-central collisions, elliptic flow affects particles emitted in the reaction plane differently than particles emitted out of the reaction plane. The shapes of the emission regions measured in bins relative to the event plane exhibit sinusoidal variations. In particular the HBT radii oscillate. The more elliptical the freeze-out shape, the larger the amplitude of the oscillation. The shape of the fireball at kinetic freeze-out can be described by widths in space-time (σ_x, σ_y, σ_z, σ_t) as pictured in Figure 5.5. From Reference [80], the connection between the HBT radii and the shape of the participant zone may be expressed by the following equations:

$$R_o^2(\phi) = \frac{1}{2}(\sigma_x^2 + \sigma_y^2) + \frac{1}{2}(\sigma_y^2 - \sigma_x^2)\cos(2\phi) + \beta_T^2\sigma_t^2, \tag{5.25}$$

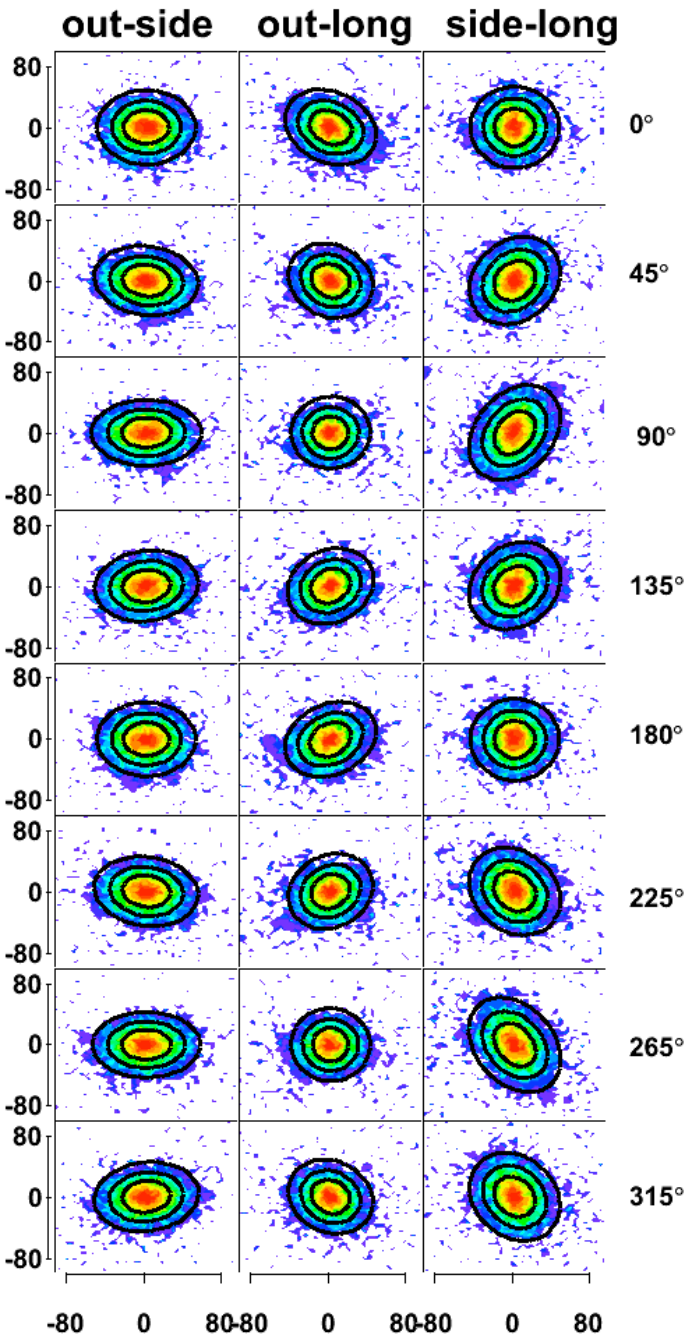

Figure 5.4: Two dimensional projections of a correlation function in the q_o-q_s, q_s-q_l and q_o-q_l planes for like-sign pions at mid-rapidity. All scales are in GeV/c. This figure is taken from Ref. [80].

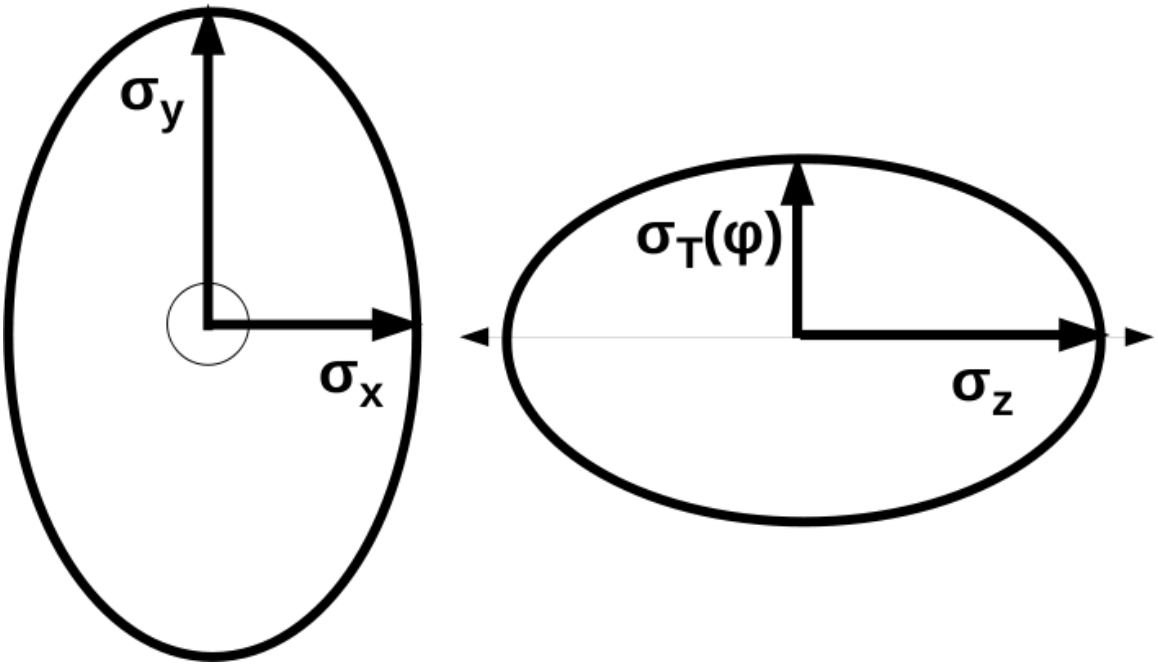

Figure 5.5: Depiction of the widths in three dimensions of the widths of the source region at kinetiv freeze-out in a non-central heavy ion collision. On the left are the widths in the transverse plane, in the reaction plane, σ_x, and normal to the reaction plane, σ_y. The width of the source in the longitudinal direction, σ_z are shown on the right where $\sigma_T(\phi) = \sqrt{\sigma_x^2 + \sigma_y^2}$ varies with azimuthal angle, ϕ. In reality these are modified by the presence of the temporal width, σ_t, appropriate for four-dimensional space-time description of the source. This leads to dependence of the HBT radii that describe the same source region on the space-momentum correlations induced by flow effects.

$$R_s^2(\phi) = \frac{1}{2}(\sigma_x^2 + \sigma_y^2) + \frac{1}{2}(\sigma_y^2 - \sigma_x^2)\cos(2\phi) \tag{5.26}$$

$$R_l^2(\phi) = \sigma_z^2 + \beta_l^2\sigma_t^2 \tag{5.27}$$

$$R_{os}^2(\phi) = -\frac{1}{2}(\sigma_y^2 - \sigma_x^2)\sin(2\phi) \tag{5.28}$$

$$R_{ol}^2 = \beta_l\beta_T\sigma_t^2 \tag{5.29}$$

$$R_{sl}^2 = 0. \tag{5.30}$$

The equations in Reference [80] allow first order oscillations. In this thesis only the second order event plane is determined so the first order oscillations of the cross terms R_{ol}^2 and R_{sl}^2 average to zero at mid-rapidity and are omitted in the equations listed above. However, away from mid-rapidity the R_{ol}^2 term becomes non-zero. Another note, is that the dependence in Eq. 5.29 for R_{ol}^2 on the pair velocities and σ_t^2 is valid for a static model only [83, 84]. Other assumptions, of transverse or longitudinal flow for instance, result in more complex dependence of R_{ol}^2 on different quantities [83, 84]. The equations above are strictly valid only when there is no flow [80]. The validity of these expressions in the presence of flow will be discussed in Section 7.4.

The R_s^2 term contains no term with σ_t^2, β_T, or β_l and therefore contains primarily spatial information. The other radii, R_o^2, R_l^2, R_{os}^2 and R_{ol}^2 mix spatial and temporal information and therefore may be affected by dynamical influence of radial or elliptical flow. Since R_s^2 oscillates relative to the event plane, the larger the difference between

regions of homogeneity in the in-plane and out-of-plane directions the larger the size of the oscillation. This will be exploited to extract the freeze-out shape as described in the next chapter.

Chapter 6: Experimental HBT analysis

In this chapter, an overview of the experimental HBT analysis is provided including the extension to an azimuthally differential analysis and extraction of the freeze-out eccentricity. The material in this section is adapted from Section IV and V of [85], the paper corresponding to the material in this thesis.

6.1 The correlation function

The experimental correlation function is constructed by forming the distributions of relative momenta, $\vec{q} = (\vec{p}_i - \vec{p}_j)$. A numerator, $N(\vec{q})$ uses particles from the same event, while a mixed event denominator, $D(\vec{q})$, uses particles from different events. The numerator distribution is driven by two-particle phasespace, quantum statistics, and Coulomb interactions, while the denominator reflects only phasespace effects. Since quantum statistics and final state interactions are driven by freeze-out geometry [70], the ratio $N(\vec{q})/D(\vec{q})$ carries geometrical information. This ratio defines the correlation function. The denominators were constructed with pairs formed from mixed events where the mixed events were required to have similar centrality, z vertex location, and event plane angle as described earlier. In the azimuthally differential analysis, four correlation functions were formed corresponding to four 45° wide angular bins relative to the event plane centered at 0° (in-plane), 45°, 90° (out-of-plane),

and 135°. The angle between the transverse momentum for each pair and the event plane is used to assign each pair to one of the correlation functions. Detector inefficiency and acceptance effects apply to both the numerator and denominator so, in taking the ratio to form the correlation function, these effects largely cancel.

6.2 Bertsch-Pratt parameterization

The relative pair momentum, $\vec{q}$, is projected onto the Bertsch-Pratt [81–83], outside-long (or o-s-l), coordinate system outlined in Chapter 5. The relative momentum is expressed in the longitudinal co-moving system (LCMS) in which the longitudinal component of the pair velocity vanishes.

To extract the bulk shape of the particle emitting regions, a Gaussian parameterization is typically used:

$$C\left(\vec{q}\right) = (1-\lambda) + K_{\mathrm{Coul}}(q_{\mathrm{inv}})\lambda\left(1 + e^{-q_o^2R_o^2 - q_s^2R_s^2 - q_l^2R_l^2 - 2q_oq_sR_{os}^2 - 2q_oq_lR_{ol}^2}\right) \tag{6.1}$$

The λ parameter accounts for non-primary particles that may come from resonance decays and misidentified particles [86]. Particles that exhibit Bose-Einstein correlations will be emitted with similar positions and therefore can experience Coulomb interactions as well. The other particles represented by the $(1-\lambda)$ term are emitted from larger seperations and will not experience either type of correlation. The values of K_{Coul} account for the Coulomb interaction as discussed in the next section. Theoretical considerations related to K_{Coul} were reviewed in the last chapter as well.

The R_{ol}^2 term vanishes at mid-rapidity, but becomes positive (negative) at forward (backward) rapidity in both azimuthal and non-azimuthal analyses [83]. For the azimuthally integrated analysis R_{os}^2 vanishes, while in an azimuthally differential

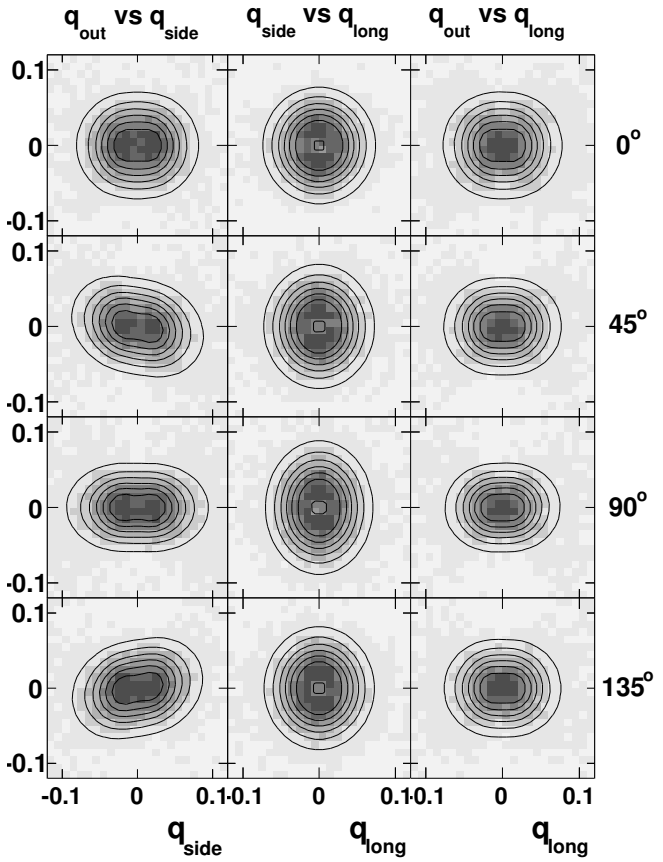

Figure 6.1: Two dimensional projections of a correlation function in the q_o-q_s, q_s-q_l and q_o-q_l planes for like-sign pions at mid-rapidity in 20-30% central, 27 GeV collisions with $0.15 < k_T < 0.6$ GeV/c. All scales are in GeV/c. In each case the third component is projected over $\pm$ 0.03 GeV/c. The emission angles relative to the event plane are within $\pm 22.5°$ of the bin centers indicated along the left side. The tilt in the q_o-q_s plane is clearly visible. Contour lines represent projections of the corresponding fit.

analysis a second order sinusoidal variation appears relative to the reaction plane. Parametrically, a non-zero cross term corresponds to a tilt of the correlation function in $\vec{q}$-space. This can be seen clearly in Fig. 6.1 in the $q_{\rm out}$-$q_{\rm side}$ plane. At 45° there is a tilt resulting in a positive R^2_{os} cross term. At 135° there is an opposite tilt corresponding to a negative R^2_{os} crossterm. It may be informative to compare and contrast results in Figure 6.1 with the predicted oscillations relative to the first order event plane in Figure 5.4. The R^2_{ol} and R^2_{sl} tilts average to zero in Figure 5.1 because they come from a 2^{nd}-order analysis at mid-rapidity. Away from mid-rapidity the R^2_{ol} cross term becomes non-zero and is included as a parameter in Eq. 6.1. The R^2_{sl} term remains zero by symmetry and is therefore excluded as a fit parameter. The interplay between the cross terms and the inherent non-Gaussianess of the correlation function is discussed later, where folding the relative momentum distributions allows covariations in the fit parameters that would strongly effect the results. In this analysis, no folding of $\vec{q}$-space is performed, eliminating this effect.

In the azimuthally differential analysis, several correlation functions are constructed for different angular bins. These are each fit with Eq. 6.1 to extract the fit parameters. The relationship between these fit parameters describing the regions of homogeneity and the shape of the source region (the collision fireball at kinetic freeze-out) has been described in the last chapter and in several references, such as [80, 87, 88], for boost invariant systems.

6.3 Coulomb interaction

Particles that are nearby in phase space and carry the signal in the correlation function will also experience Coulomb interactions. The quantum interference signal,

due to Bose-Einstein statistics for charged pions, allows extraction of the shape of the emission region from the relative momenta of pion pairs [70]. However, the correlation function also contains a signal due to final-state Coulomb interactions. The effect of the Coulomb interaction must be taken into account in order to correctly extract the HBT radii. Different methods of accounting for the Coulomb interaction were studied systematically in [86]. The most appropriate method, the Bowler-Sinyukov method [89, 90], is used in this analysis. The Coulomb interaction is computed for each pair with relative momentum components, (q_o, q_s, q_l), that enters the analysis. The average interaction in each (q_o, q_s, q_l) bin is included as a constant, $K_{\rm Coul}$, in the fit parameterization. As described in the last chapter, $K_{\rm Coul}$ is the squared Coulomb wave function integrated over the entire spherical Gaussian source. The same radius, 5 fm, is used as in earlier analyses. In Eq. 6.1, $K_{\rm Coul}$ only applies to the pairs nearby in phase space (the exponential term) and not to other particles accounted for by the $(1 - \lambda)$ term.

As discussed in the previous chapter, correction is not made for the Coulomb interaction between each particle and the mean field due to the net charge of the bulk system formed in the collision. At the energies studied here, this interaction has been found to be negligible [76, 77].

6.4 Event plane calculations

The azimuthal analysis requires determining the event plane for each event, including applying appropriate methods to flatten the event plane distribution [11]. Uncertainty in the event plane reduces the extracted oscillation amplitudes of the HBT radii. The event plane resolutions must be computed in order to correct for this

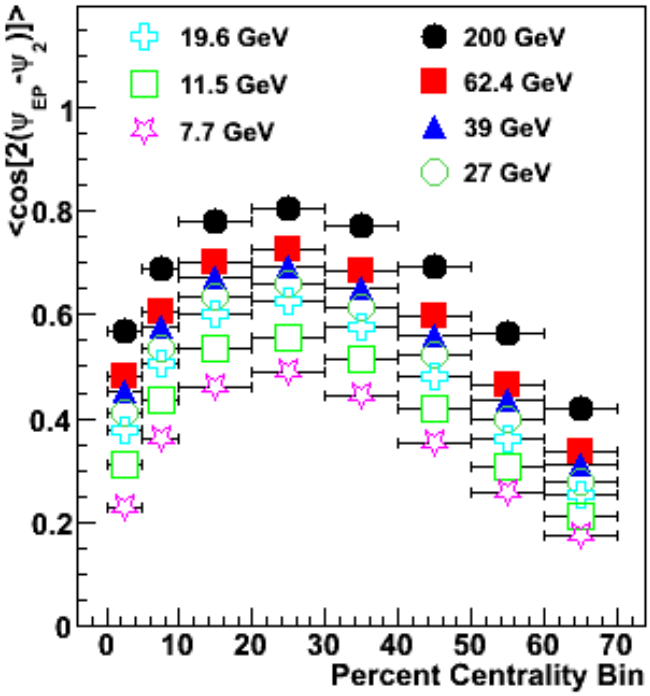

Figure 6.2: The event plane resolutions for Au+Au collisions at $\sqrt{s_{NN}} = 7.7$, 11.5, 19.6, 27, 39, 62.4 and 200 GeV as a function of collision centrality. The resolutions, computed using the TPC ($|\eta| < 1$), enter into both the correction algorithm and the global fit method.

effect later in the analysis. The n^{th} order event plane angle, ψ_n, is determined using charged particles measured in the TPC according to the equation

$$\psi_n = \frac{1}{n} \arctan\left(\frac{Q_y}{Q_x}\right) + \Delta\psi_n \tag{6.2}$$

where the components of the event plane vector are

$$Q_x = \frac{1}{N} \sum_i \left(w_i \cos(2\phi_i) - \langle Q \rangle_x\right) \tag{6.3}$$

$$Q_y = \frac{1}{N}\sum_i \left(w_i \sin(2\phi_i) - \langle Q\rangle_y\right) \tag{6.4}$$

Here, ϕ_i is the angle of the i^{th} track and N is the total number of tracks used to determine the event plane. The shift correction [11] is given by

$$\Delta\psi_n = \sum_{\alpha=1}^{\alpha_{\max}} \frac{2}{\alpha}(-\langle\sin(n\alpha\psi_n)\rangle\cos(n\alpha\psi_n) + \langle\cos(n\alpha\psi_n)\rangle\sin(n\alpha\psi_n)) \tag{6.5}$$

where α determines the order ($n\alpha$) that each correction term flattens. This analysis is performed relative to the second-order ($n = 2$) event plane.

For 7.7-39 GeV the ϕ-weighting method [11, 91–93] was used to flatten the event plane. The inverse, single particle, azimuthal distribution is used to weight each particle in the event plane determination so that inefficiencies do not affect the event plane determination. The ϕ-weight, $\phi_{\text{wgt,i}}$, is selected from this distribution for the i^{th} particle using the direction of the particle's transverse momentum vector, $\vec{p}_{T,i}$. In this case $w_i = \phi_{\text{wgt,i}} \cdot p_{T,i}$ while the recentering terms $\langle Q\rangle_x$ and $\langle Q\rangle_y$, as well as the shift term $\Delta\psi_n$, are all zero.

For 62.4 and 200 GeV a problematic sector of the TPC was turned off causing a rather non-uniform azimuthal distribution. In this case, the recentering and shift methods [11, 92, 94] were required to determine the event plane accurately. In this case, ϕ-weights were not applied so $w_i = p_{T,i}$. Here, the average offset in the direction of the p_T weighted flow vector, $\vec{Q}$, is used to compute $\langle Q\rangle_x$ and $\langle Q\rangle_y$. After this correction is applied, a shift method is needed to correct the event plane values for effects due to other harmonics. The shift term $\Delta\psi_n$ is determined by computing the correction terms $\langle\sin(n\alpha\psi_n)\rangle$ and $\langle\cos(n\alpha\psi_n)\rangle$ from $\alpha = 1$ up to $\alpha = 20$ terms, although generally $\alpha_{\max} = 2$ would be sufficient for a second order analysis [11].

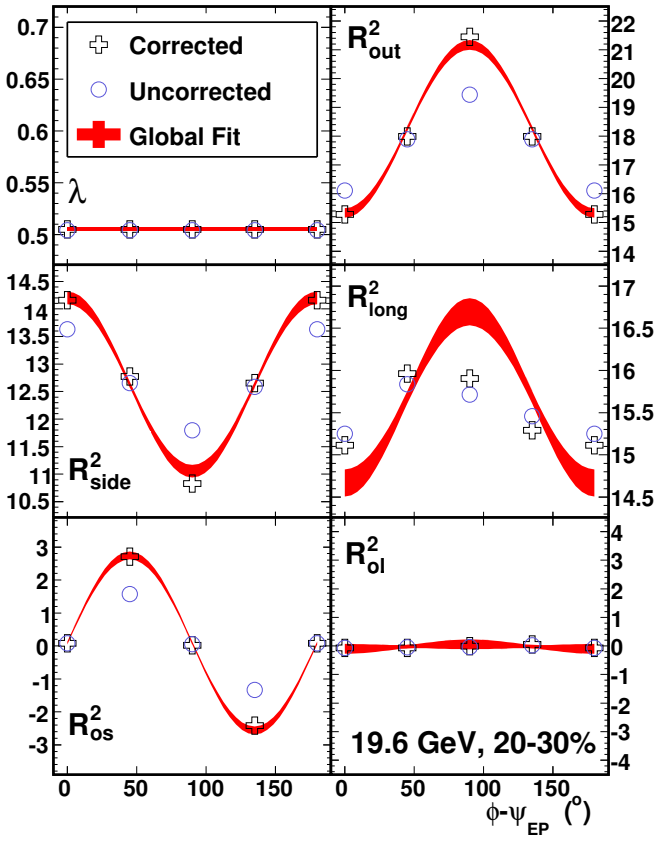

Figure 6.3: Examples of the radial oscillations of the HBT radii relative to the reaction plane from 20-30% central, 19.6 GeV Au+Au collisons for $0.15 < k_T < 0.6$ GeV/c. Open circles show the radii before correction for finite-bin-width and event plane resolution. Open cross symbols demonstrate that correcting these effects increases the oscillation amplitude. The corrected and uncorrected results are obtained with the standard fit method (see text) before and after the correction algorithm (Sec. 6.6) is applied. The points at 0° are reused at 180° for clarity. The solid band shows the Fourier decomposition directly extracted using a global fit (Sec. 6.7) to all four angular bins. The value of λ is consistent for the two methods.

The event plane resolution, $\langle\cos[2(\psi_{\rm EP} - \psi_2)]\rangle$, is also needed as it enters the correction algorithm described later. The calculation begins by determining two event planes for two independent subevents which in this analysis correspond to the $\eta < 0$ and $\eta > 0$ regions, so called η subevents. These subevent plane estimates are processed through an iterative procedure to solve for the full event plane resolution as outlined in [11]. Resolutions are reduced for lower multiplicity (and therefore lower energy) as well as more round (less anisotropic) cases. The values at each energy that enter this specific analysis are included in Fig. 6.2.

6.5 Fourier coefficients

In the azimuthal HBT analysis, four correlation functions are constructed, for pairs directed in four different angular bins centered at $\Phi = 0°$, $45°$, $90°$, and $135°$ relative to reaction plane. As described in the last chapter, the HBT radii in these different bins exhibit sinusoidal oscillations relative to the reaction planes. Figure 6.3 shows an example of these oscillations. The Φ dependence of the HBT radii are described by:

$$R^2_\mu(k_T,\Phi) = R^2_{\mu,0}(k_T) + 2\sum_{n=2,4,6\ldots} R^2_{\mu,n}(k_T)\cos(n\Phi) \qquad (\mu = o,s,l,ol) \quad (6.6)$$

and

$$R^2_\mu(k_T,\Phi) = R^2_{\mu,0}(k_T) + 2\sum_{n=2,4,6\ldots} R^2_{\mu,n}(k_T)\sin(n\Phi) \qquad (\mu = os) \quad (6.7)$$

where $R^2_{\mu,n}$ are the $n^{\rm th}$-order Fourier coefficients for radius term μ. These coefficients are computed using

$$R^2_{\mu,n}(k_T) = \begin{cases} \langle R^2_\mu(k_T,\Phi)\cos(n\Phi)\rangle & (\mu = o,s,l,ol) \\ \langle R^2_\mu(k_T,\Phi)\sin(n\Phi)\rangle & (\mu = os) \end{cases} \quad (6.8)$$

The 0^{th}-order Fourier coefficients are expected to be nearly identical to radii extracted in an azimuthally integrated analysis (which is observed, see results Sec. 8.2). The 2^{nd}-order terms correspond to half the amplitude of the second order oscillations for a second order, $n = 2$, analysis.

Once the Fourier coefficients are extracted the eccentricity, defined as

$$\varepsilon_F = \frac{\sigma_y^2 - \sigma_x^2}{\sigma_y^2 + \sigma_x^2} \approx 2\frac{R_{s,2}^2}{R_{s,0}^2} \tag{6.9}$$

can be simply computed from the Fourier coefficients [87]. The quantities σ_y and σ_x correspond to the widths of the fireball at kinetic freeze-out in the out-of-plane and in-plane directions, respectively. This definition allows negative eccentricities if $\sigma_y < \sigma_x$ which would indicate the system expanded enough to become in-plane extended. Whether or not that happens is related to the collision dynamics and equation of state as described in Sec. 2.3. The ratio $R_{s,2}^2/R_{s,0}^2$ is used to estimate ε_F because R_{side} is less affected by flow so it carries primarily geometric information [87]. Recall in Section 5.7 that Eq. 5.26 was the only equation relating the HBT radii and source geometry that had no dependence on temporal or dynamical variables.

6.6 Correction algorithm

The distributions for each of the four angular bins are smeared together partially due to imperfect event plane resolution. In the limit of zero event plane resolution the distributions would become indistinguishable and no oscillation of the radii would be observed. For finite but imperfect event plane resolution, the amplitude of the observed oscillations are reduced from the true value. Also, due to using pairs from a range of angles relative to the reaction plane, for instance $90^\circ \pm 22.5^\circ$, average values of the radii in this range are obtained which must nessecarily be slightly lower than

the true peak amplitude. These effects must be corrected for in order to extract the true 2^{nd}-order oscillation amplitudes needed to compute ε_F.

In some previous analyses the radii have been extracted and the oscillation amplitudes then scaled by the event plane resolution to get the corrected 2^{nd}-order Fourier coefficients. In this analysis, as in [17], a model independent correction algorithm is applied to compute the corrected numerator, denominator, and Coulomb weighted denominator histograms for each angular bin. These corrected distributions are then used in the fits to directly extract the true radii. We briefly summarize this correction procedure.

The derivation in [88], requires first decomposing the true and experimental distributions in Fourier series. The true distributions are then convolved with a (Gaussian) distribution of the reconstructed event plane about the true event plane and a function to account for the finite azimuthal bin width. Finally, each coefficient from the series for the true distrubtion is equated with the corresponding coefficient from the series expansion of the experimental distribution. This leads to the following relationship between coefficients for the true and experimentally observed distributions:

$$A_{\alpha,n}^{\text{exp}}\left(\vec{q}\right) = A_{\alpha,n}\left(\vec{q}\right)\frac{\sin(n\Delta/2)}{n\Delta/2}\langle\cos[n(\psi_{\text{EP}}-\psi_2)]\rangle. \tag{6.10}$$

The quantities $A_{\alpha,n}(\vec{q})$ and $A_{\alpha,n}^{\text{exp}}(\vec{q})$ are the coefficients for the Fourier series representation of the true and experimental distributions respectively. The formula applies separately to the numerator (A=N), the denominator (A=D) and the Coulomb weighted mixed event (A=K_{Coul}) distributions. The factors multiplying $A_{\alpha,n}(\vec{q})$ come from the convolution of the true series mentioned previously. The quantities $\langle\cos[n(\psi_{\text{EP}}-\psi_2)]\rangle$ are the reaction plane resolutions described earlier. The symbol Δ is the width of each angular bin and n is the order of the Fourier coefficient. The

experimental coefficients can be computed from the experimentally measured distributions in each angular bin using the standard definition for Fourier coefficients so that

$$A^{\rm exp}_{\alpha,n} = \begin{cases} \langle A^{\rm exp}_n(\vec{q},\Phi)\cos n\Phi\rangle & (\alpha = c) \\ \langle A^{\rm exp}_n(\vec{q},\Phi)\sin n\Phi\rangle & (\alpha = s) \end{cases} \tag{6.11}$$

are the coefficients for the cosine ($\alpha = c$) or sine ($\alpha = s$) terms in the series expansion.

The true, corrected distributions are computed from the experimental distributions using

$$A\left(\vec{q},\Phi_j\right) = A^{\rm exp}\left(\vec{q},\Phi_j\right) + 2\sum_{n=1}^{n_{\rm bins}} \zeta_n\left(\Delta\right) \times \left[A^{\rm exp}_{c,n}\left(\vec{q}\right)\cos(n\Phi_j) + A^{\rm exp}_{s,n}\left(\vec{q}\right)\sin(n\Phi_j)\right] \tag{6.12}$$

In this analysis only the $2^{\rm nd}$-order event plane (ψ_2) is measured and so only the $n = 2$ terms are required. The correction parameter $\zeta_2(\Delta)$ is given by

$$\zeta_n\left(\Delta\right) = \frac{n\Delta/2}{\sin(n\Delta/2)\langle\cos[2(\psi_{\rm EP} - \psi_2)]\rangle_p} - 1. \tag{6.13}$$

When this factor multiplies a coefficient in Eq. 6.12 it replaces the experimentally observed coefficient by the true, corrected coefficient. All quantities on the right hand side of Eq. 6.12 and 6.13 are measured experimentally.

Once the corrected numerator, denominator, and Coulomb weighted mixed-event distributions are computed for each angular bin, fits are performed to extract the radii. As in [17], the λ parameter from the four angular bins are averaged (for each centrality) and set as a constant for all four bins; the $\langle\lambda\rangle$ values are nearly identical to the non-azimuthal cases. The correlation functions are refit to extract the radii. The λ-fixing procedure reduces the number of independent fit parameters needed. This procedure is done under the assumption that λ has no explicit Φ dependence, none has been observed.

In any case, the HBT radii extracted from these corrected distributions exhibit the true, larger oscillation amplitude. This is clearly demonstrated in Figure 6.3. One deficiency in this approach is that the uncertainties on the corrected distributions are correlated, leading to an underestimate of the uncertainties for the extracted radii. A new approach, the "global fit" method, is developed to avoid this and to try to get more reliable results in cases where the statistics and resolution are very low.

In earlier azimuthal analyses E895 and CERES simply divided the uncorrected oscillation amplitudes by the event plane resolution as is done in v_2 analyses. Although the results are rather consistent, it is not the formally correct approach.

To distinguish between the three methods, in the remainder of this paper, fitting the uncorrected distributions and then scaling by the resolution will be referred to as the "v_2-type" correction method. The process of first applying the correction algorithm to the distributions before extracting the radii, separately for each angular bin (with Eq. 6.1), will be referred to as the "standard fit" method.

6.7 Global fit method

A new global method of fitting was developed that avoids correlated errors and provides more reliable results in cases of low statistics and poor event plane resolution. The method begins with the same Gaussian parameterization in Eq. 6.1. The Fourier representation of the radii from Eqs. 6.6 and 6.7 are substituted, keeping only the 0^{th}- and 2^{nd}-order terms. In this method, the fit parameters are the Fourier coefficients that describe the oscillations of the radii relative to the event plane, and so the Fourier coefficients are extracted directly rather than the radii. Using this parameterization, the theoretical estimate of the numerator is then smeared for event plane resolution

and finite-binning effects by applying the correction algorithm in reverse, as described below. In this way, a theoretical estimate of the values expected in each uncorrected numerator is obtained which can then be compared to the uncorrected numerators that are measured.

For each bin $\vec{q}$=(q_o,q_s,q_l), a value of the correlation function, $C(\vec{q})$, is computed. An estimate for the denominator is obtained from the "true" denominator (i.e., the denominator for a given Φ bin run through the correction algorithm described in the last section). The estimate for the true numerator, for each $\vec{q}$ bin, is simply $N(\vec{q}) = D(\vec{q})C(\vec{q})$. This value is then run through the correction algorithm in reverse. A series similar to Eq. 6.12,

$$\begin{aligned} A^{\text{smeared}}(\vec{q},\Phi_j) = A^{\text{theory}}(\vec{q},\Phi_j) + 2\sum_{n=1}^{n_{\text{bins}}} \zeta_n^{'}(\Delta) \\ \times [A_{c,n}^{\text{theory}}(\vec{q})\cos(n\Phi_j) + A_{s,n}^{\text{theory}}(\vec{q})\sin(n\Phi_j)] \end{aligned} \tag{6.14}$$

is used to compute the value expected to appear in the uncorrected numerator for each (q_o,q_s,q_l) bin and each Φ bin. The quantity A^{smeared} is the value expected in the uncorrected numerator, based on the value, A^{theory}, predicted by the current values of the fit parameters. All fit parameters (including normalizations) obtained in this method correspond to the true correlation function even though the fit is applied to the uncorrected numerators. As in Eq. 6.12, $n = 2$ terms are used for an analysis relative to the second order event plane.

A factor similar to Eq. 6.13, from the relationship between true and experimental values (for $n = 2$),

$$\zeta_n^{'}(\Delta) = \frac{\sin(n\Delta/2)\langle\cos[2(\psi_{\text{EP}} - \psi_2)]\rangle_p}{n\Delta/2} - 1 \tag{6.15}$$

smears the true amplitude according to the resolution and bin-width.

In this way an estimate of the value that should be found in the uncorrected, raw numerator histogram for each (q_o,q_s,q_l) bin and for each Φ bin is obtained. The fit then compares this value to the values in the four uncorrected numerator histograms for all four Φ bins in a single simultaneous "global" fit.

A separate normalization is used for each Φ bin since there will be differences in the number of tracks, and therefore pairs, in the different bins. A single λ parameter is used for all four angular bins, as is done in the standard fit method. This method significantly reduces the number of parameters needed (besides the four normalizations) to describe the data. In the standard fit method 21 parameters (λ + 5 radii x 4 Φ bins) are needed. The global fit method requires only 11 parameters (λ + 10 Fourier coefficients).

The standard correction algorithm computes a corrected histogram from all of the uncorrected histograms. Therefore, the uncertainties in each corrected histogram depend on the uncertainties in all the uncorrected histograms. While the uncertainties are independent in the uncorrected histograms, the uncertainties in the "corrected" histograms are not. However, the fit assumes the uncertainties are independent and, as a result, underestimates the true uncertainty. The new global fit method, by fitting directly to the uncorrected numerator histograms, avoids this problem.

A disadvantage of the new algorithm is that the normalizations obtained correspond to the "true" correlation function, $C^{\rm true}(\vec{q}) = N^{\rm corr}(\vec{q})/D^{\rm corr}(\vec{q})$, but the fit uses the corrected denominator histogram, $D^{\rm corr}$, and the uncorrected numerator histogram, $N^{\rm uncorr}$. To compare the fit to the distributions that are actually used in the fit, $C(\vec{q}) = N^{\rm uncorr}(\vec{q})/D^{\rm corr}(\vec{q})$ is projected but the normalizations do not correspond

exactly. They do put the projections on a common scale however. The 0° and 90° projections are shifted away from unity at large $\vec{q}$. Examples of the projections using the global fit method are shown in Fig. 6.4 for the same centrality and energy as the fits using the standard fit method, also shown in Fig. 6.4 for comparison. As a check, if instead one projects $N^{\rm corr}(\vec{q})/D^{\rm corr}(\vec{q})$ and $N^{\rm fit}(\vec{q})/D^{\rm corr}(\vec{q})$, where $N^{\rm fit}(\vec{q})$ is the unsmeared fit numerator computed from the extracted Fourier coefficients, the projections look essentially identical to the standard fit method projections for all four angular bins.

For most centralities and fit parameters, the results agree quite well. However, the amplitude describing the $R^2_{\rm long}$ oscillation, $R^2_{l,2}$, is larger when obtained using the new fit method. The difference in $R^2_{l,2}$ for the two parameterizations means that the second order oscillation that best fits the data from all angular bins simultaneously is not consistent with the Gaussian $R_{\rm long}$ values that best describe the regions of homogeneity in each angular bin separately. The difference may be attributed to a subtle interdependence of the fit parameters in the standard fit method that constrains the $R_{\rm long}$ values. Also, the new fit method has difficulties in all central 0-5% cases and in a few 5-10% cases when the statistics become low. For some of the 0-5% cases the fit could never converge even with high statistics. While the $R^2_{ol,2}$ values are close to zero in the standard fit results for all centralities, a large $R^2_{ol,2}$ suddenly appears only in this most central bin, only when using this global fit method. This should not happen because for a symmetric acceptance window around mid-rapidity R^2_{ol} must average to zero. Additionally, because the different angular bins are most similar in central events any second order oscillation of $R^2_{ol,2}$ should decrease in the most central bin due to symmetry, not appear suddenly. In fact when $R^2_{ol,2}$ is varied, the χ^2 value

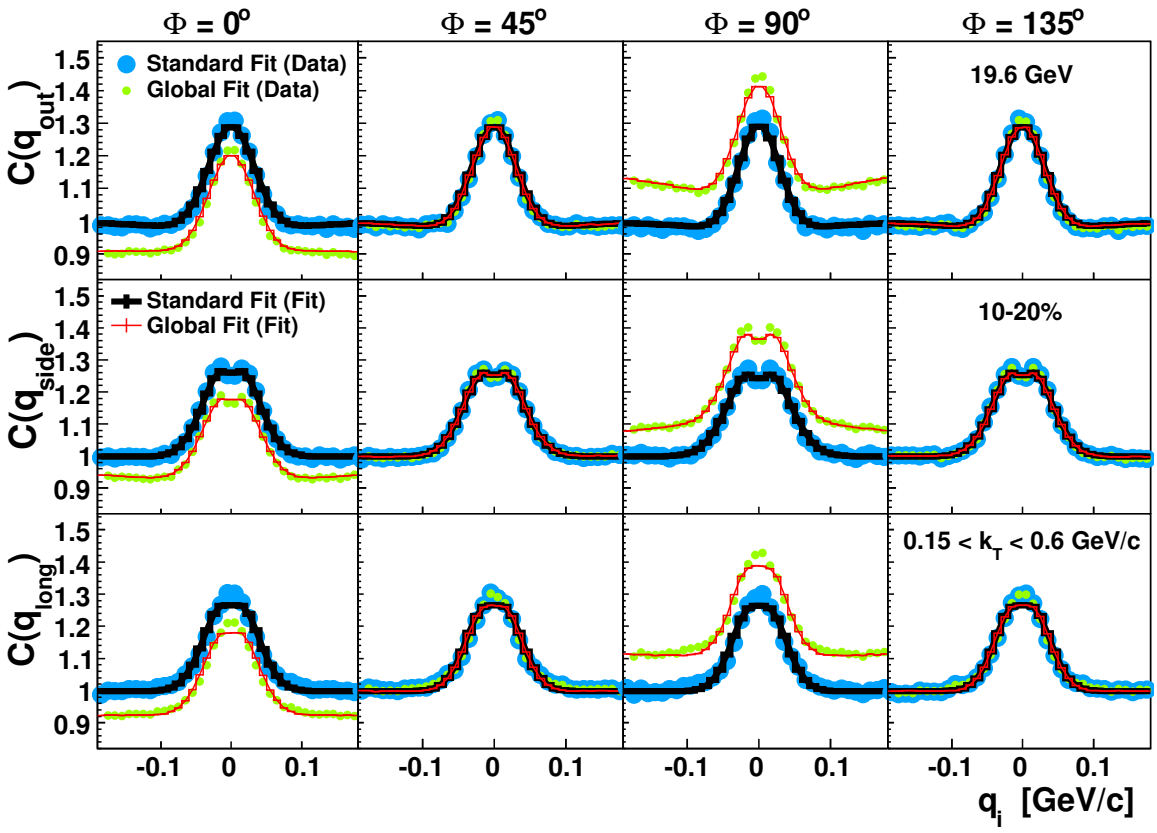

Figure 6.4: Sample fit projections onto the q_{out} (top row), q_{side} (middle row) and q_{long} (bottom row) axes for four angular bins relative to the reaction plane. Results from the standard fit method and the global fit method are shown for direct comparison. These projections are from results for 10-20% central, 19.6 GeV Au+Au collisions with $0.15 < k_T < 0.6$ GeV/c.

between the fit and the data becomes quite flat for the central data compared to other centralities allowing $R^2_{ol,2}$ to take on a wide range of values without constraint. Additionally, when this happens the oscillations extracted for some, or sometimes all, of the other parameters ($R^2_{o,2}$, $R^2_{s,2}$, $R^2_{l,2}$) change sign in this central case, even when statistics are high.

Due to symmetry of the almost round central events, the distributions for different angular bins are quite similar compared to other centralities. The global fit method extracts oscillations, not radii, from all four bins simultaneously and when the distributions are similar it seems to have the freedom to find a wider variety of solutions. The standard fit method, with separate fits in each azimuthal bin, has no such freedom, but is found to be less reliable when statistics and resolutions are low. For other centralities the results are rather stable and, the 0^{th}-order coefficients, even for 0-5% centrality, always remain consistent with the azimuthally integrated results. The behavior for central data appears to be the result of the relationship between the fit parameters used in this parameterization, the similar shape of the emission regions for all the angular bins in the central data, and the very shallow minimum in χ^2 that develops for $R^2_{ol,2}$ at the same time. There are no other differences in the global fit algorithm compared to the standard fit method.

Chapter 7: Event, track, and pair selections and systematic uncertainty

The various selection criteria and binning of data that are used in the analyses are described in the first three sections of this chapter which correspond to Section III B-D in [85]. The last section provides a discussion of systematic uncertainties which is taken from Section IV E of [85].

7.1 Event selection

Events included in the analysis were selected using the reconstructed vertex position. The radial vertex position ($V_R = \sqrt{V_X^2 + V_Y^2}$) was required to be less than 2 cm to reject collisions with the beam pipe. The vertex position along the beam direction, V_Z, was required to be near the center of the detector as summarized in Table 7.1, with larger ranges at 7.7 and 11.5 GeV to maximize statistics. The number of events at each energy used in this analysis are also listed in Table 7.1.

The events were binned in different centrality ranges. For the azimuthal HBT analysis the centrality bins studied were 0-5%, 5-10%, 10-20%, 20-30% and 30-40%. For the non-azimuthal HBT analysis, additional 40-50%, 50-60%, 60-70% bins were also studied. Events were mixed only with other events in the same centrality bin and with relative z vertex positions of less than 5 cm. For the azimuthally sensitive

$\sqrt{s_{NN}}$ (GeV)	$\lvert V_Z \rvert$ (cm)	N_{events} (10^6)
7.7	< 70	3.9
11.5	< 50	10.7
19.6	< 30	15.4
27	< 30	30.8
39	< 30	8.8
62.4	< 30	10.1
200	< 30	11.6

Table 7.1: Number of analyzed events and z-vertex range, V_Z, at each energy.

analysis, events were also required to have the estimated reaction plane within 22.5°, similar to an earlier analysis [17]. Reducing the width of the mixing bins only changes the relative normalizations in the different angular bins but has no effect on the other parameters. The study in Appendix A.1 demonstrates this by comparing results using 8, 9, and 12 azimuthal mixing bins.

7.2 Particle selection

Tracks were selected in three rapidity ranges: $-1 < y < -0.5$ (backward rapidity), $-0.5 < y < 0.5$ (mid-rapidity), and $0.5 < y < 1$ (forward rapidity). Each track was required to have hits on more than 15 (out of 45 maximum) of the TPC pad rows to ensure good tracks. A distance of closest approach requirement, $DCA < 3$ cm, was imposed to reduce contribution from non-primary pions.

Particle identification is accomplished by measuring energy loss in the gas, dE/dx, for each track and comparing to the expected value for each species ($i = e^{\pm}$,$\pi^{\pm}$,$k^{\pm}$,p,$\bar{p}$)

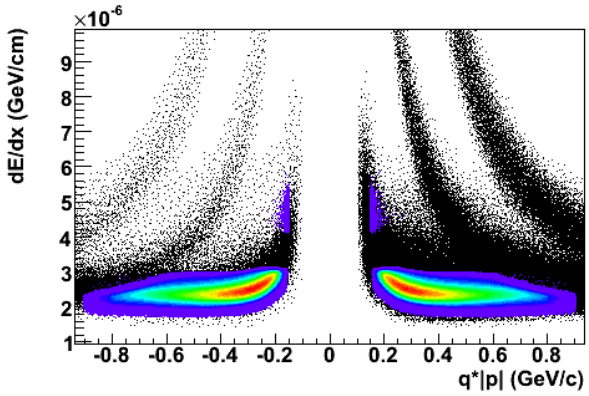

Figure 7.1: The energy loss, dE/dx, demonstrates that particle idendification (and other particle selection criteria) effectively selects pions (colored contour region) that are well separated from the kaon, proton, and electron bands (shown in black). The gaps in the colored region at $|p| \approx 0.2$ GeV/c are caused by the cut to eliminate electrons from the analysis in the region where the electron and pion band overlap.

using the equation

$$n\sigma_i = \frac{1}{\sigma_i} \log \left(\frac{dE/dx_{\text{measured}}}{dE/dx_{\text{expected},i}} \right) \tag{7.1}$$

where σ_i is the dE/dx resolution of the TPC. Tracks with $n\sigma_\pi < 2$ allow identification of pions for use in the analysis. An additional requirement that $n\sigma_e$, $n\sigma_k$, and $n\sigma_p > 2$ supresses contamination from other particles. Additionally, a transverse momentum cut, $0.15 < p_T < 0.8$ GeV/c, further ensures particles come from the region where the pion band is separated from the kaon band. Any contamination is estimated to be less than 1.7% even before the $n\sigma$ cut to reject kaons. Figure 7.1 demonstrates that these cuts effectively remove non-pions.

7.3 Pair cuts and binning

7.3.1 Split tracks

Track splitting occurs when a single charged particle track is reconstructed as two separate tracks that appear to have nearly identical momenta. The relative momenta of these artificial pairs is very small and therefore extra entries appear in the region of the correlation function that carries the signal. As described in Sec. 6.1, the correlation function is the ratio of the relative momentum distribution for particles in the same event (numerator) to the distribution for particles from mixed events (denominator) that exhibits a signal peak at low relative momentum. The artificial pairs caused by track splitting appear only in the numerator, artificially increasing the peak in the correlation function. A process to remove track splitting effects was described in [86] where a "splitting level", $SL < 0.6$ was required. Analogous studies show the same cut is effective at removing track splitting in the more recent data sets so $SL < 0.6$ is required for all pairs in the current analysis. More discussion of track splitting studies can be found in Appendix A.2.

7.3.2 Merged tracks

Compared to track splitting, track merging has the opposite effect on the correlation signal, reducing the observed peak at low relative momentum.

Since the tracks that carry the correlation signal have low relative momentum, they must follow similar trajectories through the detector. Track merging occurs when two such tracks are reconstructed as a single track. Therefore, the pairs they would form with each other (and other particles) are missed in the analysis. This reduces the number of pairs in the numerator in the signal region. No such merging

effect occurs in the mixed event denominator because the tracks from separate events were reconstructed independently. Again, in [86] a technique to remove track merging effects was developed. As discussed in Sec. 4.2, if two tracks have hits on the same padrow that are too close together they would appear as a single "merged" hit. Two tracks with such "merged" hits on many of the 45 TPC padrows are more likely to be reconstructed as single merged track. For each pair of tracks, the fraction of hits that are close enough so they would appear merged is computed. The same algorithm can be applied to track pairs from the numerator and denominator. The allowed fraction of merged hits (FMH) can be reduced until the effect is eliminated. In [86] it was determined that $FMH < 10\%$ reduced track merging effects as much as possible. While this approach eliminates the potentially large effect of track merging, it introduces a systematic uncertainty due to the non-Gaussianess of the correlation function [86]. The azimuthal HBT analysis is more sensitive to the track merging cut and allows the systematic uncertainty associated with this requirement to be estimated in Sec. 7.4. Analogous studies to those in [86] lead to the same conclusions so in the present analyses a requirement that $FMH < 10\%$ is imposed to remove effects of track merging for all energies studied. Additional information related to investigations of track merging effects can be found in Appendix A.3.

7.3.3 k_T cut and pair binning

Similar to previous analyses [17, 86, 95, 96] pairs were required to have average transverse pair momenta, $k_T = (|\vec{p}_{1T} + \vec{p}_{2T}|)/2$, in the range $0.15 < k_T < 0.6$ GeV/c. For the non-azimuthal HBT analyses four k_T bins were used: [0.15,0.25] GeV/c, [0.25,0.35] GeV/c, [0.35,0.45] GeV/c, [0.45,0.6] GeV/c. This binning allows

the presentation of results as a function of mean k_T (or $m_T = \sqrt{k_T^2 + m_\pi^2}$) in each bin. These bins yield mean k_T values similar to those in the historical data allowing direct comparison of certain quantities to previously observed trends.

In earlier azimuthal HBT studies by CERES [16] and STAR [17] the analysis was performed in similar, narrow k_T bins. For an azimuthally differential HBT analysis the statistics are spread across at least four additional azimuthal bins. At the lowest energies this did not allow for sufficient statistics. For instance, the 7.7 GeV dataset has both the fewest number of events and the lowest multiplicity per event in each centrality bin. Reliable results could not be obtained from data split into both multiple k_T and multiple bins relative to the reaction plane. Instead, a single k_T-integrated analysis was performed using all pairs in the combined range $0.15 < k_T < 0.6$ GeV/c with $\langle k_T \rangle \approx 0.31$ GeV/c. The eccentricity at kinetic freeze-out exhibits a systematic decrease by as much as 0.02 when using a single, wide k_T range compared to analyses when results from several narrow k_T bins are averaged. This is simply because the lowest k_T bin appears to give slightly smaller eccentricities. Therefore, when a wide bin is used the results are biased toward the low k_T results due to the much higher statistics of the low k_T pairs. In the earlier analyses, CERES reported a weighted average of results for different k_T bins, while STAR used an average without statistical weights. In any case, to compare the present results as a function of $\sqrt{s_{NN}}$ the same k_T integrated range was used for all energies.

For the azimuthally differential analysis, the pairs were separated into four 45° wide azimuthal bins relative to the reaction plane direction using the angle $\Phi = \phi_{\text{pair}} - \psi_2$. The angle of each pair, ϕ_{pair}, is the azimuthal angle of the average pair transverse momentum vector, $\vec{k}_T$, and ψ_2 is the second-order event plane angle defined in the

Source	R_{out}	R_{side}	R_{long}	ε_F
Coulomb	4%	3%	4%	0.004
Fit Range	5%	5%	5%	0.002
FMH	7%	3%	3%	0.003
Total	9.5%	6.5%	7%	0.005

Table 7.2: The approximate systematic uncertainty on the HBT radii and freeze-out eccentricities.

range $[0, \pi]$. This allows measurement of the oscillations of parameters necessary to estimate the freeze-out eccentricity as projected on the transverse plane. A first order analysis could provide additional information at the lowest energies [8, 80]. However, significant additional work is needed to obtain first order results due to complications from relatively low statistics spread across more bins and with much lower first order (compared to second order) event plane resolutions.

7.4 Systematic uncertainties

The sources of systematic uncertainty have been studied in previous HBT analyses such as [17, 86, 95, 96]. Similar studies have been used to estimate the systematic uncertainty due to the Coulomb correction, fit range, and fraction of merged hits (FMH) cut discussed earlier. Track splitting is effectively eliminated. The estimated uncertainty on the HBT radii and freeze-out eccentricity from each source are summarized in Table 7.2.

Earlier STAR analyses [17, 86, 95, 96] found, for various collision species (p+p, Cu+Cu, Au+Au) and data sets that the systematic uncertainty is approximately 10%

or less for the HBT radii in all centrality and k_T bins studied. Analogous studies lead to the same conclusion for the data sets used in the current analysis.

It should be noted that there is also an inherent uncertainty in the general method used to extract the eccentricity. The theoretical framework assumes a static, Gaussian region of homogeneity that corresponds to the entire volume of the collision at kinetic freeze-out. Flow-induced space-momentum correlations reduce this correspondence which could affect the reliability of the equations. However, several different model studies [80, 87] find consistently that the results are still reliable to within 30% even in the presence of strong flow. This would not affect any conclusions regarding the shape of the excitation function in regards to whether or not it is monotonic.

Chapter 8: Results

The azimuthally integrated HBT results are discussed first and compared to historical data from earlier experiments and recent results from ALICE. Later, the azimuthally differential analysis is presented for a wide range of beam energies. The azimuthally differential analysis is also performed in three rapidity bins allowing extraction of the excitation function for the R_{ol}^2 parameter and to directly compare the freeze-out eccentricity in the same forward rapidity window as an earlier measurement by the CERES collaboration. Finally, the excitation function for the freeze-out eccentricity is discussed along with its implications for the relevant underlying physics as outlined in Sec. 2.3. The material presented in this chapter is adapted directly from Section VI of Reference [85], the paper pertaining to the research for this thesis.

8.1 Azimuthally integrated HBT

There is a wealth of historical HBT data demonstrating the systematic behavior of the HBT radii as a function of beam energy, k_T (or m_T), and centrality. The trends have been established despite the measurements having been performed by various experiments and with differences in the analysis techniques. In this paper, the results are presented across a wide range of beam energies, overlapping previously measured regions and filling in previously unmeasured regions of $\sqrt{s_{NN}}$.

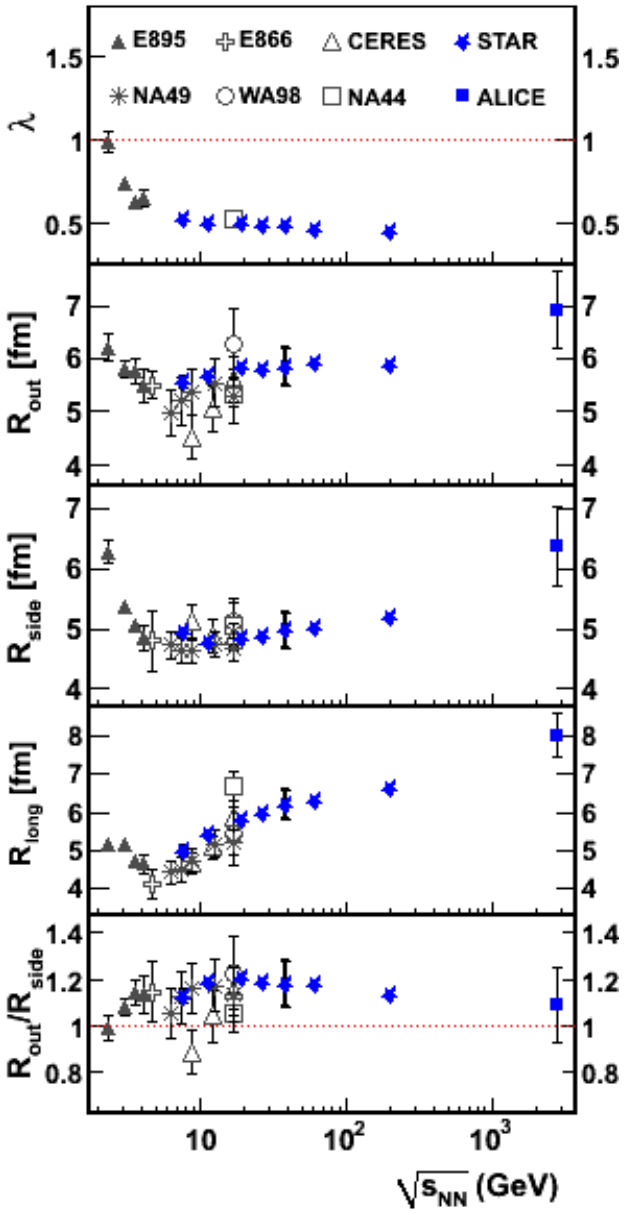

Figure 8.1: Energy dependence of the HBT parameters for central Au+Au, Pb+Pb, and Pb+Au collisions at mid-rapidity and $\langle k_T \rangle \approx 0.22$ GeV/c [97–103]. The text contains discussion about variations in centrality, k_T, and analysis techniques between experiments. Errors on NA44, NA49, WA98, CERES and ALICE points include systematic errors. The 39 GeV point includes the approximate systematic uncertainty (from Table 7.2) typical of the STAR results at all energies. Errors on other results are statistical only. Forsome experiments the λ value was not specified.

Figure 8.1 shows the beam energy dependence of the λ parameter, the HBT radii, and the ratio $R_{\rm out}/R_{\rm side}$ for central collisions at low k_T. All the STAR results are from the most central 0-5% and lowest $\langle k_T \rangle$ (≈ 0.22 GeV/c) data. The ALICE point is also from 0-5% central data, but has a slighly larger $k_T \approx 0.26$ GeV/c. Historical results from earlier experiments come from a range of central data sets, as narrow as 0-7.2% to as wide as 0-18% centrality, as well as a range of $\langle k_T \rangle$ values, from 0.17 GeV/c to 0.25 GeV/c. The historical data are from π^--π^- correlation results in which various methods of accounting for the Coulomb interaction were employed. The new STAR results are from combined π^--π^- and π^+-π^+ correlation functions. No significant difference between the two cases has been observed so the combination simply leads to higher statistics. Our high-statistics analysis, with identical acceptance for all $\sqrt{s_{NN}}$, yields a well-defined smooth excitation function consistent with previous trends.

The λ parameter primarily represents the fraction of correlated pairs entering the analysis, as described in Sec. 6.2. It decreases relatively rapidly at lower, AGS, energies while changing rather little from 7.7 to 200 GeV. This suggests that the fraction of pions in this $\langle k_T \rangle$ range from long-lived resonances increases at lower energy but remains rather constant at higher energies. The $R_{\rm out}$ parameter similarly shows little change over a wide range of RHIC energies. It does appear to rise noticably at the LHC. The values of $R_{\rm side}$ show a very small increase at the higher RHIC energies and a more significant increase at the LHC. The values of $R_{\rm long}$, on the other hand, appear to reach a minimum around 5 GeV, rising significantly at RHIC and the ALICE point once again rises more rapidly than the trend observed at STAR.

The radius $R_{\rm side}$ is primarily associated with the spatial extent of the particle emitting region whereas $R_{\rm out}$ is also affected by dynamics and is believed to be related

to the duration of particle emission. The ratio $R_{\rm out}/R_{\rm side}$ was predicted to increase with beam energy by hydrodynamical calculations and might show an enhancement if the lifetime were to be extended by entrance into a different phase [104, 105]. The previous observation that this quantity shows a quite flat energy dependence is reproduced with the scatter in data points greatly reduced and the region between SPS and previous RHIC measurements covered. The trend remains flat up to LHC energies. The ability of various models to reproduce this trend is discussed in [95].

The value of $R_{\rm long}$ has been related to the freeze-out temperature and lifetime of the system by the relation [87, 106, 107]

$$R_{\rm long} = \tau\sqrt{\frac{T}{m_T}\frac{K_2(m_T/T)}{K_1(m_T/T)}} \tag{8.1}$$

where $K_1(m_T/T)$ and $K_2(m_T/T)$ are modified Bessel functions. The freeze-out temperature, T, is not expected to change much with $\sqrt{s_{NN}}$. Therefore, the rise of $R_{\rm long}$ suggests that the total lifetime, τ, of the system is increasing with energy. At the end of this section Eq. 8.1 will be used to extract, τ as a function of $\sqrt{s_{NN}}$ given certain assumptions.

Figure 8.2 shows the $\langle m_T \rangle$ dependence of the HBT parameters for each energy. As mentioned earlier, in Sec. 5.4, the decrease in transverse and longitudinal radii at higher m_T are attributed to transverse and longitudinal flow [87, 108] Larger m_T pairs are emitted from smaller emission regions with less correspondence to the size of the entire fireball. For both $R_{\rm out}$ and $R_{\rm side}$, the different beam energies show nearly identical trends both in magnitude and slope. For $R_{\rm long}$, the slopes appear to remain consistent for the different energies but the magnitude, for all centralities, appears to increase at higher energies. From these observations and considering Figure 8.1

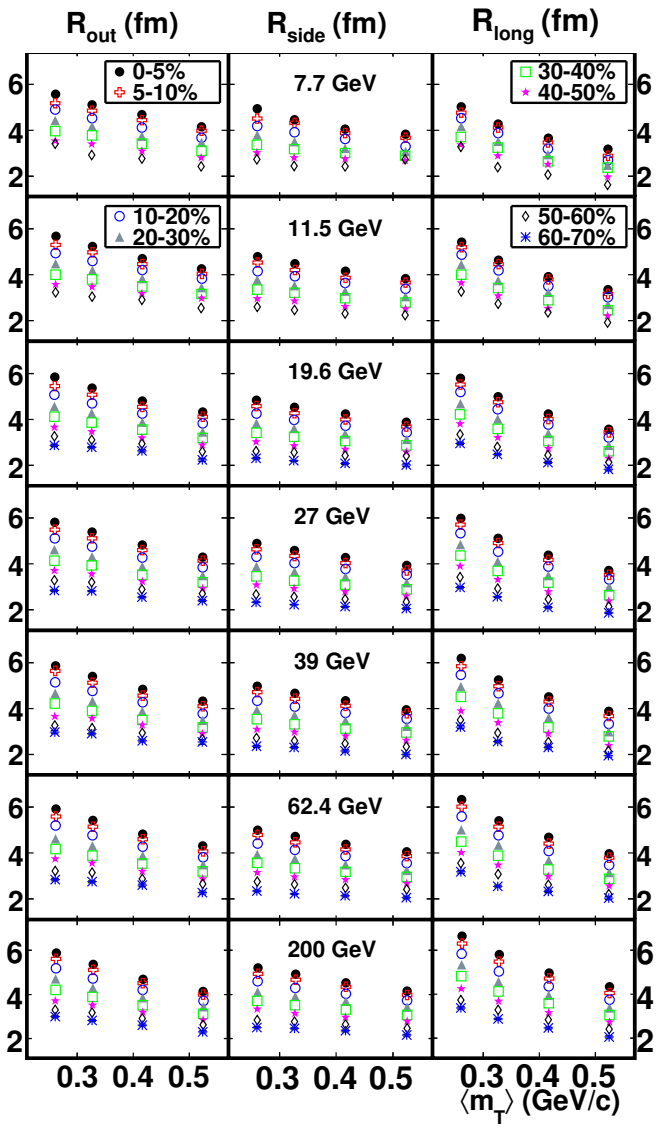

Figure 8.2: The $\langle m_T \rangle$ dependence of $R_{\rm out}$, $R_{\rm side}$ and $R_{\rm long}$ for each energy and multiple centralities. For 7.7 GeV and 11.5 GeV, the results for 60-70% centrality are excluded due to lack of statistics.

showed the beam energy dependence for a single k_T and centrality bin it is apparent that similar dependences on $\sqrt{s_{NN}}$ exists for all the studied centrality and k_T ranges.

The multiplicity dependence of the HBT radii are presented in Fig. 8.3 for two k_T ranges with $\langle k_T \rangle \approx 0.22$ GeV/c and $\langle k_T \rangle \approx 0.39$ GeV/c. A few historical points with similar $\langle k_T \rangle$ are shown as well. It was observed in [95] that $R_{\rm side}$ and $R_{\rm long}$ both follow a common universal trend at 62.4 and 200 GeV independent of the collision species. ALICE has recently shown p+p collisions exhibit a different multiplicity dependence with a smaller slope [109, 110]. The difference may be due to the interactions in the bulk medium formed in heavy ion collisions.

The results from ALICE are at different $\langle k_T \rangle$ values. To get a similar $\langle k_T \rangle \approx 0.39$ GeV/c estimate, the ALICE data points [103] reported for $\langle k_T \rangle \approx 0.35$ GeV/c and $\langle k_T \rangle \approx 0.44$ GeV/c are averaged and plotted on Fig. 8.3. There is some ambiguity in this approach as the different pair statistics at different k_T are not accounted for when averaging this way. The universal trends for $R_{\rm side}$ and $R_{\rm long}$ appear to continue up to LHC energies. This has already been demonstrated clearly in [103, 109, 110].

In this paper, $\langle dN_{\rm ch}/d\eta \rangle$ was estimated in a consistent way for all the STAR results. This reduces the horizontal scatter that is present in the historical data due to differences in techniques used to estimate the multiplicity. The quantity $dN_{\rm ch}/d\eta$ is used as the standard definition of STAR's percent centrality bins and the mean value is simply computed using all events that pass event cuts and enter the analysis. However, it should be noted that this is an uncorrected value of $\langle dN_{\rm ch}/d\eta \rangle$ that underestimates the true value. This allows a qualitative comparison with other experiments. More precise quantitative comparison of the multiplicity dependence for STAR data to

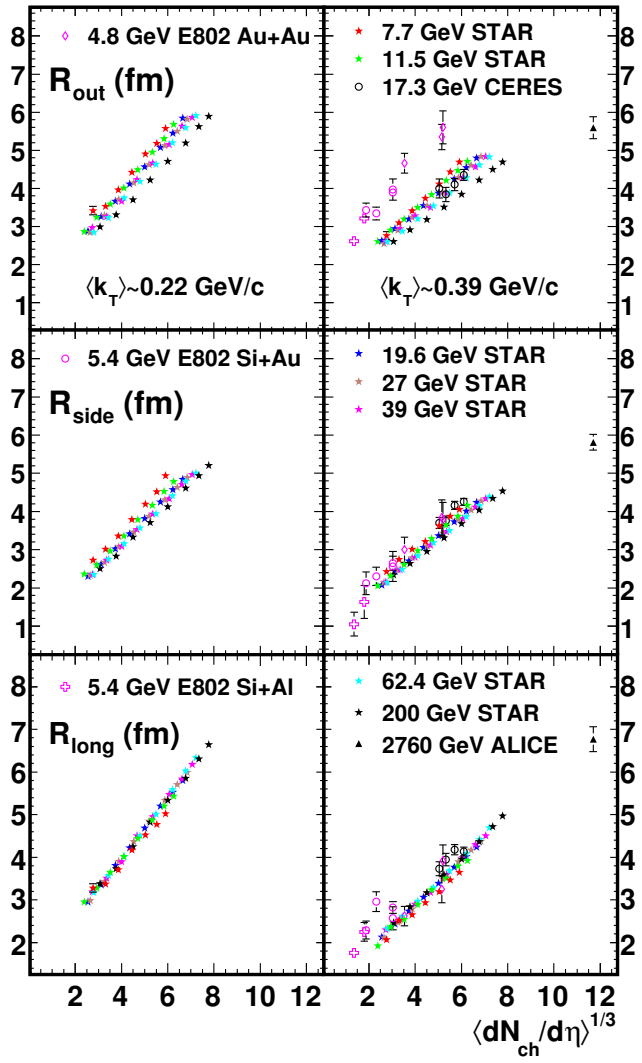

Figure 8.3: The dependence of the HBT radii on multiplicity, $\langle dN_{\rm ch}/d\eta\rangle^{1/3}$, for $\langle k_T\rangle \approx 0.22$ GeV/c (left) and $\langle k_T\rangle \approx 0.39$ GeV/c (right). Results are for Au+Au collisions at STAR, Pb+Pb at CERES [97] and ALICE [103], and Si+A at E802 [111].

results from other experiments should wait for publication of corrected values of $dN_{\rm ch}/d\eta$.

An estimate of the volume of the homogeneity regions, $V = (2\pi)^{3/2} R_{\rm side}^2 R_{\rm long}$, can be computed using the data in Fig. 8.1. These values are plotted in Fig. 8.4 as a function of $\sqrt{s_{NN}}$. The STAR results are all for 0-5% central collisions with $\langle k_T \rangle \approx 0.22$ GeV/c. Since the values are computed using the data in Fig. 8.1, all the same variations in centrality ranges and $\langle k_T \rangle$ values are present in the volume estimates too. The historical data suggest a minimum between AGS and SPS energies. The STAR results show a noticable increase in volume at the higher energies while the 7.7 and 11.5 GeV points are almost the same, consistent with a minimum in the vicinity of 7.7 GeV. The ALICE point rises significantly above the trend at lower energies so the regions of homogeneity are significantly larger in collisions at the LHC.

The CERES collaboration [113] has found that a constant mean free path at freeze-out,

$$\lambda_F \approx \frac{V}{(N_\pi \sigma_{\pi\pi} + N_N \sigma_{\pi N})} \approx 1 fm, \tag{8.2}$$

leads naturally to a minimum in the energy dependence of the volume that is observed. The yields of pions and nucleons, N_π and N_N, change with energy. Assuming the cross sections, $\sigma_{\pi\pi}$ and $\sigma_{\pi N}$ are constant with energy, the denominator in Eq. 8.2 reaches a minimum. To keep the mean free path at freeze-out constant, the volume also reaches a minimum. Above 19.6 GeV, the ratio of $N_\pi \sigma_{\pi\pi}/N_N \sigma_{\pi N}$ remains rather constant and the denominator in Eq. 8.2 increases with energy similar to the volume. Below 11.5 GeV, the $N_N \sigma_{\pi N}$ term becomes the dominant term and it increases at lower energies as does the volume. At higher energies, this mechanism is consistent with the nearly universal trend of the volume on $\langle dN_{\rm ch}/d\eta \rangle$ and therefore, $R_{\rm side}$ and $R_{\rm long}$

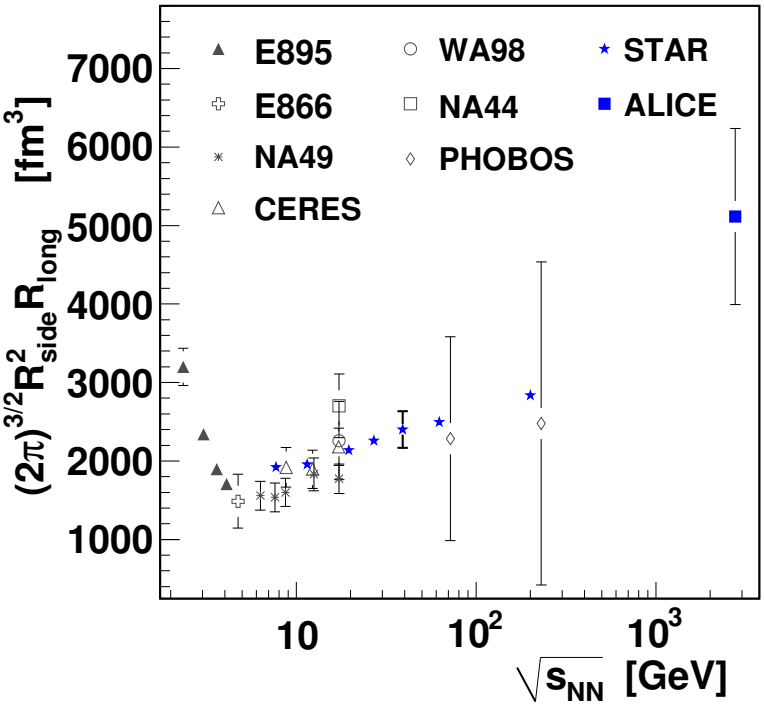

Figure 8.4: The beam energy dependence of the volume, $V = (2\pi)^{3/2} R^2_{\rm side} R_{\rm long}$, of the regions of homogeneity at kinetic freeze-out in central Au+Au collisions with $\langle k_T \rangle \approx 0.22$ GeV/c [97–103, 112]. The 39 GeV point shows the approximate systematic uncertainty (from Table 7.2) typical of the STAR results. The PHOBOS points are offset in $\sqrt{s_{NN}}$ for clarity. The text contains some discussion about variations in centrality, $\langle k_T \rangle$, and analysis techniques between different experiments.

on $\langle dN_{\rm ch}/d\eta\rangle^{1/3}$ [95]. It is interesting that the trend for $R_{\rm side}$ begins to deviate from this trend slightly for 7.7 and 11.5 GeV in Fig. 8.3, which is the same region where the system changes from π-N to π-π dominant. Also, the argument above neglects the influence from less abundant species including kaons, but it has been observed that strangeness enhancement occurs in this same region of $\sqrt{s_{NN}}$ [114]. Multiple physical changes in the collisions are occuring simultaneously in this region.

Yet another change that occurs in this region is the rapid increase of v_2 around 2 to 7 GeV. In the region around 7.7 to 11.5 GeV, the slope of $v_2\left(\sqrt{s_{NN}}\right)$ begins to level off. A possibility is that the deviation of $R_{\rm side}$ for 7.7 and 11.5 GeV is related to the onset of flow induced space-momentum correlations. The E802 results at 4.8 and 5.4 GeV in the right column of Fig. 8.3 are qualitatively similar to the STAR 7.7 GeV results for $R_{\rm side}$, but considering the STAR $\langle dN_{\rm ch}/d\eta\rangle^{1/3}$ values are slightly underestimated the E802 results probably deviate slightly more relative to the higher energies than even the 7.7 GeV data. For $R_{\rm out}$, on the other hand, the E802 results are quite significantly larger than the STAR 7.7 GeV points. This could be consistent with the effects of flow. Transverse flow should reduce the size of the regions of homogeneity and is expected to affect $R_{\rm out}$ much more than $R_{\rm side}$. This was reflected already in the larger slope for the $\langle m_T\rangle$ dependence in Fig. 8.2. That the deviation of the multiplicity dependence of $R_{\rm side}$ from the trends at higher energies is much smaller than $R_{\rm out}$ may be an indication of the relative degree to which the transverse radii are affected by flow. It would be interesting to study these trends at lower energies with a single detector where many interesting physical changes are occuring simultaneously.

An alternative explanation of the minimum observed in the volume measurement in Fig. 8.3 is provided by Ultra-relativistic Quantum Molecular Dynamics (UrQMD) calculations. In [115], UrQMD also finds a minimum between AGS and SPS energies but, in this case, the cause is related to a different type of change in the particle production mechanism. At the lowest energies pions are produced by resonances, but as the energy increases more pions are produced by color string fragmentation (accounting for color degrees of freedom) which freeze-out at an earlier, smaller stage (thus a smaller volume is measured) [115]. At even higher energies, the large increase in pion yields cause the volume to increase once more [115]. This explanation suggests that a change from hadronic to partonic degrees of freedom cause the minimum in the volume measurement [115]. Allowing a mean field potential to act on these pre-formed hadrons (the color string fragments) leads UrQMD to predict $R_{\rm out}/R_{\rm side}$ values near the observed values (≈ 1) for the whole energy range from AGS to SPS [116]. Simultaneously, inclusion of the mean field for pre-formed hadrons causes UrQMD to reproduce the net proton rapidity distribution and slightly improves its prediction for $v_2(p_T)$ at intermediate p_T [116].

As one last application of the data, the lifetime of the collisions is extracted in a study analogous to [103]. We also assume a kinetic freeze-out temperature, $T = 0.12$ GeV and fit the data in Fig. 8.2 using Eq. 8.1. The results are plotted in Fig. 8.5. The STAR results are all for 0-5% collisions with $\langle k_T \rangle \approx 0.22$ GeV/c. Again, there are some variations in the centrality ranges, as in Fig. 8.1, for the historical data. The lifetime appears to increase from around 4.5 fm/c at the lowest energies to around 7.5 fm/c at 200 GeV. Again, the ALICE point suggests a much longer lived, system significantly above the trend observed at lower energies. Consistent with [103], varying

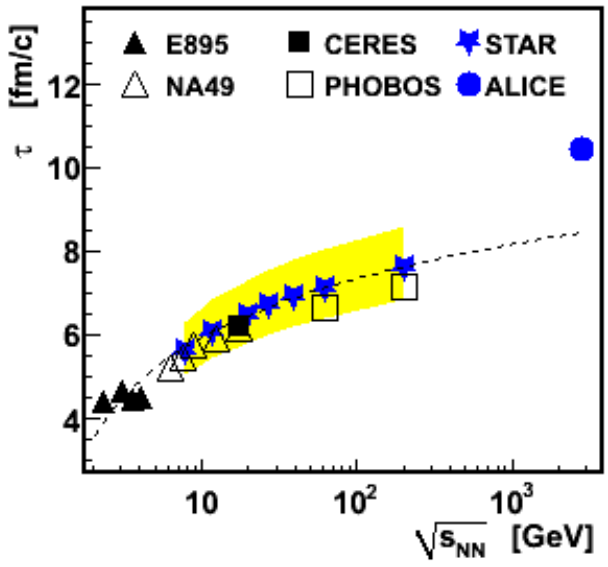

Figure 8.5: The lifetime, τ, of the system as a function of beam energy for central Au+Au collisions assuming a temperature of $T = 0.12$ GeV at kinetic freeze-out. The yellow band demonstrates the effect on τ of varying the assumed temperature by ± 0.02 GeV. Statistical uncertainties from the fits are smaller than the data points. To guide the eye, the dashed line extrapolates the trend observed at STAR to higher and lower energy. The text contains some discussion about variations in centrality and analysis techniques between different experiments.

the temperature assumed in the fits to $T = 0.10$ and $T = 0.14$ GeV causes the lifetimes to increase by 13% and decrease by 10%, respectively, for all energies. As noted in [103], due to affects from non-zero transverse flow and chemical potential for pions, the use of Eq. 8.1 may significantly underestimate the actual lifetimes.

8.2 Azimuthally differential HBT

The results of the azimuthally differential analysis are presented in two sets of seven figures corresponding to the seven energies. The first set, Fig. 8.6 through Fig. 8.12, compare mid-rapidity results obtained with the standard fit method to

those obtained with the global fit method. The second set, Fig. 8.13 through Fig. 8.19 compares forward, backward and mid-rapidity results obtained using the global fit method. The results for the freeze-out eccentricity can be found in the last section of this chapter. Earlier, Fig. 6.3 presented an example of the second order oscillations of the HBT radii relative to the event plane for a single energy, centrality, and rapidity. These second order oscillations are represented by 0^{th}- and 2^{nd}-order Fourier coefficients. Sec. 6.5 described these Fourier coefficients and how they can be used to compute the freeze-out eccentricity. In Figs. 8.6 through 8.19 the Fourier coefficients are presented as a function of N_{part}. Each set of Fourier coefficients for a given N_{part} (centrality), rapidity, and energy encodes all the information for oscillations similar to those in Fig. 6.3.

In each of the figures showing the Fourier coefficients, the 0^{th}-order coefficients are presented in the middle column, for the squared radii in the out, side and long directions ($R^2_{o,0}$, $R^2_{s,0}$, $R^2_{l,0}$) and the out-side cross term ($R^2_{os,0}$). These values are expected to correspond to radii from the azimuthally integrated analysis. This correspondence is demonstrated in the first Fourier coefficient figure for each energy which also includes the azimuthally integrated results (red crosses) for direct comparison. As in the azimuthally integrated case, the diagonal radii increase with centrality while the $R^2_{os,0}$ cross term remains about zero for all centralities. In the right column of these figures, ratios of 2^{nd}-order to 0^{th}-order coefficients are presented, also for the out, side, long and out-side parameters. The ratios that are presented have been connected to the freeze-out geometry, especially for the $R^2_{s,2}/R^2_{s,0}$ case. The left column of each of

the figures contains the parameters for the out-long cross term. The 0^{th}-order values, $R^2_{ol,0}$, are non-zero away from mid-rapidity and show interesting dependence on energy and centrality that will be discussed later.

8.2.1 Comparison of fit methods

The results using the two fit methods are generally consistent for most of the parameters. For each energy, the first figure compares the Fourier coefficients from the two fit methods at mid-rapidity. Forward and backward rapidity results are not included as some of the results become unreliable in a few cases. The reason is that at the lowest energies statistics limits the reliability, especially for the standard fit method, and especially for 7.7 GeV which has the fewest events and the lowest multiplicity per event. The forward and backward rapidity regions have even lower statistics due to the more narrow range of rapidity, $\Delta y = 0.5$ rather than $\Delta y = 1$. The event plane resolutions are much lower at these energies as well which can amplify noise in the correlation function when the correction algorithm is applied. The correction algorithm does not distinguish between a real signal and a statistical variation. The amplitude is increased in either case. The global fit method was designed to minimize this problem by only applying the correction algorithm to the denominator which has an order of magnitude higher statistics than the numerator.

The 0^{th}-order Fourier coefficients are expected to be consistent with the radii in the azimuthally integrated analysis. Therefore, the 0^{th}-order, squared radii should increase smoothly with N_{part} (as in the middle column of Figs. 8.6 through 8.19). For the 0^{th}-order terms good agreement with the azimuthally integrated results was observed for both the standard and global fit methods, except a few cases at the lowest

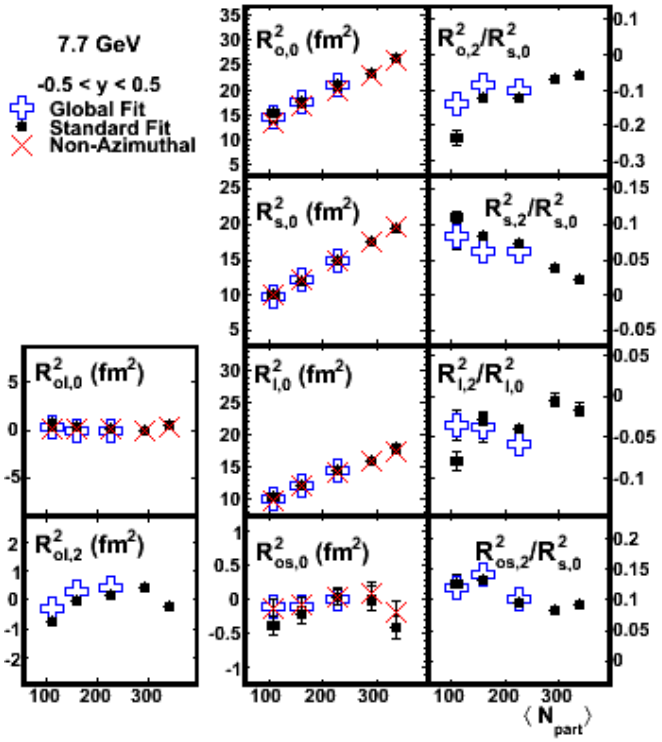

Figure 8.6: Centrality dependence of the Fourier coefficients that describe azimuthal oscillations of the HBT radii, at mid-rapidity ($-0.5 < y < 0.5$), in 7.7 GeV with $\langle k_T \rangle \approx 0.31$ GeV/c. Solid circles are results using separate "standard" Gaussian fits to each angular bin. Open symbols represent results using a single global fit to all angular bins to directly extract the Fourier coefficients. Red crosses demonstrate good agreement between the azimuthally integrated radii and the 0^{th}-order Fourier coefficients. As described in the text, the 0-5% and 5-10% global fit points have been excluded.

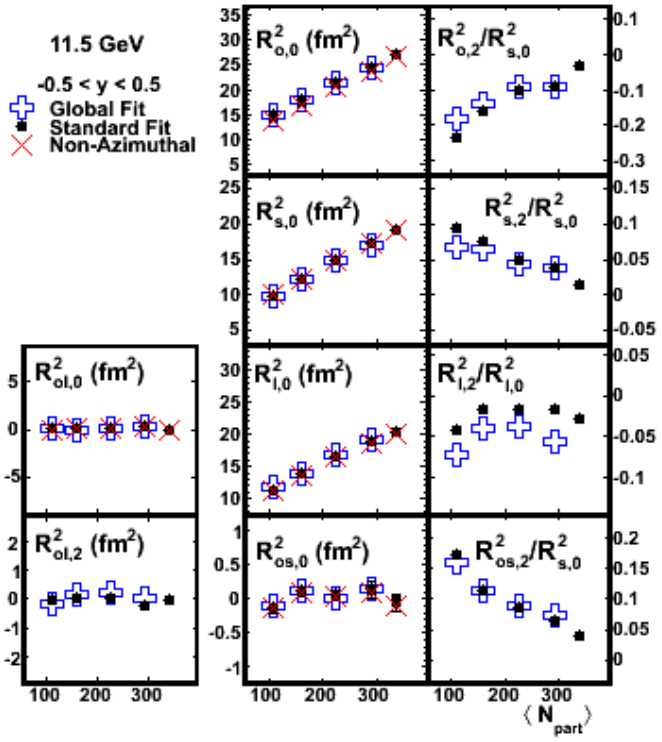

Figure 8.7: Centrality dependence of the Fourier coefficients that describe azimuthal oscillations of the HBT radii, at mid-rapidity ($-0.5 < y < 0.5$), in 11.5 GeV collisions with $\langle k_T \rangle \approx 0.31$ GeV/c. Solid circles are results using separate "standard" Gaussian fits to each angular bin. Open symbols represent results using a single global fit to all angular bins to directly extract the Fourier coefficients. Red crosses demonstrate good agreement between the azimuthally integrated radii and the 0^{th}-order Fourier coefficients. The 0-5% global fit point is excluded.

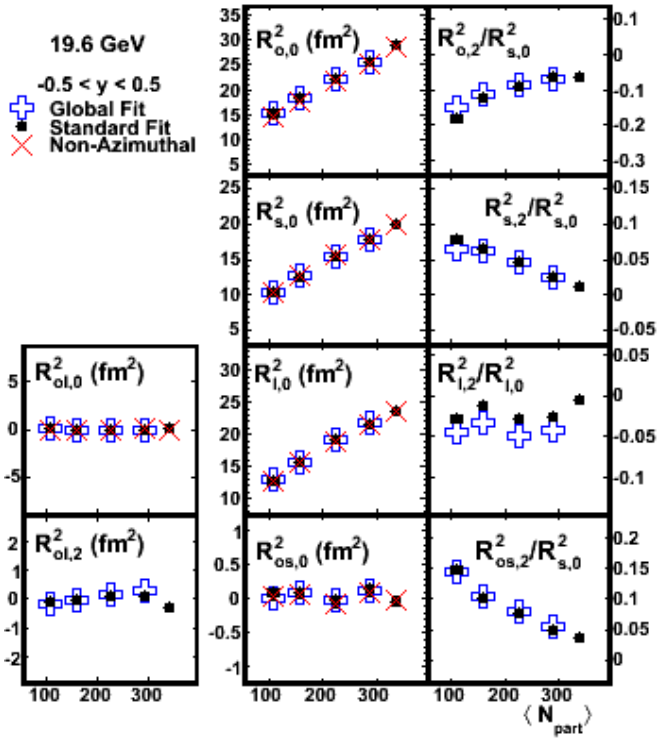

Figure 8.8: Centrality dependence of the Fourier coefficients that describe azimuthal oscillations of the HBT radii, at mid-rapidity ($-0.5 < y < 0.5$), in 19.6 GeV collisions with $\langle k_T \rangle \approx 0.31$ GeV/c. Solid circles are results using separate "standard" Gaussian fits to each angular bin. Open symbols represent results using a single global fit to all angular bins to directly extract the Fourier coefficients. Red crosses demonstrate good agreement between the azimuthally integrated radii and the 0^{th}-order Fourier coefficients. As described in the text, the 0-5% global fit method point is excluded.

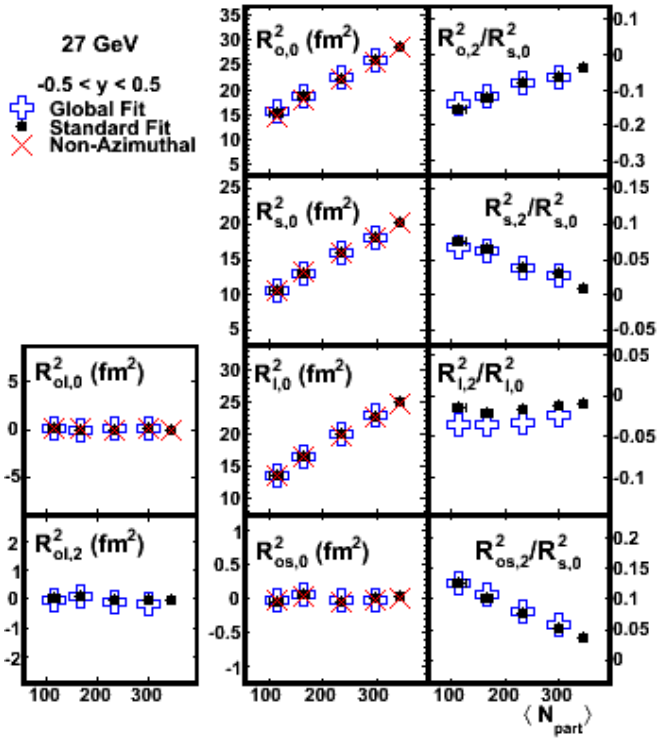

Figure 8.9: Centrality dependence of the Fourier coefficients that describe azimuthal oscillations of the HBT radii, at mid-rapidity ($-0.5 < y < 0.5$), in 27 GeV collisions with $\langle k_T \rangle \approx 0.31$ GeV/c. Solid circles are results using separate "standard" Gaussian fits to each angular bin. Open symbols represent results using a single global fit to all angular bins to directly extract the Fourier coefficients. Red crosses demonstrate good agreement between the azimuthally integrated radii and the 0^{th}-order Fourier coefficients. As described in the text, the 0-5% global fit method point is excluded.

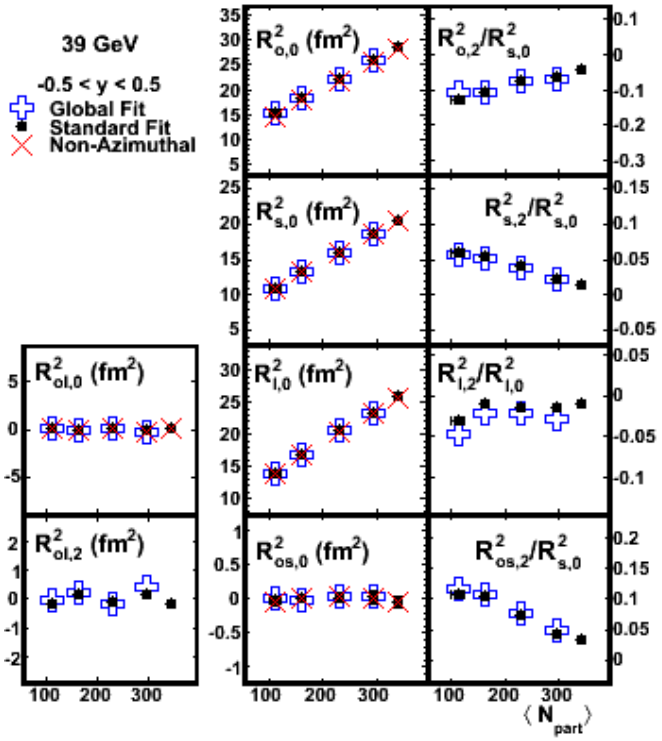

Figure 8.10: Centrality dependence of the Fourier coefficients that describe azimuthal oscillations of the HBT radii, at mid-rapidity ($-0.5 < y < 0.5$), in 39 GeV collisions with $\langle k_T \rangle \approx 0.31$ GeV/c. Solid circles are results using separate "standard" Gaussian fits to each angular bin. Open symbols represent results using a single global fit to all angular bins to directly extract the Fourier coefficients. Red crosses demonstrate good agreement between the azimuthally integrated radii and the 0^{th}-order Fourier coefficients. As described in the text, the 0-5% global fit method point is excluded.

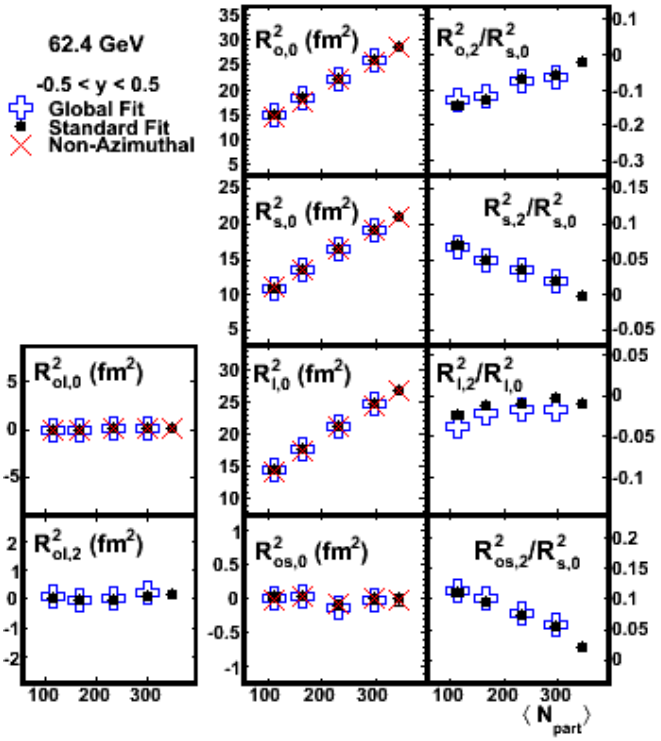

Figure 8.11: Centrality dependence of the Fourier coefficients that describe azimuthal oscillations of the HBT radii, at mid-rapidity ($-0.5 < y < 0.5$), in 62.4 GeV collisions with $\langle k_T \rangle \approx 0.31$ GeV/c. Solid circles are results using separate "standard" Gaussian fits to each angular bin. Open symbols represent results using a single global fit to all angular bins to directly extract the Fourier coefficients. Red crosses demonstrate good agreement between the azimuthally integrated radii and the 0^{th}-order Fourier coefficients. As described in the text, the 0-5% global fit method point is excluded.

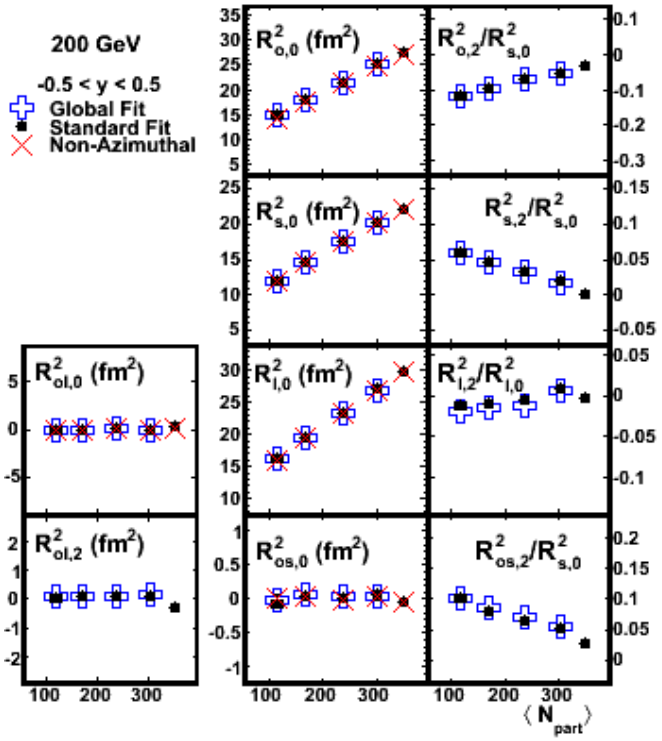

Figure 8.12: Centrality dependence of the Fourier coefficients that describe azimuthal oscillations of the HBT radii, at mid-rapidity ($-0.5 < y < 0.5$), in 200 GeV collisions with $\langle k_T \rangle \approx 0.31$ GeV/c. Solid circles are results using separate "standard" Gaussian fits to each angular bin. Open symbols represent results using a single global fit to all angular bins to directly extract the Fourier coefficients. Red crosses demonstrate good agreement between the azimuthally integrated radii and the 0^{th}-order Fourier coefficients. As described in the text, the 0-5% global fit method point is excluded.

energies. Especially for 7.7 GeV, with the standard fit method, several points, primarily the most peripheral and more central (lowest statistics and resolution) points, deviate quite significantly from this trend. In the same cases, the global fit method remains consistent with the non-azimuthal radii. Projections of the fits show the standard fit method results do not match well with the data in such cases. In particular, the 90° bin suffers most from low statistics (fewer tracks are directed out of the reaction plane) which affects both the 0^{th}- and 2^{nd}-order coefficients when each bin is fit separately. The global fit method results appear to be somewhat more reliable in these low statistics and low resolution cases.

As noted earlier, there is a difference in the oscillation amplitude for the long direction, $R^2_{l,2}$, obtained from the two methods. This is shown clearly in Fig. 6.3 where the global fit method extracts a larger oscillation amplitude. From the first Fourier coefficient figure at each energy, the ratio $R^2_{l,2}/R^2_{l,0}$ is systematically further below zero for the global fit method results. This is a systematic difference, independent of centrality and energy, related to the different parameterizations in the two fit methods.

Earlier in Sec. 6.7, the global fit method was found to have difficulties fitting the most central 0-5% data as well as a few 5-10% cases for 7.7 and 11.5 GeV where the statistics are low. This was attributed to the similarity of the distributions for all the angular bins in the more central data and the parameterization used in the global fit method where the dependence of χ^2 on the value of $R^2_{ol,2}$ becomes quite flat for the central bin. These points have been excluded from the figures as this seems to be the limit of reliability. Still, in all cases, the fit projections from the global fit method better match the data, there is better agreement between forward and

backward as well as mid-rapidity results and, as discussed in Sec. 6.7, the errors are not underestimated as they are for the standard fit method. Therefore, results using the global fit method are used later when discussing the freeze-out shape.

8.2.2 Discussion of Fourier components

The trends exhibited by the Fourier coefficients are qualitatively similar for all energies. The 0^{th}-order coefficients are consistent with the non-azimuthal results. Like in the non-azimuthal results, the increase of the 0^{th}-order coefficients for more central data is related to the increasing volume of the homogeneity regions in more central events. Since the ratios of 2^{nd}- to 0^{th}-order results are related to the freeze-out shape, the trends are expected to extrapolate toward zero for more central, more round collisions. The right column of the Fourier coefficient figures for each energy demonstrate that this behavior is observed. For each HBT radius, the ratios of 2^{nd}- to 0^{th}-order coefficients follow similar trends for all energies, rapidities, and centralities. This means that the 2^{nd}-order coefficients (half the oscillation amplitudes) have the same sign in all these cases. Therefore, the data requires that all energies, rapidities, and centralities must exhibit oscillations of the HBT radii that are qualitatively similar to those in Fig. 6.3. The Fourier coefficients for all three rapidities are quite similar in most cases, especially in the $R^2_{s,2}/R^2_{s,0}$ values for 10-20% and 20-30% centralities used later in the excitation function for the freeze-out eccentricity.

One interesting feature occurs in the $R^2_{ol,0}$ parameter at forward and backward rapidity. This parameter exhibits both centrality and energy dependence that may be relevant for constraining future model studies. The centrality dependence is shown in the upper panels in the left column of Figs. 8.13, 8.14, 8.15, 8.16, 8.17, 8.18, and

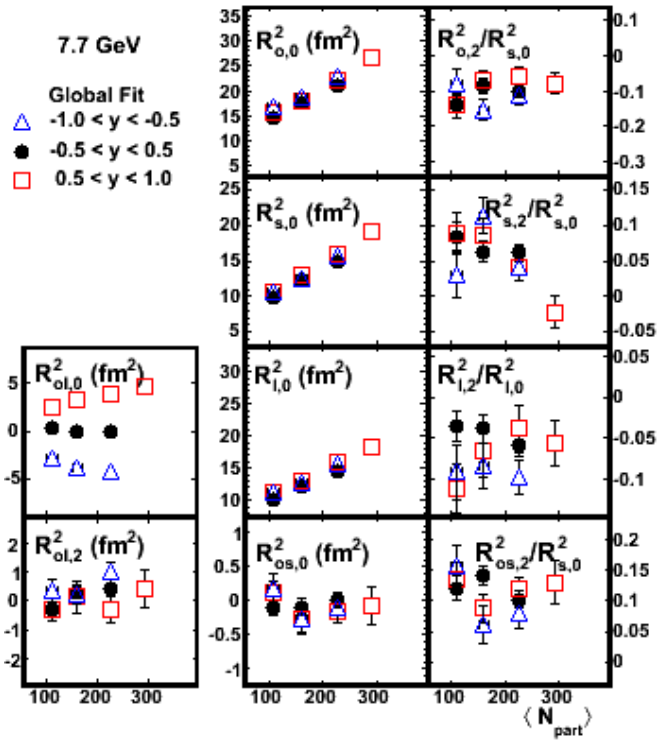

Figure 8.13: Centrality dependence of the Fourier coefficients that describe azimuthal oscillations of the HBT radii, at backward ($-1 < y < -0.5$), forward ($0.5 < y < 1$) and mid ($-0.5 < y < 0.5$) rapidity, in 7.7 GeV collisions with $\langle k_T \rangle \approx 0.31$ GeV/c using the global fit method. As described in the text, the 0-5% and two 5-10% points have been excluded.

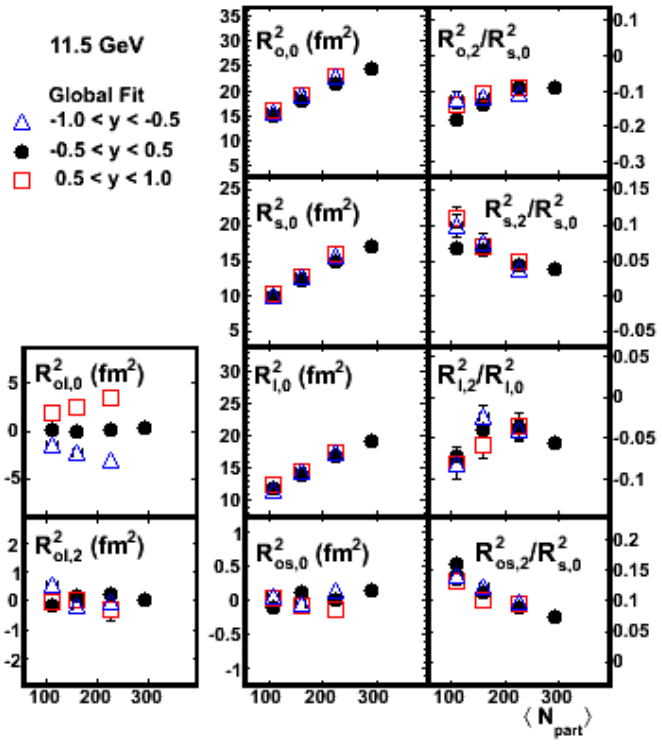

Figure 8.14: Centrality dependence of the Fourier coefficients that describe azimuthal oscillations of the HBT radii, at backward ($-1 < y < -0.5$), forward ($0.5 < y < 1$) and mid ($-0.5 < y < 0.5$) rapidity, in 11.5 GeV collisions with $\langle k_T \rangle \approx 0.31$ GeV/c using the global fit method. As described in the text, the 0-5% and two 5-10% points have been excluded.

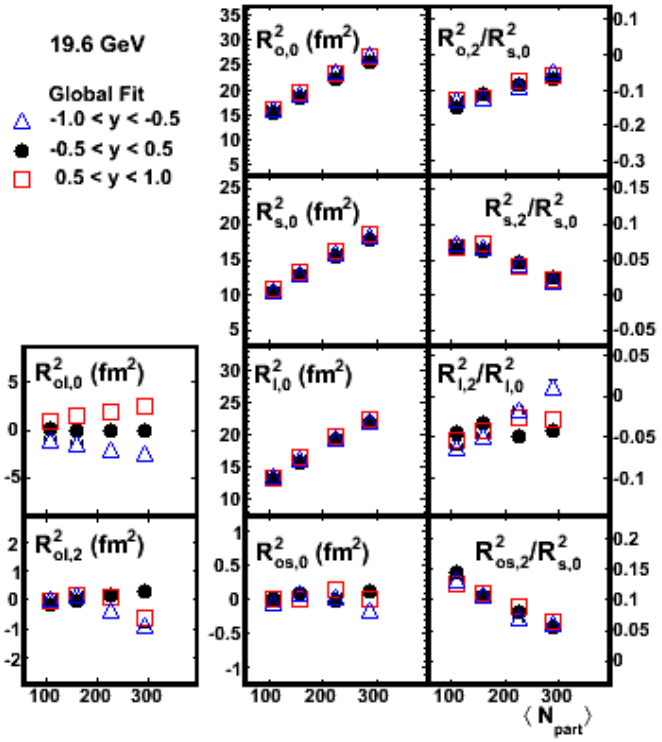

Figure 8.15: Centrality dependence of the Fourier coefficients that describe azimuthal oscillations of the HBT radii, at backward ($-1 < y < -0.5$), forward ($0.5 < y < 1$) and mid ($-0.5 < y < 0.5$) rapidity, in 19.6 GeV collisions with $\langle k_T \rangle \approx 0.31$ GeV/c using the global fit method.

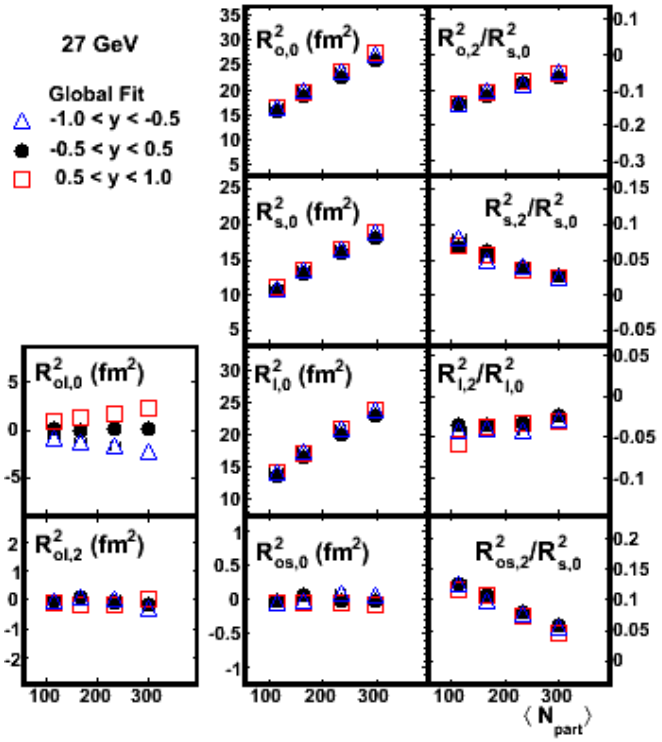

Figure 8.16: Centrality dependence of the Fourier coefficients that describe azimuthal oscillations of the HBT radii, at backward ($-1 < y < -0.5$), forward ($0.5 < y < 1$) and mid ($-0.5 < y < 0.5$) rapidity, in 27 GeV collisions with $\langle k_T \rangle \approx 0.31$ GeV/c using the global fit method.

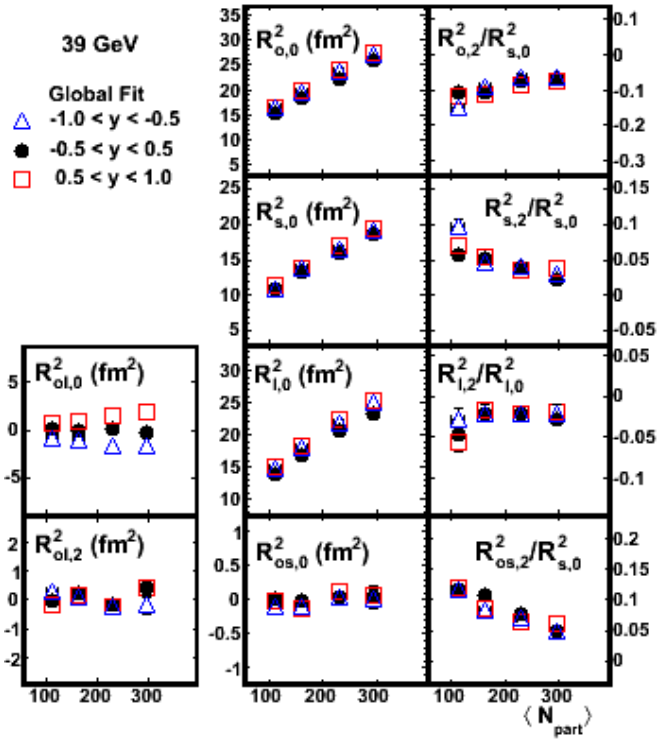

Figure 8.17: Centrality dependence of the Fourier coefficients that describe azimuthal oscillations of the HBT radii, at backward ($-1 < y < -0.5$), forward ($0.5 < y < 1$) and mid ($-0.5 < y < 0.5$) rapidity, in 39 GeV collisions with $\langle k_T \rangle \approx 0.31$ GeV/c using the global fit method.

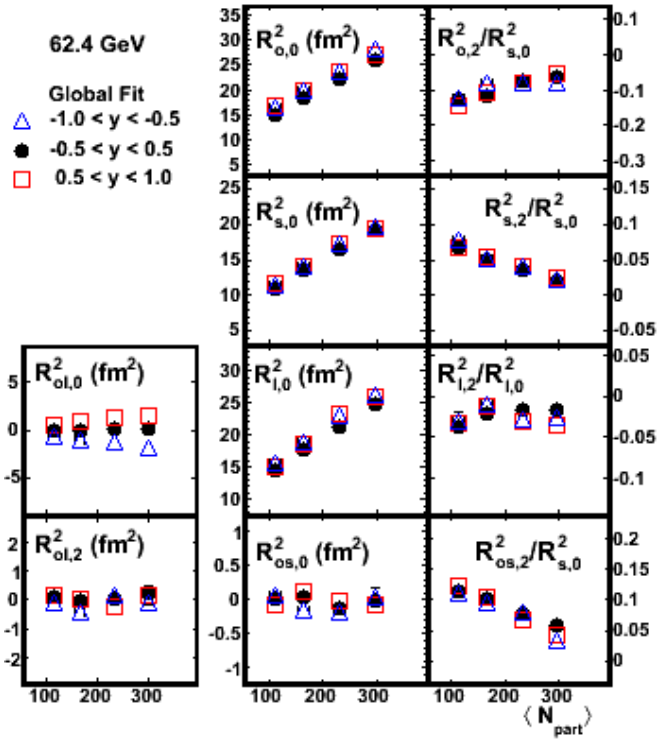

Figure 8.18: Centrality dependence of the Fourier coefficients that describe azimuthal oscillations of the HBT radii, at backward ($-1 < y < -0.5$), forward ($0.5 < y < 1$) and mid ($-0.5 < y < 0.5$) rapidity, in 62.4 GeV collisions with $\langle k_T \rangle \approx 0.31$ GeV/c using the global fit method.

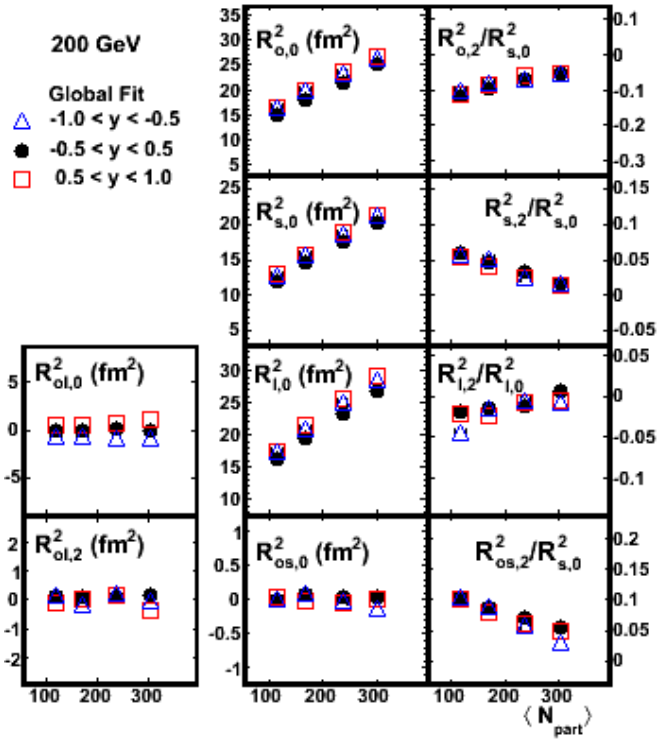

Figure 8.19: Centrality dependence of the Fourier coefficients that describe azimuthal oscillations of the HBT radii, at backward ($-1 < y < -0.5$), forward ($0.5 < y < 1$) and mid ($-0.5 < y < 0.5$) rapidity, in 200 GeV collisions with $\langle k_T \rangle \approx 0.31$ GeV/c using the global fit method.

8.19. As discussed earlier, this term averages to zero for results centered at mid-rapidity, but is otherwise non-zero. At the lowest energy, the $R^2_{ol,0}$ offset is quite large (Fig. 8.13) and increases in a linear manner with $N_{\rm part}$. At higher energies, although the linear trend with $N_{\rm part}$ remains, the slope decreases for larger $\sqrt{s_{NN}}$. For the 200 GeV results (Fig. 8.19), the slope and values are quite small. As discussed in Sec. 6.2, this non-zero cross term corresponds to a tilt in the $q_{\rm out}$-$q_{\rm long}$ plane. The non-zero value of the crossterm means there is a correlation between the relative momentum of particle pairs in the out and long directions. Two considerations affect how $R^2_{ol,0}$ (or any of the radii) are related to physical parameters of interest. One is the frame in which the correlation function is constructed (fixed center of mass, LCMS, etc.) [83, 84]. The other involves the assumptions that enter a particular analytical model of the source distribution (static, longitudinal flow, transverse flow, boost-invariance, etc.) that is required to relate the extracted fit parameters (radii) to physical quantities such as freeze-out duration or total lifetime [83, 84].

Assume for the moment that radii are measured in the LCMS frame, as in this analysis. In models with longitudinal expansion, breaking of boost-invariance results in non-zero values of the $R^2_{ol,0}$ cross term away from mid-rapidity [83, 84]. The reason is that the LCMS and local rest frame of the source only coincide in the boost-invariant model [84]. This is one example of how changing the model assumptions leads to a different relationship between the radii (including $R^2_{ol,0}$) and physical parameters.

Alternatively, if the same analytical model is assumed but the measurement is performed in different frames, the dependence of the radii on physical parameters will also change. For instance, in a model with boost-invariant longitudinal expansion, [84] demonstrates that measurement in a fixed frame, the LCMS frame, and a

generalized Yano-Koonin frame lead to three different relationships between the fit parameters (radii) and physical quantities. In [83], a similar analytical model leads to a quite complex dependence of $R^2_{ol,0}$ on various physical quantities in the center of mass frame. However, the expression greatly simplifies in the LCMS frame, leaving $R^2_{ol,0}$ directly proportional to the freeze-out duration and other parameters.

Fig. 8.20 shows that for each centrality $R^2_{ol,0}$ decreases smoothly toward zero at higher energies. It has been suggested [83, 84] that the quantity $R^2_{\rm out} - R^2_{\rm side}$ should be sensitive to the duration of particle emission, $\Delta\tau$, which is why the quantity $R_{\rm out}/R_{\rm side}$ has been studied in the past, as in Fig. 8.1. The R^2_{ol} offset has also been associated with the duration of freeze-out and other parameters in a functionally different way [83, 84]. Although it cannot be determined from the data alone, this new data may allow an estimate of $\Delta\tau$ (or other quantities) as a function of beam energy, using a variable that has different dependence on $\Delta\tau$ than does the more commonly studied quantity $R^2_{\rm out} - R^2_{\rm side}$.

One other observation can be made because the $R^2_{ol,0}$ values in Fig. 8.20 are measured in the LCMS frame. As mentioned above, non-zero values of this parameter suggest boost-invariance may be broken. That $R^2_{ol,0}$ becomes more non-zero at lower $\sqrt{s_{NN}}$ may thus reflect how assumption of boost-invariance becomes less valid at lower energies.

Assume for the moment that radii are measured in the LCMS frame, as in this analysis. In models with longitudinal expansion, breaking of boost-invariance results in non-zero values of the $R^2_{ol,0}$ cross term away from mid-rapidity [83, 84]. The reason is that the LCMS and local rest frame of the source only coincide in the boost-invariant

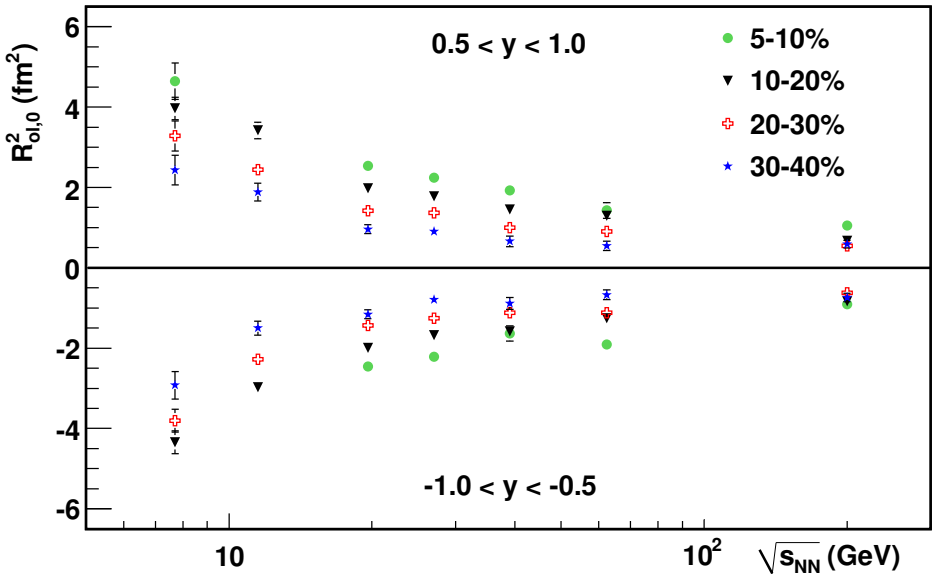

Figure 8.20: Beam energy dependence of the $R^2_{ol,0}$ cross term for forward and backward rapidity with $\langle k_T \rangle \approx 0.31$ GeV/c.

model [84]. This is one example of how changing the model assumptions leads to a different relationship between the radii (including $R^2_{ol,0}$) and physical parameters.

Alternatively, if the same analytical model is assumed but the measurement is performed in different frames the dependence of the radii on physical parameters will also change. For instance, in a model with boost-invariant longitudinal expansion, [84] demonstrates that measurement in a fixed frame, the LCMS frame, and a generalized Yano-Koonin frame lead to three different relationships between the fit parameters (radii) and physical quantities. In [83], a similar analytical model leads to a quite complex dependence of $R^2_{ol,0}$ on various physical quantities in the center of mass frame. However, the expression greatly simplifies in the LCMS frame leaving $R^2_{ol,0}$ directly proportional to the freeze-out duration and other parameters.

Fig. 8.20 shows that for each centrality $R^2_{ol,0}$ decreases smoothly toward zero at higher energies. It has been suggested [83, 84] that the quantity $R^2_{\rm out} - R^2_{\rm side}$ should be sensitive to the duration of particle emission, $\Delta\tau$, which is why the quantity $R_{\rm out}/R_{\rm side}$ has been studied in the past, as in Fig. 8.1. The R^2_{ol} offset has also been associated with the duration of freeze-out and other parameters in a functionally different way [83, 84]. Although it cannot be determined from the data alone, this new data may allow an estimate of $\Delta\tau$ (or other quantities) as a function of beam energy, using a variable that has different dependence on $\Delta\tau$ than does the more commonly studied quantity $R^2_{\rm out} - R^2_{\rm side}$.

One other observation can be made because the $R^2_{ol,0}$ values in Fig. 8.20 are measured in the LCMS frame. As mentioned above, non-zero values of this parameter suggest boost-invariance may be broken. That $R^2_{ol,0}$ becomes more non-zero at lower $\sqrt{s_{NN}}$ may thus reflect how assumption of boost-invariance becomes less valid at lower energies.

8.2.3 Discussion of the freeze-out eccentricity

Figure 8.21 shows the eccentricities at kinetic freeze-out, ε_F, defined in Eq. 6.9 for all centralities and energies. They are plotted against the initial eccentricity relative to the participant plane, defined as

$$\varepsilon_{PP} = \frac{\sqrt{(\sigma_y^2 - \sigma_x^2)^2 + 4\sigma_{xy}^2}}{\sigma_x^2 + \sigma_y^2}. \tag{8.3}$$

The quanitities $\sigma_x^2 = \{x^2\} - \{x\}^2$ and $\sigma_y^2 = \{y^2\} - \{y\}^2$ gauge the widths of the distributions of participant nucleons in and out of the reaction plane direction, respectively. The symbol $\{\ldots\}$ denotes averaging over the position of participant nucleons in each

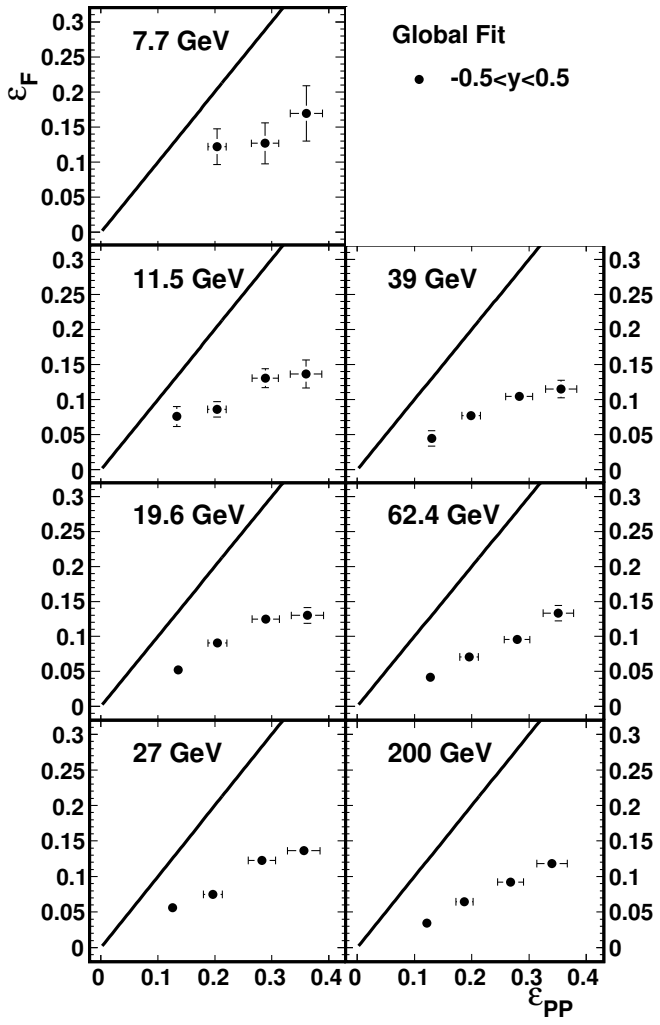

Figure 8.21: The eccentricity of the collisions at kinetic freeze-out, ε_F, as a function of initial eccentricity relative to the participant plane, ε_{PP}, at mid-rapidity. All results are for $\langle k_T \rangle \approx 0.31$ GeV/c. The line has a slope of one indicating no change in shape. Points further below the line evolve more to a round shape.

event for many events. The quantity $\sigma_{xy} = \{xy\} - \{x\}\{y\}$ accounts for event-by-event fluctuations in the distribution of participant nucleons. The values of ε_{PP} on the horizontal axes of Fig. 8.21 were determined with Monte Carlo Glauber simulations for each energy and centrality as described in [117]. The line has a slope of one ($\varepsilon_F = \varepsilon_{PP}$) so points further below the line have evolved more toward a round shape ($\varepsilon_F = 0$). These results demonstrate that, at all energies and rapidities studied, the freeze-out shape remains an out-of-plane extended ellipse ($\varepsilon_F > 0$). In no case does extended lifetime or stronger flow result in the shape becoming in-plane extended ($\varepsilon_F < 0$). However, there is always some evolution toward a more round shape, as expected, and there tends to be slightly more evolution for the higher energies. The same observations apply at forward and backward rapidity because of the similar trends observed for the ratio $R^2_{s,2}/R^2_{s,0}$ ($= \varepsilon_F/2$).

The excitation function for the freeze-out shape is presented in Figure 8.22. The new STAR results for three rapidities are compared to earlier measurements from other experiments and to several models. The results use the global fit method and are for mid-peripheral (10-30%) collisions where the initial anisotropic shape is large but there is still significant overlap of the nuclei. The larger differences between in-plane and out-of-plane pressure gradients in these collisions and larger initial spatial anisotropy could admit more varied results in the change in shape, if that where to happen at different energies. The new STAR results exhibit a monotonic decrease in the freeze-out eccentricity with beam energy for all three rapidity regions.

There are some differences in analyses from different experiments such as correction for event plane resolution, fitting in one k_T bin versus averaging several smaller k_T bins, and centrality ranges. These could potentially be important and were studied.

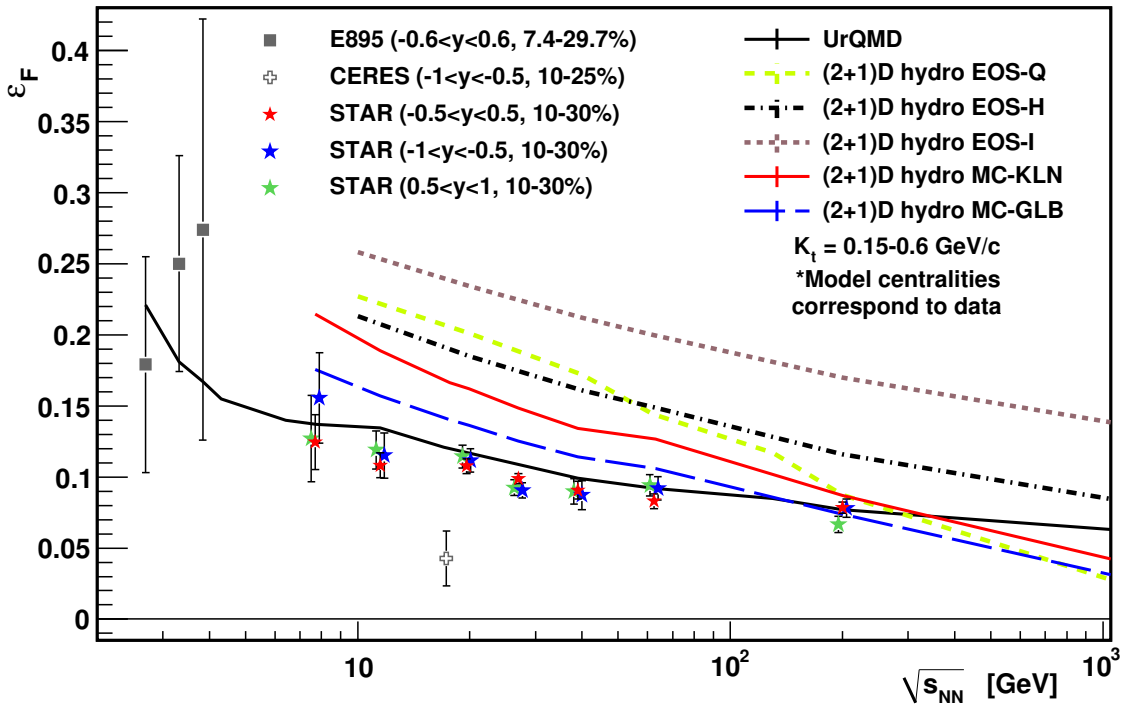

Figure 8.22: The freeze-out eccentricity dependence on beam energy in mid-central Au+Au or Pb+Pb collisions for three rapidity regions and with $\langle k_T \rangle \approx 0.31$ GeV/c. For clarity, the points for forward and backward rapidity from STAR are offset slightly. The models are from UrQMD as well as several (2+1)D hydrodynamical models. The trend is consistent with a monotonic decrease in eccentricity with beam energy.

The CERES point at 17.3 GeV suggested a possible minimum in the historical data. The new STAR results at 11.5 and 19.6 GeV at mid-rapidity were significantly higher suggesting a monotonic decrease in the freeze-out shape. To check that the difference was not due to the different rapidity windows the STAR analysis was extended to include the same rapidity region as CERES, $0.5 < |y| < 1$. The forward and backward rapidity results remained consistent with the mid-rapidity measurement. The CERES point for 10-25% centrality is consistent with 0-10% central STAR results at 19.6 GeV and it seems rather unlikely that differences in centrality definitions could be a cause of the difference. Event, track, and pair selection quantities have rather little effect on the results. Another difference is the range of k_T values included in the fits. In the CERES and earlier STAR result [17], the azimuthal analysis was done in narrow k_T bins and the ε_F values averaged. This was problematic at the lowest energies due to lower statistics when the analysis was additionally differential in k_T. Using a single, wide k_T bin biases the results slightly toward smaller ε_F values, as discussed in Sec.2.3. Therefore, to be consistent, the same (wide k_T bin) method is used for all the STAR points. The CERES results used a weighted average of results in narrow k_T bins which should be equivalent to using a single, wide k_T bin. It seems unlikely that this is the cause of the discrepency. The "v_2-type" correction algorithm was used in the CERES and E895 cases to correct for the event plane resolution while in the STAR case the histograms were corrected or the fit function smeared in the global fit case. The difference in the results is rather tiny for these different methods and cannot explain the difference.

As discussed in Sec. 7.3.3, non-monotonic behavior in the excitation function would have strongly suggested interesting changes in the equation of state. The

observed monotonic decrease excludes the scenario described in reference [8] and is consistent with increased lifetime and/or pressure gradients at higher energy. The energy dependence of $R_{\rm long}$ from the non-azimuthal analysis, and the lifetimes shown in Fig. 8.5, suggest also that the system is longer-lived at higher energy. Still, these results will allow to probe equation of state effects by comparing to various models.

The currently available model predictions for the energy dependence of the freeze-out eccentricity are also shown in Fig. 8.22. All models predict a monotonic decrease in the freeze-out shape at higher energies, so all models agree qualitatively with the data. The older (2+1)D, ideal hydrodynamical models [14], labeled EOS-H, EOS-I, and EOS-Q, all overpredict the data. As was noted in [118], in comparison to the historical data, the model with a first order phase transition, EOS-Q, gets close to the 200 GeV point. The predictions of the freeze-out shape are sensitive to the equation of state used in the hydrodynamic models. This is clear by comparing the curves for EOS-I (ideal, massless quark gluon gas) and EOS-H (hadronic gas). For EOS-Q, the slope changes, following EOS-H at low energies but dropping more rapidly at higher energies. This is attributed to passage through a mixed-phase regime which extends the lifetime allowing the system to evolve to a more round state at higher energies [8].

The two more recent (2+1)D predictions, from the VISH2+1 model, get closer to the data. MC-KLN and MC-GLB correspond to different initial conditions and are somewhat more realistic than the earlier results as they allow to incorporate viscous effects. MC-GLB uses a specific shear viscosity of $\eta/s = 0.08$ with Glauber initial conditions [118]. The MC-KLN model has a much larger viscosity $\eta/s = 0.2$ and the initial shape is derived from the initial gluon density distribution in the transverse

plane (which is converted to an entropy and finally energy density profile) [118]. Both models incorporate an equation of state based on lattice QCD, named s95p-PCE [119, 120]. Initial parameters in the models were calibrated using measured multiplicity distributions (and extrapolations to lower energies) and to describe p_T-spectra and v_2 measurements for 200 GeV Au+Au collisions at RHIC [118]. The two cases were found to yield similar lifetimes but in the MC-KLN case the initial eccentricities are larger (more out-of-plane extended). The MC-KLN model achieves a less round shape simply because it starts with larger initial eccentricity [118]. The excitation function for freeze-out eccentricities has the potential to resolve ambiguities between models with different initial conditions and values of η/s. In particular, the two sets of initial conditions and η/s yield identical v_2, but very different ε_F. So the results in Fig. 8.22 provide tighter constraints on these models.

The goal of [118] was to map systematic trends in observables with the two models, not to explain the data precisely. In fact the applicability of these models is known to be problematic at lower energies both because they assume boost-invariance which is broken at lower energy and because the hadronic phase is expected to become more important at lower energy. To avoid these difficulties requires (3+1)D viscous hydrodynamics. Nevertheless, the new results are able to match more closely the experimemental results. Of the hydrodynamical models, MC-GLB is closest to the data although it still overpredicts the freeze-out eccentricity and the slope appears too steep. One relevant observation from [118] is that in these models the decrease in the eccentricity with energy appears to be due mainly to an extended lifetime rather than larger anistropy of pressure gradients. As discussed earlier, the lifetime extracted from $R_{\rm long}$ values also suggest an increase in the total lifetime. However, the data

cannot allow one to determine whether the decrease in eccentricity is due solely to increased lifetime or whether the pressure gradients may also play a significant role.

The prediction of the Boltzmann transport model, UrQMD (v2.3) [121], matches most closely the freeze-out shape at all energies. UrQMD follows the trajectories and interactions of all hadronic particles throughout the collision so it does not require assumptions about how freeze-out occurs. The model is 3D and does not require boost-invariance and so is equally applicable at all the studied energies. This may be at least partially, why the predictions from UrQMD more closely match the energy dependence compared to the hydrodynamic predictions. While it does not explicitly contain a deconfined state, it does incorporate color degrees of freedom through inclusion of the creation of color strings and their subsequent decay back into hadrons.

For the azimuthally integrated results, UrQMD does rather well at predicting the observed dependence of HBT radii on $\langle k_T \rangle$ and centrality [122, 123]. As discussed earlier, inclusion of a mean field acting between pre-formed hadrons (color string fragments) predicts $R_{\rm out}/R_{\rm side}$ ratios similar to the observed values and leads naturally to a minimum in the volume similar to that which is observed experimentally [115, 116]. Such a repulsive potential between the string fragments would mimic somewhat an increase in pressure gradients at early stages [116] similar to the hydrodynamics cases with an equation of state that includes a phase transition. The UrQMD predictions for the eccentricities at kinetic freeze-out in Fig.8.22 were made with UrQMD in cascade mode and so do not incorporate this potential between string fragments.

It should be noted that none of the models is perfect and none predict all observables simultaneously. The UrQMD model, while it matches the freeze-out shapes well, matches the momentum space observables less well. And the hydrodynamic models,

while they are able to describe the momentum space p_T spectra and v_2 results, do less well at predicting the eccentricity and trends observed in HBT analyses. The availability of these new experimental results provide an important opportunity to further constrain models.

Chapter 9: Conclusions

This chapter summarizes the conclusions from the research presented in this thesis and are the same as those in Section VII in Reference [85], the paper corresponding to this thesis.

The results of HBT analyses have been measured using the STAR detector for Au+Au collisions from 7.7 GeV to 200 GeV. The dependence of the HBT radii on m_T, centrality, and energy have been observed to be similar to earlier measurements with other experiments. The comparison of results across this wide range of energies is greatly improved by eliminating differences between detectors, analysis techniques and binning in centrality and $\langle k_T \rangle$ that is present in the historical data. For instance, the beam energy dependence of the radii generally agree with results from different experiments but show a much smoother trend than the historical data and, additionally, contribute data in previously unexplored regions of collision energy. The transverse mass dependence is also consistent with earlier observations and, additionally, allows one to conclude all k_T and centrality bins will exhibit similar trends as a function of beam energy.

The energy dependence of the volume of the homogeneity regions is consistent with a constant mean free path at freeze-out as is the very flat energy dependence of $R_{\rm out}$. This scenario also explains the common dependence of $R_{\rm side}$ and $R_{\rm long}$ on the

cubed-root of the multiplicity that is observed at higher energy. For 7.7 and 11.5 GeV, R_{side} appears to deviate slightly from the trend at the higher energies. Two physical changes that may potentially be related to this are the effects of strangeness enhancement (not included in the argument for a constant mean free path at freeze-out) and the rapid increase in the strength of v_2 that levels off around 7.7 to 11.5 GeV. Both of these physical changes occur in the vicinity of the minimum. A systematic study with a single detector at slightly lower energies would be needed to help disentangle the different effects.

The UrQMD model provides an alternative explanation for the minimum in the volume measurement in terms of a change from a hadronic to a partonic state. Including interactions between color string fragments early in the collision, it not only can explain the minimum in the volume but is also able to find $R_{\text{out}}/R_{\text{side}}$ values close to one as observed from AGS through RHIC energies and improves the agreement between UrQMD and other observables at the same time. It is interesting that such an interaction potential may somewhat mimic an increase in the pressure gradients which may correlate with the observation that v_2 increases rapidly with $\sqrt{s_{NN}}$ in this region also.

The lifetime of the collision evolution was extracted using the $\langle m_T \rangle$ dependence of R_{long}. Subject to certain assumptions, the lifetime increases by roughly 1.7 times from AGS to 200 GeV collisions measured at STAR. The lifetime increases significantly more rapidly between RHIC and the LHC.

A new global fit method was developed and studied in relation to the standard fit method. While it has problems primarily in the most central bin, related to differences in the parameterization, for other centralities it yields more reliable results in cases

of low statistics and poor event plane resolution. Additionally, it avoids problems related to correlated errors. This has allowed to get the most reliable results at the lowest energies studied.

The Fourier coefficients measured away from mid-rapidity allow one to extract the previously unavailable monotonic decrease of the $R^2_{ol,0}$ cross term as a function of beam energy. This observable has been connected to the duration of particle emission in a way that is different than the more commonly studied quantities $R^2_{\rm out} - R^2_{\rm side}$ or $R_{\rm out}/R_{\rm side}$. Actually, the dependence of these two observables on physical quantities, including emission duration or lifetime, depend on specific assumptions [83, 84]. In particular, each of these two observables tend to relate to the other quantities differently. Considering the beam energy dependence of R^2_{ol} in conjunction with the various sets of assumptions explored in [83, 84], for instance, may lead to new insights, or even constraints on which assumptions are valid.

The azimuthally differential results show that, for all energies, the evolution of the collision eccentricity leaves the system still out-of-plane extended at freeze-out. In mid-central (10-30%) collisions, the freeze-out eccentricity shows a monotonic decrease with beam energy consistent with expectations of increased flow and/or increased lifetime at higher energies. This is supported by the azimuthally integrated results which suggest longer lifetimes at higher energies. The results are consistent qualitatively with all model predictions and most consistent quantitatively with UrQMD. While the hydrodynamic models can match momentum space observables (p_T spectra, v_2) well, they do less well at predicting the HBT results. At the same time, while the UrQMD model does better at predicting the HBT results, like the freeze-out shape, it does less well at predicting the momentum space observables. The

freeze-out eccentricity excitation function provides new, additional information that will help to constrain future model investigations.

Appendix A: Selected studies

A.1 Azimuthal Mixing Bin Width

In the azimuthally differential analysis mixed events are formed using events with similar z vertex, multiplicity, and reaction plane angle. The number of reaction plane mixing bins varies somewhat compared to earlier studies. The earlier STAR analysis used 9 bins (20° wide), the CERES analysis used 12 bins (15° wide), and the current analysis used 8 bins (22.5° wide). To check that this does not affect the results, the analysis was redone with 9 and 12 bins using 200 GeV data taken in 2010.

Figure A.1 shows the effect of varying the number of mixing bins on the normalizations for each angular bin. With wider mixing bins the normalizations show a larger variation. This is related to the fact that more particles and therefore pairs point in the reaction plane direction (around 0°) than point out of the reaction plane (around 90°). With narrower bins the event planes are more aligned so there are more mixed pairs that would enter the denominator of the correlation function constructed around 0° and fewer would enter the denominator for the 90° case. Consider also the limit of one 180° wide mixing bin. All numerators would be divided by the same denominator and a variation in the normalizations must appear. In this case, since the numerator at 0° has more entries than the numerator at 90° the ratio will be smaller

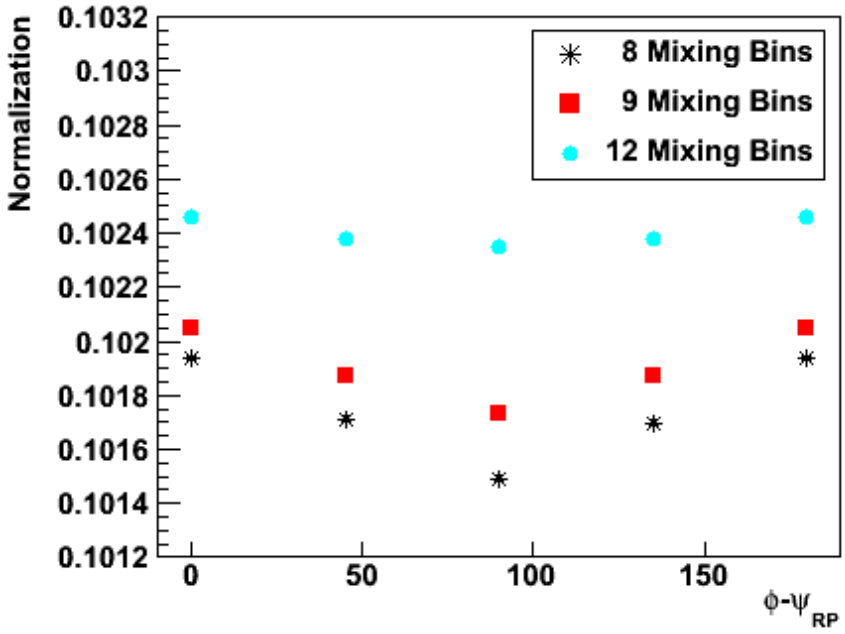

Figure A.1: Variation of the normalization with azimuthal angular bin for Au+Au collisions at mid-rapidity ($-0.5 < y < 0.5$) for Au+Au collisions at $\sqrt{s_{NN}} = 200$ GeV.

for 90°. To normalize the correlation function around 90° must require dividing by a smaller value. Therefore, the normalization in Figure A.1 exhibits a minimum at 90° that is deeper as the width of the mixing bins increases.

In Figure A.2 the Fourier coefficients are compared for various numbers of mixing bins. There appears to be no effect on the Fourier coefficients. This verifies that differences in the number of mixing bins cannot account for the difference between STAR results at 19.6 GeV and the CERES results at 17.3 GeV.

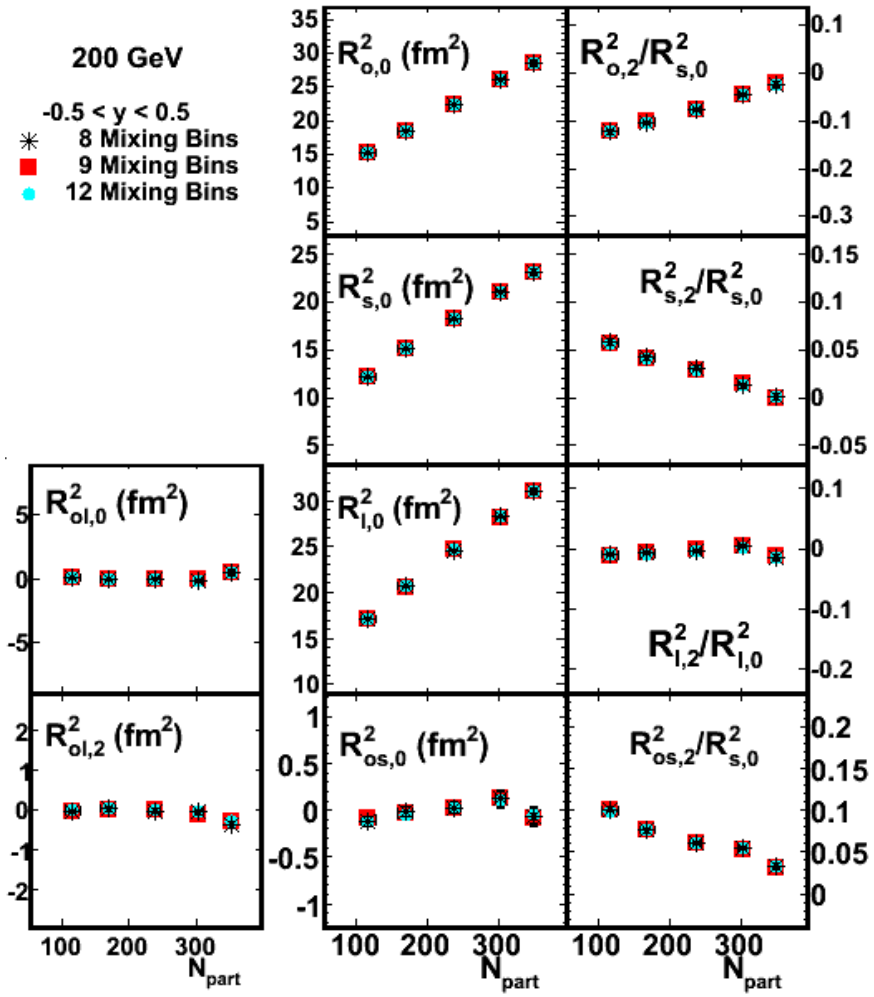

Figure A.2: Centrality dependence of the Fourier coefficients with 8, 9, and 12 mixing bins corresponding to 22.5°, 20°, and 15° widths, respectively. These results are for Au+Au collisions at mid-rapidity ($-0.5 < y > 0.5$) at $\sqrt{s_{NN}} = 200$ GeV taken in 2010.

A.2 Track splitting

In earlier analyses track splitting was found to influence the results and appropriate cuts were identified that removed such effects. Track splitting results in false pairs at low relative momentum that enter the low $|\vec{q}|$ bins in the correlation function. A splitting level (SL), outlined in [66, 67, 86], is used to identify track pairs that are likely split tracks and these are removed from the analysis. In both [66] and [67] the requirement that $-0.5 < SL < 0.6$ was determined to remove track splitting effects. The same cut has been used in various STAR analyses [17, 86, 95, 96, 124].

Similar studies were performed with more recent data sets. A preliminary study using 11.5 GeV data showed the same behavior as in the earlier analyses, although the effect of split tracks appeared to be slightly smaller. The shape of the correlation function was similar to Figure A.3 (which is from 200 GeV data) except a peak developed at low $Q_{\rm inv}$ as the splitting level was increased near $SL < 1$. The same cut $-0.5 < SL < 0.6$ still effectively removed splitting effects although the amount of track splitting may have been slightly smaller than the earlier studies. In that preliminary study tracks were required to have fewer hits, $N_{\rm hits} < 10$, than in the final analysis, $N_{\rm hits} > 15$. However, in that study there was a problem with the particle identification that allowed some contamination. Therefore, the results are not shown here even though it is interesting to mention to contrast with a more recent study.

The same study was repeated later using 200 GeV data taken in 2010 but requiring $N_{\rm hits} > 15$. As can be seen in Figure A.3 there is no significant effect from removing the splitting level cut. This is likely related to the change in $N_{\rm hits}$. Split tracks tend to have rather low $N_{\rm hits}$ and the $N_{\rm hits}$ distribution reaches a minimum around $N_{\rm hits} \approx 15$.

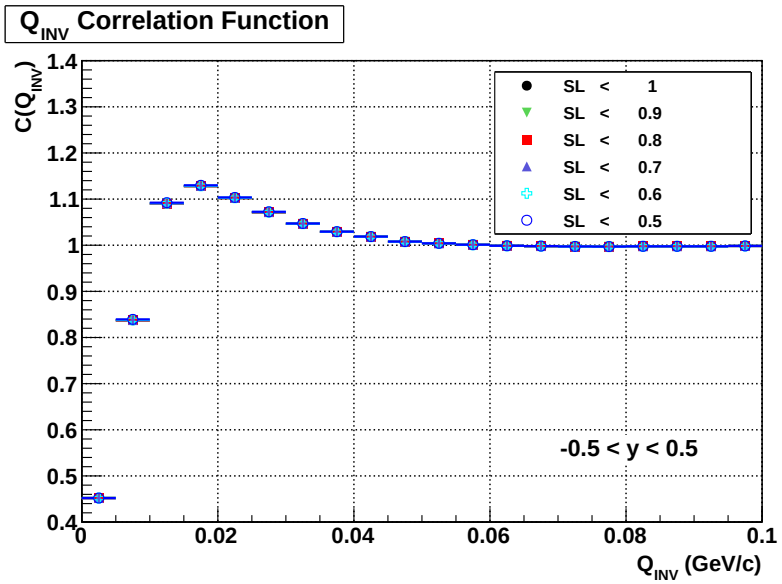

Figure A.3: The effect of varying the splitting level is very small in this example from 200 GeV data taken in 2010. The fraction of merged hits requirement was $FMH < 0.1$ and the number of hits requirement for tracks was $N_{\text{hits}} > 15$. With $FMH < 0.01$ and $FMH < 1$, there is also negligible variation with splitting level.

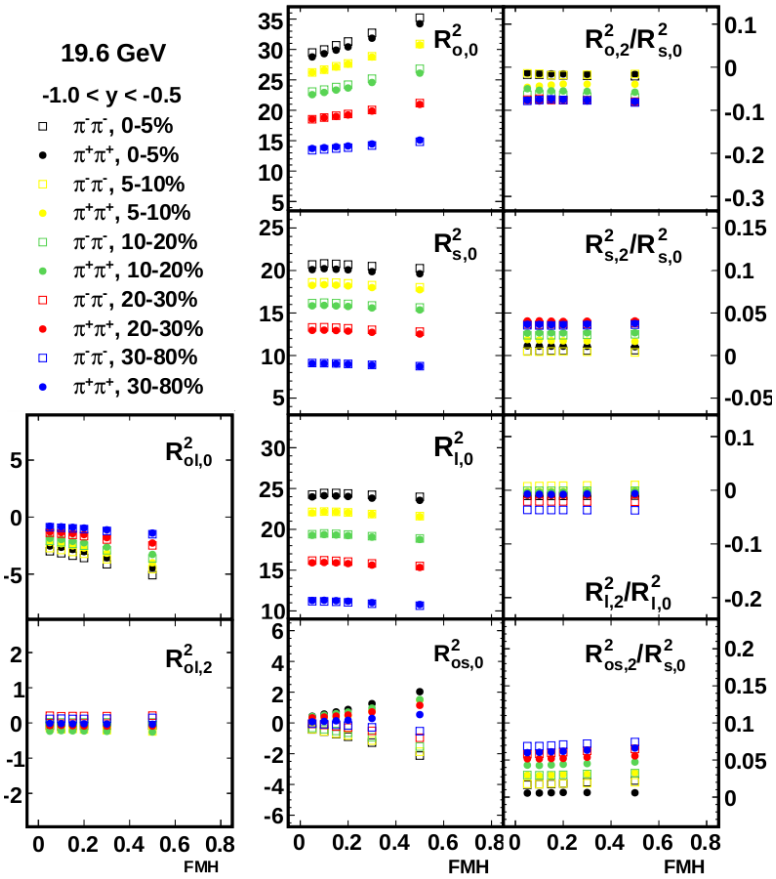

Figure A.4: Dependence of the Fourier coefficients on the fraction of merged hits (FMH) requirement. These results are for Au+Au collisions at $\sqrt{s_{NN}}$=19.6 GeV at backward rapidity ($-1.0 < y < -0.5$). The correction for finite bin width and reaction plane resolution have not been applied in this figure. These particular results are for a wide $0.15 < k_T < 0.6$ range.

It appears that requiring $N_{\text{hits}} > 15$ may already remove split tracks. Even if it had no effect, to be the safe, the same requirement on splitting level, $-0.5 < SL < 0.6$, was still applied in all the results in this thesis.

A.3 Fraction of merged hits

The effects of track merging tend to reduce the correlation function for small values of $\vec{q}$ because merged tracks must have similar trajectories, and therefore low relative momenta. The pairs that these merged tracks would form with each other and with other particles are missed in the numerator. The consequence is a change in the observed radii. Studies presented in [66, 86] and in preparation for the paper [17] found the HBT radii varied as a function of the fraction of merged hits (FMH). Similar studies were performed in more recent data sets. An example of the results is shown in Figure A.4. Similar deviation of the R_{os}^2 term in all the more recent studies compared to the earlier study suggest that track merging is independent of the energy and year that the data was taken. Similar values of the corresponding uncertainties in the radii are obtained consistent with the earlier study as listed in Table 7.2. As in other recent STAR analyses [17, 86, 95, 96] the same requirement, $FMH < 0.1$, was applied. As noted in [17], R_{out} is most affected by track merging which is clear from the middle column of Figure A.4.

Appendix B: Non-Gaussian effects on azimuthal HBT analyses

The discussion in this appendix is the same the appendix in Reference [85], the paper corresponding to this thesis.

In azimuthally integrated HBT analyses, the crossterms (R_{os}, R_{ol}, R_{sl}) vanish at mid-rapidity. In this case, the sign of the components of the relative momentum vector, $\vec{q}$, are arbitrary. The three dimensional $\vec{q}$-space may be folded, so that $q_{\rm long}$ and $q_{\rm side}$ are always positive, for instance, to increase statistics in each ($q_{\rm out}$,$q_{\rm side}$,$q_{\rm long}$) bin. In azimuthally differential analyses, however, the relative signs of components are important in order to extract non-zero crossterms [67, 86]. At mid-rapidity, the relative sign of $q_{\rm out}$ and $q_{\rm side}$ must be maintained to extract values of R^2_{os}. Away from mid-rapidity, the R^2_{ol} crossterm is also non-zero and $q_{\rm long}$ must be allowed to have both positive or negative values. This way the relative sign of $q_{\rm out}$ and $q_{\rm long}$ is maintained and the corresponding crossterm can be extracted.

If the "q-folding" procedure is performed and the crossterms are included as fit parameters, the fit parameters become strongly correlated and the values of the extracted radii change. The size of this effect varies randomly from one azimuthal bin to the next, causing large variations in the extracted oscillations of the radii. This behavior is related to the non-Gaussianess of the correlation function. Due to the

necessity of using finite bins in k_T and centrality, which are described by a range of radii, the radii extracted from these correlation functions are some average value. If too much q-folding is performed, the covariance of fit parameters that appears allows deviations from the average values and the results become unreliable.

This is an important consideration for any HBT analysis performed away from mid-rapidity, or relative to the first order reaction plane, where measurement of crossterms is important. In this analysis, no folding of $\vec{q}$-space is performed and so any possible effects of this phenomena are eliminated.

Bibliography

[1] N. Cabibbo and G. Parisi, Phys. Lett. B **59**, 67 (1975).

[2] E. Shuryak, Phys. Lett. B **78**, 150 (1975).

[3] J. Adams et al. (STAR), Nucl. Phys. A **757**, 102 (2005).

[4] K. Adcox et al. (PHENIX), Nucl. Phys. A **757**, 184 (2005).

[5] B. B. Back et al. (PHOBOS), Nucl. Phys. A **757**, 28 (2005).

[6] I. Arsene et al. (BRAHMS), Nucl. Phys. A **757**, 1 (2005).

[7] M. M. Agarwal et al. (STAR) (2010), `arXiv:1007.2613`.

[8] M. A. Lisa, E. Frodermann, G. Graef, M. Mitrovski, E. Mount, H. Petersen, and M. Bleicher, New J. Phys. **13** (2011).

[9] File: Standard_Model_of_Elementary_Particles.png, 2013. Used under the Creative Commons Attribution 3.0 Unported license. http://creativecommons.org/licenses/by/3.0/.

[10] A. Enokizomo, Ph.D. thesis, Hiroshima University (2004).

[11] A. M. Poskanzer and S. A. Voloshin, Phys. Rev. C **58**, 1671 (1998).

[12] B. Alver and G. Roland, Phys. Rev. C **81**, 054905 (2010).

[13] S. Shi (STAR Collaboration), *Event anisotropy v_2 in Au+Au collisions at $\sqrt{s_{NN}}$=7.7-62.4 GeV with STAR* (2012), presentation at Quark Matter 2012.

[14] P. F. Kolb and U. W. Heinz (2003), `arXiv:nucl-th/0305084`.

[15] M. A. Lisa et al. (E895), Phys. Lett. B **496**, 1 (2000).

[16] D. Adamova et al. (CERES), Phys. Rev. C **78**, 064901 (2008).

[17] J. Adams et al. (STAR Collaboration), Phys. Rev. Lett. **93**, 012301 (2004).

[18] R. Vogt, *Ultrarelativistic Heavy-Ion Collisions* (Elsevier, 2007).

[19] B. Back, M. Baker, D. Barton, R. Betts, M. Ballintijn, et al., Phys. Rev. Lett. **91**, 052303 (2003).

[20] M. G. Alford, A. Schmitt, K. Rajagopal, and T. Schafer, Rev. Mod. Phys. **80**, 1455 (2008).

[21] J. C. Collins and M. J. Perry, Phys. Rev. Lett. **34**, 1353 (1975).

[22] P. B. Demorest et al., Nature **467**, 1081 (2010).

[23] F. R. Brown, F. P. Butler, H. Chen, N. H. Christ, Z. Dong, W. Schaffer, L. I. Unger, and A. Vaccarino, Phys. Rev. Lett. **65**, 2491 (1990).

[24] Y. Aoki, G. Endrodi, Z. Fodor, S. Katz, and K. Szabo, Nature **443**, 675 (2006).

[25] S. Borsanyi et al. (Wuppertal-Budapest Collaboration), JHEP **1009**, 073 (2010).

[26] M. Cheng (HotQCD Collaboration), PoS **LAT2009**, 175 (2009).

[27] A. Masayuki and Y. Koichi, Nucl. Phys. A **504**, 668 (1989).

[28] A. Barducci, R. Casalbuoni, S. De Curtis, R. Gatto, and G. Pettini, Phys. Rev. D **41**, 1610 (1990).

[29] A. Barducci, R. Casalbuoni, S. D. Curtis, R. Gatto, and G. Pettini, Phys. Lett. B **231**, 463 (1989).

[30] A. Barducci, R. Casalbuoni, G. Pettini, and R. Gatto, Phys. Rev. D **49**, 426 (1994).

[31] J. Berges and K. Rajagopal, Nucl. Phys. B **538**, 215 (1999).

[32] M. A. Halasz, A. D. Jackson, R. E. Shrock, M. A. Stephanov, and J. J. M. Verbaarschot, Phys. Rev. D **58**, 096007 (1998).

[33] O. Scavenius, A. Mócsy, I. N. Mishustin, and D. H. Rischke, Phys. Rev. C **64**, 045202 (2001).

[34] N. G. Antoniou and A. S. Kapoyannis, Phys. Lett. B **563**, 165 (2003).

[35] Y. Hatta and T. Ikeda, Phys. Rev. D **67**, 014028 (2003).

[36] M. Stephanov, Prog. Theor. Phys. Suppl. **153**, 139 (2004).

[37] F. Karsch, C. R. Allton, S. Ejiri, S. J. Hands, O. Kaczmarek, E. Laermann, and C. Schmidt, Nucl. Phys. B - Proc. Suppl. **129-130**, 614 (2004).

[38] Z. Fodor and S. D. Katz, JHEP **0404**, 050 (2004).

[39] R. V. Gavai and S. Gupta, Phys. Rev. D **71**, 114014 (2005).

[40] A. Li, A. Alexandru, and K.-F. Liu, Phys. Rev. D **84**, 071503 (2011).

[41] S. Datta, R. V. Gavai, and S. Gupta, Nucl. Phys. A **904-905**, 883c (2013).

[42] M. Cheng, P. Hendge, C. Jung, F. Karsch, O. Kaczmarek, et al., Phys. Rev. D **79**, 074505 (2009).

[43] V. Koch, A. Majumder, and J. Randrup, Phys. Rev. Lett. **95**, 182301 (2005).

[44] M. A. Stephanov, K. Rajagopal, and E. V. Shuryak, Phys. Rev. D **60**, 114028 (1999).

[45] S. V. Afanasiev et al. (NA49 Collaboration), Phys. Rev. Lett. **86**, 1965 (2001).

[46] T. J. Tarnowsky (STAR Collaboration), Acta Phys.Polon.Supp. **5**, 515 (2012).

[47] T. Anticic et al. (NA49 collaboration), Phys. Rev. C **83**, 061902 (2011).

[48] A. Rustamov (NA49/SHINE Collaboration), Nucl. Phys. A **904-905**, 915c (2013).

[49] M. A. C. Lamont (STAR), J. Phys. G **32**, S105 (2006).

[50] L. Adamczyk et al. (STAR Collaboration), Phys. Rev. Lett. **110**, 142301 (2013).

[51] M. Sumbera (STAR Collaboration), Acta Phys. Polon. Supp. **6**, 429 (2013).

[52] P. Seyboth, Acta Phys. Polon. Supp. **6**, 409 (2013).

[53] C. Alt et al. (NA49 Collaboration), Phys. Rev. C **77**, 024903 (2008).

[54] P. Braun-Munzinger, J. Cleymans, H. Oeschler, and K. Redlich, Nucl. Phys. A **697**, 902 (2002).

[55] H. Petersen and M. Bleicher, PoS **CPOD2006**, 025 (2006).

[56] S. S. Adler et al. (PHENIX Collaboration), Phys. Rev. Lett. **94**, 232302 (2005).

[57] L. P. Csernai and D. Röhrich, Phys. Lett. B **458**, 454 (1999).

[58] H. Stöcker, Nucl. Phys. A **750**, 121 (2005).

[59] J. Brachmann, S. Soff, A. Dumitru, H. Stöcker, J. A. Maruhn, W. Greiner, L. V. Bravina, and D. H. Rischke, Phys. Rev. C **61**, 024909 (2000).

[60] R. J. M. Snellings, H. Sorge, S. A. Voloshin, F. Q. Wang, and N. Xu, Phys. Rev. Lett. **84**, 2803 (2000).

[61] M. Bleicher and H. Stöcker, Phys. Lett. B **526**, 309 (2002).

[62] Y. Pandit, Nucl. Phys. A **904-905**, 357c (2013).

[63] K. H. Ackermann et al., Nucl. Instr. Meth. A **499**, 624 (2003).

[64] M. Anderson et al. (STAR collaboration), Nucl. Instr. Meth. A **499**, 659 (2003).

[65] M. Anderson et al. (STAR collaboration), Nucl. Instr. Meth. A **499**, 679 (2003).

[66] M. Lopez-Noriega, Ph.D. thesis, The Ohio State University (2004).

[67] R. Wells, Ph.D. thesis, The Ohio State University (2002).

[68] R. H. Brown and R. Q. Twiss, Nature **178**, 1046 (1956).

[69] G. Goldhaber, S. Goldhaber, W. Lee, and A. Pais, Phys. Rev. **120**, 300 (1960).

[70] M. A. Lisa, S. Pratt, R. Soltz, and U. Wiedemann, Ann. Rev. Nucl. Part. Sci. **55**, 357 (2005).

[71] S. Pratt, T. Csörgő, and J. Zimányi, Phys. Rev. C **42**, 2646 (1990).

[72] S. E. Koonin, Phys. Lett. B **70**, 43 (1977).

[73] U. A. Wiedemann and U. Heinz, Phys. Rep. **319**, 145 (1999).

[74] S. Pratt, Phys. Rev. Lett. **53**, 1219 (1984).

[75] M. G. Bowler, Z. Phys. C **39** (1988).

[76] W. A. Zajc et al., Phys. Rev. C **29**, 2173 (1984).

[77] H. W. Barz, Phys. Rev. C **59**, 2214 (1999).

[78] M. Bowler, Phys. Lett. B **270**, 69 (1991).

[79] G. Baym and P. Braun-Munzinger, Nucl. Phys. A **610**, 286C (1996).

[80] E. Mount, G. Graef, M. Mitrovski, M. Bleicher, and M. A. Lisa, Phys. Rev. C **84**, 014908 (2011).

[81] S. Pratt, Phys. Rev. D **33**, 1314 (1986).

[82] G. Bertsch, M. Gong, and M. Tohyama, Phys. Rev. C **37**, 1896 (1988).

[83] S. Chapman, P. Scotto, and U. Heinz, Phys. Rev. Lett. **74**, 4400 (1995).

[84] S. Chapman, J. R. Nix, and U. Heinz, Phys. Rev. C **52**, 2694 (1995).

[85] L. Adamczyk et al. (STAR Collaboration), Phys. Rev. C (unpublished).

[86] J. Adams et al. (STAR Collaboration), Phys. Rev. C **71**, 044906 (2005).

[87] F. Retière and M. A. Lisa, Phys. Rev. C **70**, 044907 (2004).

[88] U. Heinz, A. Hummel, M. A. Lisa, and U. A. Wiedemann, Phys. Rev. C **66**, 044903 (2002).

[89] M. G. Bowler, Phys. Lett. B **270**, 69 (1991).

[90] Y. M. Sinyukov, R. Lednicky, S. Akkelin, J. Pluta, and B. Erazmus, Phys. Lett. B **432**, 248 (1998).

[91] J. Barrette et al. (E877 Collaboration), Phys. Rev. C **55**, 1420 (1997).

[92] H. Appelshäuser et al. (NA49 Collaboration), Phys. Rev. Lett. **80**, 4136 (1998).

[93] P. Danielewicz et al., Phys. Rev. C **38**, 120 (1988).

[94] J. Barrette et al., Phys. Rev. C **56**, 3254 (1997).

[95] B. I. Abelev et al. (STAR Collaboration), Phys. Rev. C **80**, 024905 (2009).

[96] M. M. Aggarwal et al. (STAR Collaboration), Phys. Rev. C **83**, 064905 (2011).

[97] D. Adamova et al., Nucl. Phys. A **714**, 124 (2003).

[98] M. A. Lisa et al. (E895 Collaboration), Phys. Rev. Lett. **84**, 2798 (2000).

[99] I. G. Bearden et al. (NA44 Collaboration), Phys. Rev. C **58**, 1656 (1998).

[100] C. Alt et al., Phys. Rev. C **77**, 064908 (2008).

[101] R. A. Soltz, M. Baker, and J. H. Lee, Nucl. Phys. A **661**, 439 (1999).

[102] M. M. Aggarwal et al. (WA98 Collaboration), Phys. Rev. C **67**, 014906 (2003).

[103] K. Aamodt et al. (ALICE Collaboration), Phys. Lett. B **696**, 328 (2011).

[104] D. H. Rischke and M. Gyulassy, Nucl. Phys. A **608**, 479 (1996).

[105] U. W. Heinz and P. F. Kolb (2002), arXiv:hep-ph/0204061.

[106] M. Herrmann and G. Bertsch, Phys. Rev. C **51**, 328 (1995).

[107] U. A. Wiedemann, P. Scotto, and U. Heinz, Phys. Rev. C **53**, 918 (1996).

[108] A. N. Makhlin and Y. M. Sinyukov, Z. Phys. C **39**, 69 (1988).

[109] A. Kisiel (ALICE Collaboration), J. Phys. G **38**, 124008 (2011).

[110] J. L. Gramling (ALICE Collaboration), AIP Conf. Proc. **1422**, 68 (2012).

[111] L. Ahle et al. (E-802 Collaboration), Phys. Rev. C **66**, 054906 (2002).

[112] B. B. Back et al. (PHOBOS Collaboration), Phys. Rev. C **73**, 031901 (2006).

[113] D. Adamova et al. (CERES Collaboration), Phys. Rev. Lett. **90**, 022301 (2003).

[114] C. Alt et al. (NA49 Collaboration), Phys. Rev. C **77**, 024903 (2008).

[115] Q. Li, C. Shen, and M. Bleicher (2010), arXiv:1009.3334.

[116] Q. Li, M. Bleicher, and H. Stocker, Phys. Lett. B **659**, 525 (2008).

[117] L. Adamczyk et al. (STAR collaboration), Phys. Rev. C **86**, 054908 (2012).

[118] C. Shen and U. Heinz, Phys. Rev. C **85**, 054902 (2012).

[119] C. Shen, U. Heinz, P. Huovinen, and H. Song, Phys. Rev. C **82**, 054904 (2010).

[120] P. Huovinen and P. Petreczky, Nucl. Phys. A **837**, 26 (2010).

[121] H. Petersen, M. Bleicher, S. A. Bass, and H. Stocker (2008), arXiv:0805.0567.

[122] Q. Li, M. Bleicher, and H. Stoecker, Phys. Rev. C **73**, 064908 (2006).

[123] Q. Li, M. Bleicher, X. Zhu, and H. Stocker, J. Phys. G **34**, 537 (2007).

[124] C. Adler et al. (STAR), Phys. Rev. Lett. **87**, 082301 (2001).